EPFL

Investigation of femtosecond laser-tuned thermomechanical properties of fused silica

Présentée le 28 octobre 2020

à la Faculté des sciences et techniques de l'ingénieur
Laboratoire Galatea
Programme doctoral en manufacturing

pour l'obtention du grade de Docteur ès Sciences

par

Pieter VLUGTER

Acceptée sur proposition du jury

Prof. J. Brugger, président du jury
Prof. Y. Bellouard, directeur de thèse
Prof. M. Lancry, rapporteur
Prof. S. Juodkazis, rapporteur
Prof. G. Villanueva, rapporteur

École
polytechnique
fédérale
de Lausanne

2020

Acknowledgements

Abstract

The thermomechanical properties of materials are among the most important properties for designing precision instruments, in particular for devices seeking high-dimensional stability, invariant temperature-elastic properties or low thermoelastic losses. Dedicated materials have been created for these purposes, such as Zerodur® and Silinvar®.

In this thesis work, we propose a method for selectively tuning the thermomechanical behavior of transparent materials using ultrafast lasers. Specifically, we investigate laser-exposed fused silica's thermal expansion coefficient and thermoelastic properties. Fused silica's already outstanding physical properties, such as low-thermal expansion coefficient and low thermoelastic losses, offer a promising starting point for exploring its limits as a high performance thermomechanical material.

This study unraveled the preponderance of certain laser induced modifications in this process. The results are obtained using micro-mechanical devices specifically designed for this purpose. A bimorph structure is used to characterize the thermal expansion, while a resonant cantilever is implemented for investigating thermoelastic properties. Using these micro-instruments, we show that: 1) These laser-induced modifications can be used to tune silica's thermal expansion coefficient permanently. In particular, we demonstrate that a given exposure regime leads to a lower thermal expansion than the pristine material, while other exposure conditions yield the opposite result. 2) The positive temperature-elastic coefficient of silica is reduced by nearly 50% after laser exposure. Such performance turns fused silica into a good candidate for temperature-stable resonators. 3) The Young's modulus at room temperature can display laser-induced elastic anisotropy controlled by the laser polarization. 4) The thermomechanical properties can be fine-tuned with an extra thermal annealing step.

This thesis is a first step towards designing materials with arbitrary thermomechanical behavior, starting from a given transparent material. This approach stands out from other methods from the fact that material properties can selectively be transformed at the microscale level with unique and tailored thermomechanical properties, and this, in arbitrary substrate shapes. It enables the fabrication of metamaterials with engineered thermomechanical response. From a device point-of-view, this research further expands the capability of femtosecond laser to tune refractive index and etching selectivity towards thermomechanical properties, forming a larger palette of possible ultrafast laser-induced functionalities. This addition further enlarges the potential of femtosecond laser for making highly integrated multifunctional devices. This is in particular interesting for precision instruments, temperature-responsive transducers, as well as temperature-stable optomechanical devices.

Résumé

Les propriétés thermodynamiques des matériaux sont parmi les plus critiques pour la conception d'instruments de précision, en particulier pour des dispositifs visant une haute stabilité dimensionnelle, une invariance des propriétés thermoélastiques ou de faibles pertes thermoélastiques. Des matériaux visant à maximiser ces critères ont été spécialement conçus, comme le Zerodur® et le Silinvar®.

Dans ce travail de thèse, nous proposons une méthode d'ajustement du comportement thermomécanique de matériaux transparents à l'aide de lasers à impulsions ultra-courtes. Nous étudions en particulier les modifications du coefficient de dilatation thermique et des propriétés thermoélastiques du verre de silice après exposition. Les exceptionnelles propriétés thermoélastiques du verre de silice, son faible coefficient de dilatation thermique et ses faibles pertes thermomécaniques font de ce verre un point de départ prometteur pour étudier les limites des matériaux à haute performance thermomécanique.

Cette étude a démontré l'importance qu'ont les modifications induites par l'exposition au laser à impulsions ultra-courtes sur les propriétés thermomécaniques du verre de silice. Les résultats principaux sont obtenus à l'aide de dispositifs micromécaniques. Une structure bimorphe est utilisée pour caractériser l'expansion thermique, tandis qu'un cantilever résonant est implémenté pour étudier les propriétés thermoélastiques. À l'aide de ces micro-instruments, nous démontrons quatre points : 1) ces modifications induites par l'exposition au laser peuvent être utilisées pour ajuster de manière permanente la dilatation thermique du verre de silice. Nous montrons notamment qu'un régime d'exposition donné conduit à une diminution de la dilatation thermique, tandis qu'un autre induit le résultat opposé. 2) Le coefficient thermoélastique du verre de silice est réduit d'environ de moitié après l'exposition. Un tel résultat fait du verre de silice un excellent matériau pour la fabrication de résonateurs thermostables. 3) La mesure du module de Young à température ambiante montre l'anisotropicité élastique causée par l'exposition, dont la direction est contrôlable par la polarisation du rayonnement. 4) Les propriétés thermomécaniques peuvent être affinées avec un recuit supplémentaire.

Ce travail de thèse est une première étape vers le développement de composants avec des comportements thermomécaniques arbitraires. Cette approche se démarque par le fait que les modifications du matériau se font localement à l'échelle microscopique, permettant d'atteindre des propriétés thermoélastiques uniques, pouvant être spécialement adaptées à une application donnée, et ce pour des formes de substrats arbitraires. Elle permet la fabrication de métamatériaux aux propriétés thermomécaniques personnalisées. Ce travail étend également la gamme d'applications des lasers à impulsions ultra-courtes, de la modification de l'indice

Résumé

de réfraction et du taux de gravure chimique, vers l'ajustement des propriétés thermomécaniques, formant une gamme étendue de fonctionnalités permises par ces sources. Une telle technologie pourrait en particulier améliorer la fabrication d'instruments de précision, de capteurs thermosensibles, d'actuateurs, et des composants optomécaniques thermostables.

Nomenclature

Symbol	Description	Unit
A	Area	[m^2]
A_s, A_l	Substrate area, laser modified area	[m^2]
c	Constant strain	[-]
C_1, C_2, C_3	Geometrical constants	[m^3]
E	Young's modulus	[Pa]
E_s, E_l	Substrate's Young's modulus, laser affected volume's Young's modulus	[Pa]
$\hat{E}_l$	Average Young's modulus, a composition of E_s and E_l	[Pa]
E_{np}, E_{pp}	Non-porous layer Young's modulus, porous layer Young's modulus	[Pa]
$E_{l,11}$, $E_{l,22}$	Laser affected volume's Young's modulus along the axis 1, laser affected volume's Young's modulus along the axis 2	[Pa]
$\vec{E}_{el}$	Electric field vector	[V/m]
f	Resonance frequency of the resonator	[Hz]
$\vec{g}$	Gravitational acceleration vector	[m/s^2]
G	Shear modulus	[Pa]
$G_{l,12}$	Laser affected shear modulus in the local coordinate frame 1-2	[Pa]
G_{np}, G_{pp}	Non-porous layer's shear modulus, porous layer's shear modulus	[Pa]
I	Second monument of area	[m^4]
I_s, I_l	Substrate's second monument of area, laser affected volume's second monument of area	[m^4]
k	Stiffness	[N/m]
$\vec{k}$	Laser beam propagation vector	[-]
l	length	[m]
l_s	line spacing	[m]
L	Length	[m]
L_c, L_l	Length of the cantilever, length of the laser affected volume	[m]
m	Mass	[kg]
M	Moment of force	[Nm]
$\underline{Q}_l$	Stiffness matrix of the laser affected volume	[-]
r	Radius	[m]
r_{meas}, r_0, r_T, r_α, r_β	Measured radius, radius at room temperature, temperature-dependent radius, radius due to CTE difference, radius due to temperature dependent Young's modulus	[m]

Symbol	Description	Unit
R	Universal gas constant	$[\text{J} \cdot \text{K}^{-1} \cdot \text{mol}^{-1}]$
$\underline{R}$	Rotation matrix	[-]
t	Thickness	[m]
t_s, t_l, t_{st}	Substrate thickness, laser affected volume thickness, top substrate thickness	[m]
t_b	Distance between the bending axis and the bottom surface	[m]
T, ΔT, T_{ann}, T_s	Temperature, temperature difference with respect to room temperature, annealing temperature, softening temperature	[°C]
$\vec{v}$	Laser beam scanning direction vector	[-]
V	Volume	$[\text{m}^3]$
V_s	Volume fraction of the unexposed material between the exposed zones	[-]
V_l	Volume fraction of the laser exposed material	[-]
w	Width	[m]
(x, y, z)	Cartesian coordinate system	[m]
(1, 2)	In-plane local coordinate frame, aligned with respect to the nanograting orientation	[m]
α	Coefficient of thermal expansion (CTE)	[-/°C]
α_s, α_l	CTE of the substrate, laser affected volume	[-/°C]
$\hat{\alpha}_l$	Average CTE, a composition of α_s and α_l	[-/°C]
β	Non-dimensional temperature-Young's modulus coefficient	[-/°C]
β_s, β_l	Non-dimensional temperature-Young's modulus coefficient of the substrate, laser affected volume	[-/°C]
$\hat{\beta}_l$	Average non-dimensional temperature-Young's modulus coefficient, a composition of β_s and β_l	[-/°C]
δ	Vertical tip-displacement of the bimorph structure	[m]
δ_{meas}, δ_α	Measured tip displacement, tip displacement due CTE difference	[m]
ϵ	Strain	[-]
ϵ_s, ϵ_l, ϵ_{st}	Strain in substrate, strain in laser affected volume, strain in top layer substrate	[-]
θ	Angle between the axis aligned along the nanograting	[°]
$\theta_{Si-O-Si}$	Bridging oxygen bond angle	[°]
λ	Wavenumber, corresponding to the resonance mode	[-]
ν	Poisson's ratio	[-]
ν_l	Laser affected volume's Poisson's ratio	[-]
$\nu_{l,21}$, $\nu_{l,12}$	Poisson's ratios of an orthotropic material, in a local coordinate frame 1-2	[-]
ν_{np}, ν_{pp}	Non-porous layer's Poisson's ratio, porous layer's Poisson's ratio	[-]
ρ	Mass density	[-]

Nomenclature

Symbol	Description	Unit
$\sigma_s, \sigma_l, \sigma_{st}$	Stress in substrate, stress in laser affected zone, stress in top layer substrate	[Pa]
τ_{12}	Shear stress in local coordinate frame 1-2	[Pa]
τ_{xy}	Shear stress in global coordinate frame x-y	[Pa]

Subscripts	Description
ann	Annealing
l	Laser affected volume
s	Substrate
s-t	Top layer substrate
,T	As function of temperature
xx, yy	x- and y-direction in global coordinate frame x-y
xy, yx	Rotation from x to y and from y to x in global coordinate frame x-y
,0	At room temperature
11, 22	1- and 2-direction in local coordinate frame 1-2
12, 21	Rotation from 1 to 2 and from 2 to 1 in local coordinate frame 1-2

Superscripts	Description
$\perp$	Perpendicular to $\vec{v}_s$
$/\!/$	Parallel to $\vec{v}_s$

Abbreviation	Description
CTE	Coefficient of thermal expansion
DHM	Digital holographic microscope
L	Lock-in amplifier
LAZ	Laser affected volume
PI	Proportional integrating controller
PID	Proportional integrating differentiating controller
S	Signal generator
TCF	Temperature coefficient of frequency

Contents

Contents

1 Introduction

Dimensional and elastic properties changes of solids due to temperature variations pose numerous constraints in engineering constructions, instruments or devices. A first issue is the thermal expansion mismatch between materials. A difference in so-called "coefficient of thermal expansion" or "CTE" leads to stress in and at the boundaries of the materials. As an example, railways tend to buckle in summertime if no mechanism is applied to compensate for the temperature-induced dilation. In electronic devices and/or metal-glass assemblies, solder joints are subject to thermal stresses due to CTE mismatch among the different components, leading to failure [1]. Careful material selection and specific design principles are also key for maximizing the performance of MEMS devices [2, 3]. In these devices, movable structures are used for sensing e.g. pressure [4], angular velocity [5] or acceleration [6]. Thermal induced deformations or stresses in these mechanical structures interfere with the measurement, leading to inferior performance [7].

A vast majority of optical systems, like telescopes, interferometers [8, 9] and gravitational detectors (LIGO and VIRGO) [10], require a high dimensional stability. Here, in particular, the thermal expansion must be minimized or controlled, apart from avoiding parasitic thermal induced stresses and/or deformations.

A last issue, somewhat less known, is related to the stability of frequency references, which play a major role in time keeping devices, and other instruments relying on reference resonators, such as in miniaturized frequency references or RF-filters [11, 12]. The accuracy of these devices, rely not only on the dimensional stability described before, but also on temperature-induced elastic modulus change of the resonator. As an example, an accuracy of a second over a year for a single-beat/second pendulum, would require extraordinary temperature-stable dimensional and elastic material properties, in the order of 10^{-15} [13].

To address these problems, various approaches have been explored. It includes the design of new materials such as Aluminium-Silicon-Carbide (AlSiC), a high thermally conductive material, but low in thermal expansion, is particular useful for electronic packaging. Another example is Kovar, a low thermal expansion nickel-cobalt alloy, invented to join glass-metal assemblies [14]. Furthermore, specialized ceramics, such as Zerodur®, ultra low expansion

glasses (ULE), or Invar®, are used to achieve high dimensional stability. Other methods include the use of special construction principles. Examples of these types of constructions are the gridiron pendulum [13], invented in the early 18th century or recently proposed concepts based on metamaterials [15, 16]. There is a growing interest for metamaterials that have complex thermal expansion behavior by design, thanks to the advances in 3D fabrication technologies such as additive manufacturing.

Here, we investigate how laser-induced localized bulk modifications can be used to engineer the thermomechanical properties of silica. Specifically,

this thesis work c on the characterization of the thermomechanical properties of ultrafast laser exposed fused silica.

Ultrafast laser machining has in the last two decades paved new ways to fabricate three dimensional multi-functional devices at the microscale in transparent materials. With this technology it is possible to modified locally the physical properties of a microscale volume, at an arbitrarily chosen location of a given transparent material. Using this technology, optical networks with waveguiding, polarization and/or reflective capabilities can be inscribed and likewise micro-structures can be fabricated, such as combarrays, positioners, resonators or fluidic networks. Being able to change the thermomechanical properties, in any given location of a device, potentially gives the freedom to design arbitrary thermal expansion compensation schemes, in a system approach, and potentially at the material level, or for the realization of thermal actuators.

Towards this goal, first, progress in the realization of materials and systems with extraordinary thermal expansion properties is reviewed. Second, the state-of-the-art of ultra-fast laser processing of transparent materials is introduced. Third, the envisioned potential of using ultrafast laser exposure for tailoring the thermomechanical properties is explained. Finally, the thesis objectives are detailed, followed with a thesis outline.

1.1   Thermomechanical properties of solids

The thermal expansion of the vast majority of materials can be understood according to the asymmetric shape of their interatomic potential well (approximated by a Lennard-Jones potential, see Figure 1.1a. This potential well describes the potential energy (Φ) between
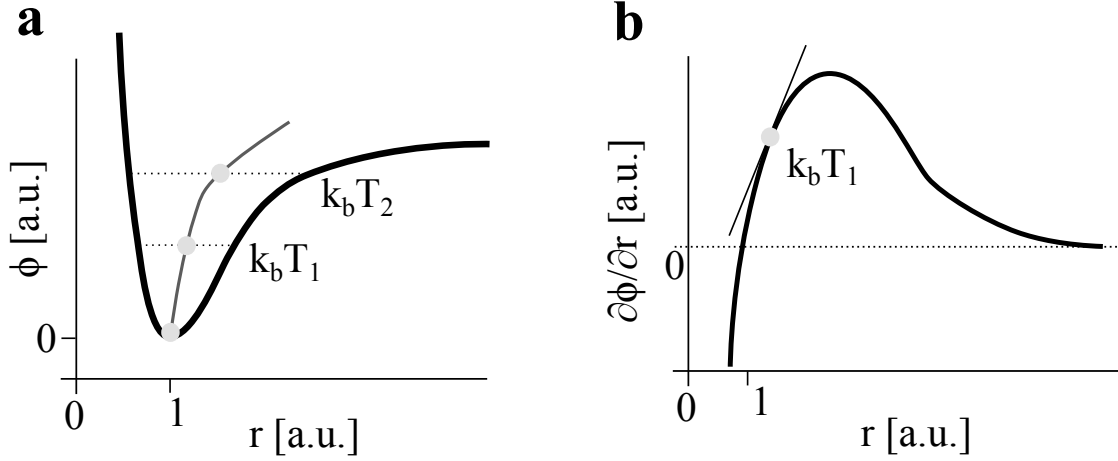
Figure 1.1 – a) The potential energy, Φ, between two atoms as a function of the interatomic distance, r. The mean interatomic distance increases for elevated temperatures, where $T_2 > T_1$. b) The potential energy's derivative, $\partial\Phi/\partial r$, which represents the interatomic force and the slope for a given interatomic distance or temperature is related to the elastic properties.

two atoms as function of their interatomic distances (r). The equilibrium is the balance between repulsive forces (Pauli repulsion) and attractive ones (i.e. van der Waals) [17]. At elevated temperatures, atoms "oscillate" around the mean interatomic distance. The mean interatomic distance increases along with the temperature, because of the potential well asymmetric character, as illustrated in Figure 1.1a, where $T_2 > T_1$. Interestingly, the elastic properties, hence the stiffness of the material, can also be discussed with this model. As the spatial derivative of the potential energy $\partial\Phi/\partial r$ is a force (as depicted in Figure 1.1b as function of r), the spatial change of interatomic force, for small displacements under a linear approximation (i.e. the indicated slope in the figure), defines the "stiffness" between the two atoms. For increasing interatomic distances, and thus for increasing temperatures, the connection becomes less stiff. A temperature decreasing Young's modulus is therefore a common behavior among solids. Together with the density and thermal conductivity, these material properties are usually closely related [18].

This simple two-atom model captures well the thermal expansion behavior of most materials. However, for more complex materials, it is rather incomplete when considering complex molecular arrangements, with several vibrational modes, or when considering, the macroscopic behavior of multiple component materials as well as phase transitions. The negative thermal expansion of water near the solidification point is a classical example of anomalous behavior near a phase transition.
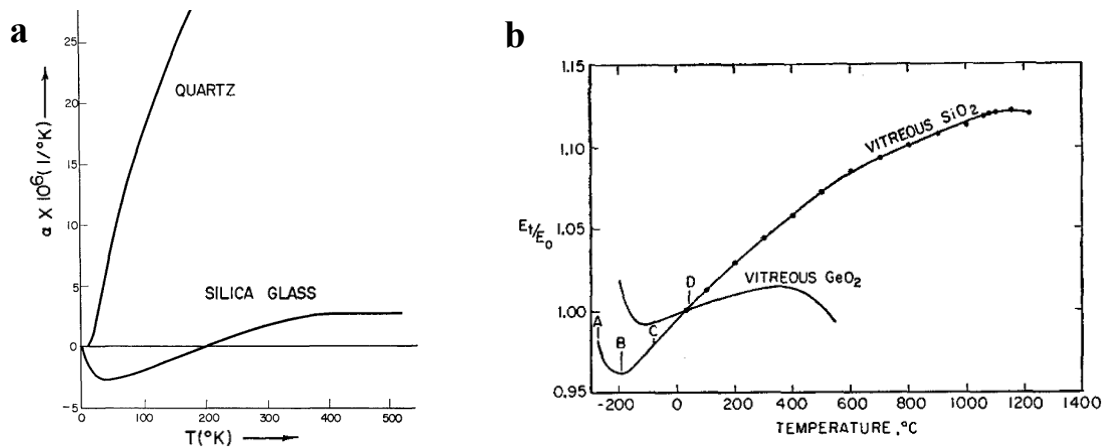
Figure 1.2 – a) *Thermal expansion coefficients for amorphous SiO$_2$ and quartz. Notice, the negative CTE for temperatures below 200K. The figure is adapted from [19].* **b)** *The increasing Young's modulus along with temperature for amorphous SiO$_2$ and GeO$_2$ [20].*

The thermomechanical properties of fused silica display an anomalous behavior. For instance, for temperatures below 200K, the thermal expansion coefficient (CTE) is negative [21], see Figure 1.2a. Above this temperature, at room temperature, the values are abnormally low (~0.6 ppm/K) in contrast with, for instance, its crystalline counterpart, quartz. The other abnormal thermomechanical property is the temperature-dependent Young's modulus, (Figure 1.2b). Where other materials display a decrease, fused silica shows an increasing Young's modulus over temperature. We will elaborate more about the current understanding of these abnormal behaviors in Chapter 6. Nevertheless, notice that both, the CTE and the positive temperature-elastic coefficient, cannot be explained by a Lennard-Jones potential-based model.

Progress in thermomechanical designed materials and systems

Tailoring the thermal expansion of materials to obtain high dimensional stability is a research topic for many years. Starting from the discovery of Invar by Charles-Édouard Guillaume, Nobel Prize in Physics 1920, a great deal of effort has been put into finding materials approaching zero-thermal expansion while having other interesting physical properties, such as optical transparency or low density. This has led to the development of specialized ceramics, such as Zerodur®, which achieves record low thermal expansion, approaching 10^{-9} K^{-1}, two orders of magnitude smaller than fused silica, which has the lowest coefficient of thermal expansion (CTE) among 'single material', and two to three orders less than Invar. The low CTE in Zerodur is achieved by adding two constituents in a composite, with one constituent exhibiting a negative CTE balancing the positive CTE of the other [22]. Further efforts have been made in the search for negative CTE materials in complex material systems [23, 24].

Fused silica is applied for high precision devices and optical elements partly because of its low CTE, to maintain high dimensional stability. In addition, the positive temperature-elastic coefficient of this material offers further improvements to the thermal stability of devices. For

instance in watchmaking, the temperature-induced frequency deviation of a silicon-based mechanical oscillator is minimized by compensating the negative temperature-elastic coefficient of silicon, with the positive temperature-elastic coefficient of silica. This composite-like material is known under the brand Silinvar® [25] which is the successor of Elinvar® and Nivarox®. For Silinvar®, an oxide layer is grown onto a silicon substrate, forming an SiO_2 layer. The main limitation of Silinvar is the growth of the oxide layer, whose thickness is limited to a maximum of approximately 4 μm due to practical reasons, unfortunately limiting the freedom in design.

A thermal expansion scheme, which makes use of fused silica's positive temperature-elastic coefficient was invented for mirrors, acting like test masses, in the gravitational wave detection project LIGO [26, 27], with the purpose to suppress thermoelastic losses [28]. The mirrors are suspended by 800 μm diameter silica fibers, as shown in Figure 1.3. The weight of the mirrors stresses the suspension and the resulting initial strain is a function of the Young's modulus ($\epsilon = \sigma/E$, Hooke's law). Due to the positive temperature-elastic coefficient, ϵ becomes smaller for elevated temperatures, causing the mirror to move upwards (right schematic of Figure 1.3a). While for the positive thermal expansion of fused silica at room temperature, the strains become larger, and the mirror moves downwards (schematic in the middle of Figure 1.3a). They demonstrated that a relatively low tensile stress, in the order of 175 MPa, is needed to compensate for the low thermal expansion coefficient. For their application, this method was sufficient to suppress the (already low) thermoelastic losses of fused silica below the detection limit of the gravitational wave detector [28, 27].
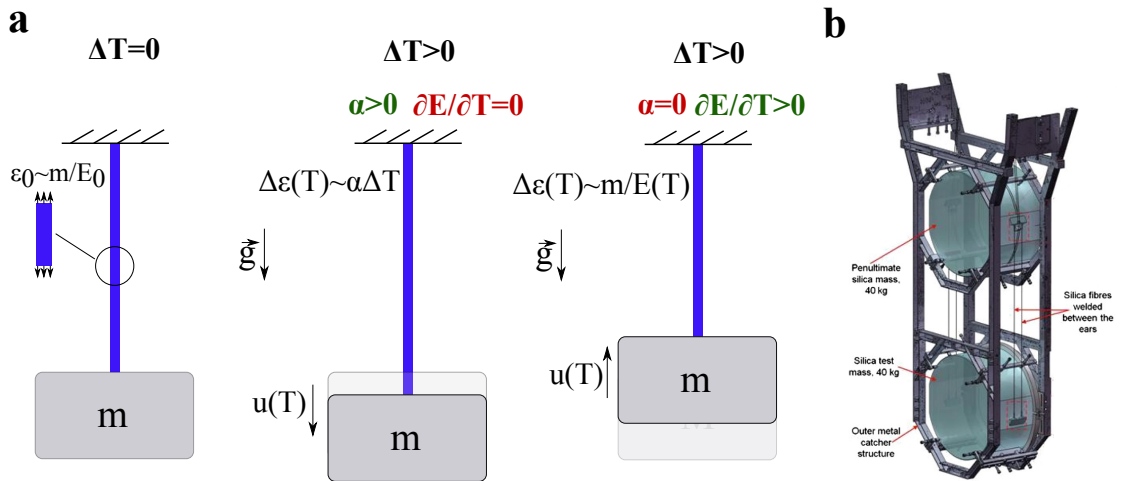
Figure 1.3 – a) *The thermal expansion principle for LIGO's test-masses/mirrors. For simplicity, the two prominent thermal expansion effects are separated. In the left, no temperature change is applied, the strain ϵ_0, in the SiO_2 fiber is constant and is a function of the weight (m) and Young's modulus (E_0). For the situation in the middle, a temperature increase is applied, consequently a downward thermal movement of the mass, accounted to the positive CTE, is illustrated. In the right schematic, an upward thermal movement of the mass due the positive temperature-elastic coefficient occurs. Furthermore, the latter is a function of the initial strain ϵ_0, or in other words the load.* **b)** *CAD-drawing of the test masses, adapted from [26].*

Let us discuss briefly the ancestor of the Elinvar® made oscillator, as it is fruitful for further thoughts. Nearly 300 years ago, the oscillator was comprised of a thermal compensation balance wheel, see Figure 1.4. Masses attached to a bimetalic strip, move radially, either inwards or outwards. This thermally-induced movement changes the inertia, such that it compensates for temperature-dimensional and -elastic change of the oscillator itself.
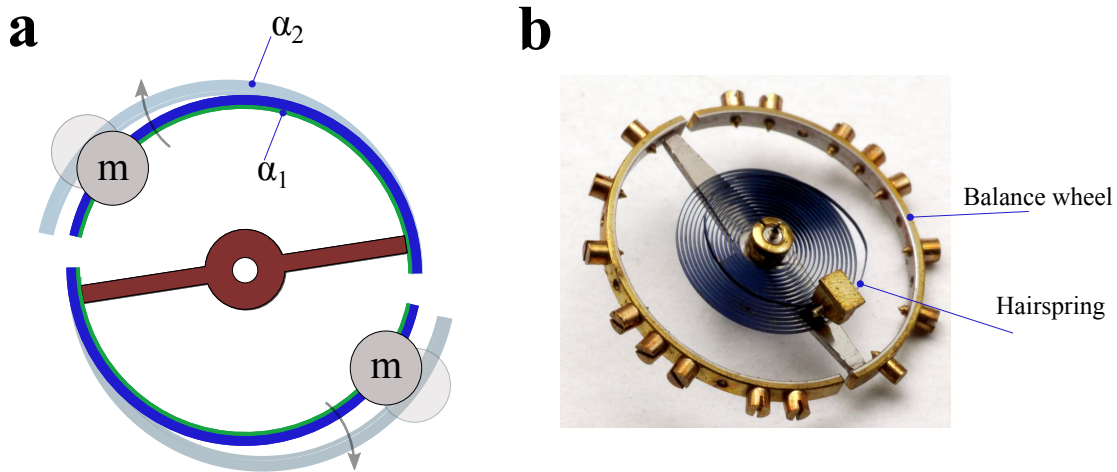
*Figure 1.4 – The thermal compensating balance wheel, invented in the 18th century by Thomas Earnshaw for watchmaking. **a**) The radial mass position is controlled by a bimetallic rim. In effect, the inertia is controlled thermally. **b**) An impression of an hairspring and balance wheel assembly. The image is adapted from the website https://www.vintagewatchstraps.com/.*

Another approach to tune macroscopic material properties is based on metamaterials, where a repeating microscale unit-cell has a programmable CTE, dictates the effective CTE of the metamaterial at the macroscale. This microscale unit cell consists of a truss-like architecture, made out of different materials, having different positive CTEs [29, 30]. Figure 1.5a depicts the CTE versus a design parameter for different metamaterial designs [31]. Although of large scale (>1 mm), it demonstrates these theoretical models for tuning and optimizing thermal expansion behaviors. These unit-blocks are an assembly of aluminum, a high-CTE material, and titanium bars, a low-CTE material, made with conventional fabrication technologies. Recent progress in additive 3D-polymerization techniques have enabled the implementation of composite microstructures [32, 33], see Figure 1.5b. For both examples, a lower effective CTE is achieved than the individual constituents, and notably, for certain design parameters, negative CTE values are obtained.

Most concepts discussed so far, use two or more constituents with distinct thermomechanical behaviors. There, the constituents display opposite thermal behaviors (as in the case of Zerodur® and Silinvar®) to minimize undesired effects. Other solutions are found at the system level, where degrees of freedom are added. Allowing for internal temperature induced movements, while at the outer-boundary, the structure exhibits a defined thermal expansion

behavior (as in the case of the gridiron pendulum and for metamaterials). The latter method requires the ability to fabricate multiple materials based three dimensional structures, where the additive fabrication methods are particularly effective. The last method found in the literature controls the stress such that the initial induced strain varies upon a temperature change, due to the temperature-elastic coefficient. This method was used for the gravitational interferometer (LIGO).
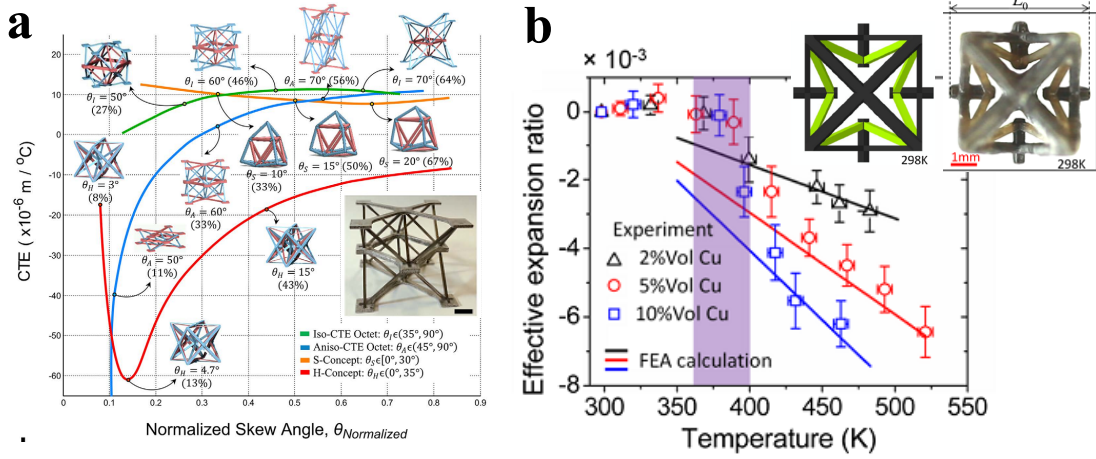
Figure 1.5 – *Two demonstrations of CTE tuneable metamaterials. In both examples, a lower effective CTE is achieved than the individual constituents. For certain parameters, negative CTE values are obtained. **a**) Set of different aluminum-titanium structures mapped to their effective CTEs and for a design parameter [31]. **b**) The effective thermal expansion of a metamaterial versus the temperature. The effective thermal expansion is further tuned with respect to the copper additive concentration [32].*

Controlling thermomechanical properties with meta-material approaches are promising for increasing the material selection. However, the accuracy on the designed properties remains limited, see Figure 1.5. This is either because of a lack of control on the fabrication technologies or due to parasitics effects imposed by assembly steps. Post-tuning the properties, i.e. in a closed-loop manner, is a possible method to reduce uncertainties, which these approaches seem not to offer. Unfortunately, the removal of material to create the necessary internal degrees-of-freedom reduces the stiffness of the meta-material [30], which is undesired in most cases.

We envision that the principles mentioned above could be integrated in a thermomechanical tuning method which is based on femtosecond laser exposure of transparent materials. This could offer several advantages with respect to other methods, because of the ability of e.g.; tuning locally the material properties in any location of the transparent material. The method we envision is further detailed in Section 1.3, but let us first introduce the ultrafast laser technology and how it is used for tuning material properties and the creation of multifunctional devices.

1.2 Ultrafast laser processing of transparent materials

Tightly focused ultrashort laser pulses focused inside a transparent material trigger non-linear absorption events, eventually leading to localized bulk modifications [34, 35]. For a variety of transparent materials, different types of laser-induced modifications can be found depending on exposure conditions. For instance, in fused silica, for relatively low pulse energies (< 200 nJ) and short pulse duration (< 200 fs), homogeneous modifications associated with a refractive index increase were reported [36], while increasing the pulse energies and/or the pulse lengths, leads to a second characteristic modification characterized by self-organized nanostructures with nanoscale periodicity, referred as 'nanograting' or 'type II modification' [37]. The relation between laser-induced structural changes and exposure conditions are discussed in more details in the next chapter.
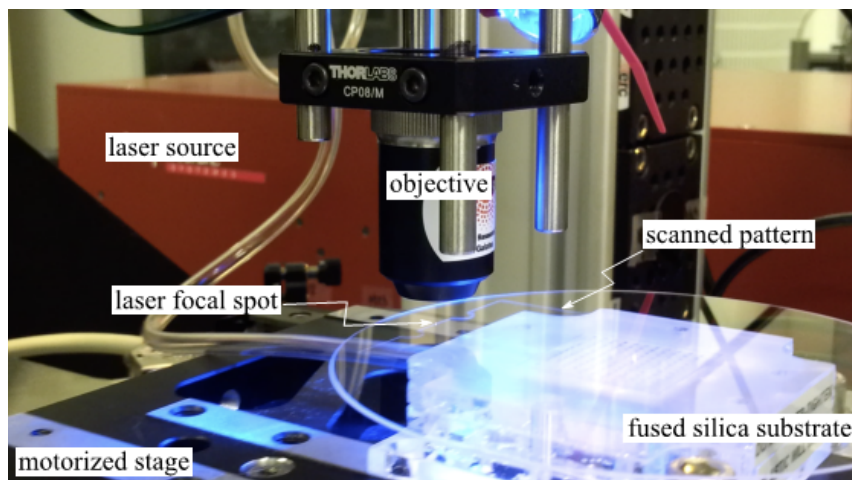
Figure 1.6 – An example of ultrafast laser machining setup: a femtosecond laser is tightly focused inside a fused silica wafer, and by means of translation stages, the focal spot is moved along an arbitrary trajectory.

The very nature of non-linear absorption, that confined energy in the bulk of the material makes possible the writing of 3D patterns, opening the door to new applications exploiting a three-dimensional design space. An interesting property of this second type of modification is the local increase of etching rate when immersed in low-concentration hydrofluoric acid [38] or KOH [39]. There, the etching rate increases significantly compared to unexposed material, typically to a ratio of 1:100 or even more with KOH, making possible the fabrication of arbitrary high-aspect ratio structures [40]- the schematic of the fabrication process is depicted in Figure 1.7a. Using brittle materials such as glass for fabricating mechanical structures may sound counter-intuitive, as fused silica – like other glasses, has a low toughness. This problem is mitigated by the fact that femtosecond laser exposure combined with chemical etching (in HF) yields to higher quality, defect-free surfaces, preventing the occurrence of crack nucleation sites. The tensile strength of femtosecond micro-machined fused silica show values well above 1 GPa with low failure probability [41], and eventually reaching 2.4 GPa [42], substantially above ordinary metals. As a material, fused silica happens to have one of the lowest internal

friction coefficient, and as such, has nearly no stress-strain hysteresis or thermoelastic losses. Together with its low thermal expansion, fused silica is particularly appealing as a construction material for high-precision mechanics. In Figure 1.7b, a femtosecond laser fabricated 3D cross-pivot is depicted [43]. This structure illustrates the true 3D nature of this manufacturing process as such device can not be fabricated with conventional lithographic methods. Another feature, which is not possible to fabricate with conventional processes, are hollow-cavities or fluidic channels [44, 45, 46]; Figure 1.7c depicts a SEM image of a fluidic channel realized with the ultrafast laser machining process. As an illustration of the potential of this technology for integrated devices, fluid-handling and mechanical elements have been integrated into one monolithic device, a medical device for surgical puncturing illustrating this idea is shown in Figure 1.7d. The motions of the needle are precisely controlled by a bistable flexure-based mechanism, ensuring a repeatable and safe puncturing. A fluidic channel is added to the needle for drug delivery. Figure 1.7e depicts a schematic of a mirror suspended by a set of flexures, which defines a virtual rotation point at the mirror's surface [47]. The orientation of the mirror is itself controlled by means of femtosecond laser exposure of certain locations on the flexures to induce the motion of the mirror.
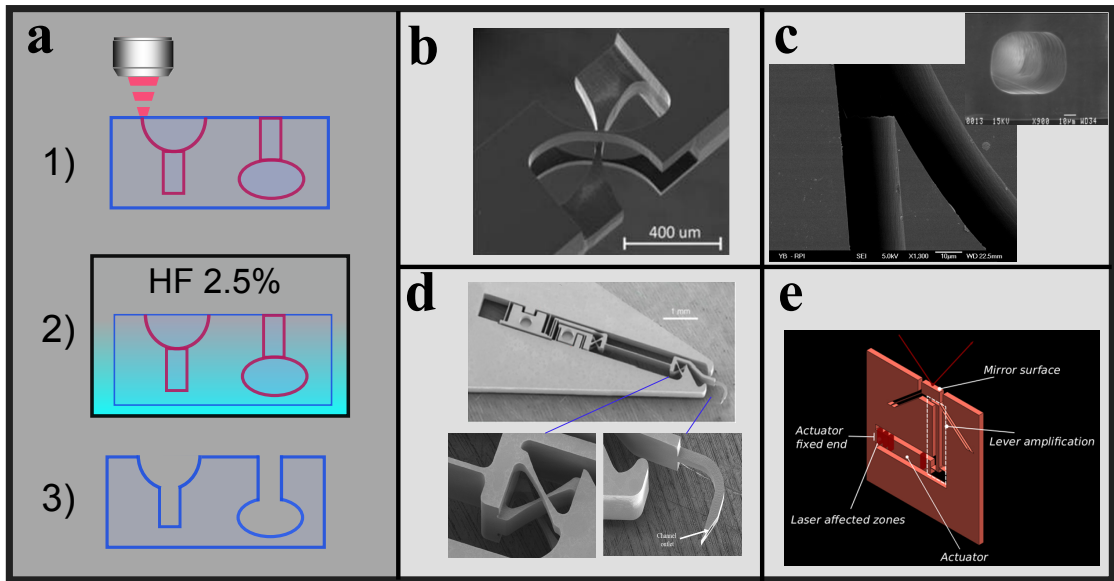
Figure 1.7 – a) *Femtosecond laser microfabrication process steps.* ***b-d)*** *Examples of monolithic mechanical elements or systems which has been fabricated using the process in* ***a)***, ***b)*** *a cross-pivot [43],* ***c)*** *branching fluidic channel [40],* ***d)*** *a medical device for surgical puncturing, an assembly of mechanical flexures with an integrated fluidic channel for drug injection.* ***e)*** *A mirror suspended in a set of flexures defining a rotation point. The mirror can be reoriented by post-exposing a part of the mechanism [47].*

In photonics, various functionalities inscribed with an ultrafast laser in fused silica have been demonstrated. Davis *et al.* demonstrated, in their pioneering work, that a low-pulse energy regime modification is associated with a homogenous refractive index increase in silica [36]. This type of modifications is since then referred as 'Regime I' modification in the literature. As a consequence, they further showed that a written line acts as an optical waveguide [36], see

Figure 1.8a. The refractive index changes are achieved in the range of 10^{-4} to 10^{-3} [48, 49], which is similar as the one of conventional monomode optical fibers. The reported losses are in the order of 0.1 dB/cm.

This property change has been further extended to more complex optical networks i.e. waveguide coupling [50, 51], photonic lanterns [52, 53], Bragg gratings [54] used as strain sensors [55, 56] or either as an end-reflector in an optical cavity [57, 58], and at last active photonic devices like waveguide amplifiers and lasers [59].

The Regime II modification is characterized by a strong form-birefringence (10^{-2}) [60, 61], due to a spatial modulation of the refractive index within the focal volume. Nano-structuring the material in arbitrarily location offers the possibility to design sophisticated optical retardance patterns, such as waveplates or polarizers [62], (Figure 1.8b). This strong birefringence property offers promising ideas for high-density data storage as shown in the lower right part of Figure 1.8b. This type of data storage would theoretically allow for 360 TB/disc of capacity and have a theoretical life time of 13.8 billion years at temperatures below 200 °C, because of their high thermal stability [63].
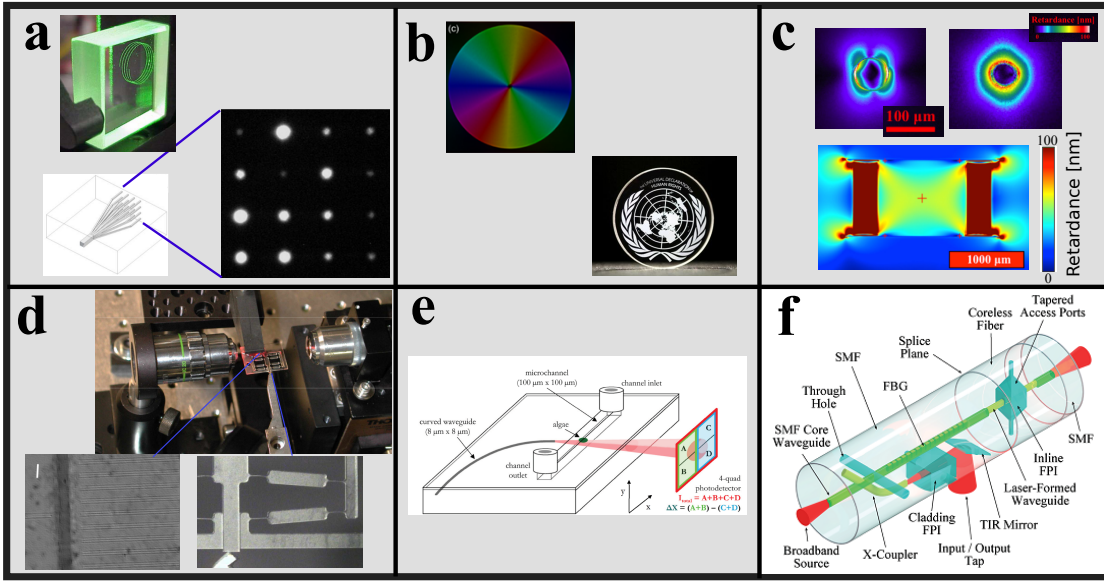
*Figure 1.8 – Examples of laser written functionalities in photonics (**a-c**) multifunctional devices combining waveguides with optics and mechanical elements(**d-f**). **a**) Ultrafast-laser written waveguides, produced with Regime I modifications. **b**) Ultrafast-laser written optical retardance patterns, produced with Regime II modifications: top, a radially polarized vortex converter [62]. Bottom right, an example of laser written data storage, here, the universal declaration of human rights. **c**) Optical retardance based on stress-induced refractive index changes [64]. **d**) Opto-mechanical device; a flexure-based translation stage with an integrated encoder use as a sensor [65]. **e**) Opto-fluidic chip for algae detection [66]. **f**) Lab-on-a-fiber; various laser written optical elements, such as waveguides, waveguide couplers, Bragg gratings, and fluidic channels.*

Both types of modifications, Regime I and II, undergo a volume change [67], inducing anisotropic stress in the surrounding pristine material, which in turn, as a consequence of the elasto-optic

effect, manifest itself in an anisotropic refractive index change around the laser-affected region. This property can be exploited to realize waveguides [68], waveplates [64, 69], and polarizers [70], see Figure 1.8c.

In this new multifunctional manufacturing paradigm, assembly steps can be omitted, and hence positioning errors when transferring from one process to another are avoided. The symbiotic combination of optical functions and structural ones using a single process leads to multifunctional monolithic devices [71], such as opto-mechanical or opto-fluidic devices [72, 44] as depicted in Figure 1.8d-f. The optomechanical device, in Figure 1.8d, is a flexure based translation stage with a laser-written waveguide based displacement sensor [65]. The opto-fluidic device in Figure 1.8e, is capable to discriminate between different types of algaes, which are flowing via a microscale fluidic channel [66]. In Figure 1.8f, optofluidic capabilities are integrated inside an optical fiber [73], with various types of optical components. This device is meant to sense multiple measurands, such as temperatures and strains, and offers a platform for in-fiber fluorescence detection or absorbance spectroscopy.

To summarize, femtosecond lasers can be used for the fabrication of highly integrated multifunctional microscale devices in fused silica. Being able to shape and tailor the material properties of a material like fused silica gives an appreciable advantage for the fabrication of precision instruments. Further attractive aspects of this fabrication techology are; localized tuning of material properties, the creation of microscale 3D shapes, assembly steps are omitted (or minimized).

1.3   Proposed method

Investigating the thermomechanical properties of ultrafast laser exposed fused silica is a rich topic to study. We foresee different methods for controlling them. Using ultrafast laser technologies, microscale volumes can be transformed in any location of an arbitrarily shaped transparent material, as illustrated in Figure 1.9. In particular, femtosecond laser exposure display several types of modifications with distinct morphologies, optical properties and densities, depending on laser-exposure conditions. Complementary to this, it is expected that these types of modifications exhibit distinct thermomechanical properties, offering an opportunity for continuous material properties tuning. As discussed in the previous section, femtosecond laser machining is capable of creating complex 3D mechanical shapes at the micrometer scale, see Figure 1.7. This gives the possibility to design metamaterial like structures in a monolith. Another method we foresee, consist in tuning the thermal expansion by controlling of laser induced stress fields, creating similar conditions to the case shown in Figure 1.3, but this time in a monolithic design. This type of material property tuning is likewise applied for optical components, see Figure 1.8c, although in that case the refractive index is tuned.

This method based on local tuning of thermomechanical properties using ultrafast lasers, offers not only the possibility to create new types of materials, but also to post-tune the thermal
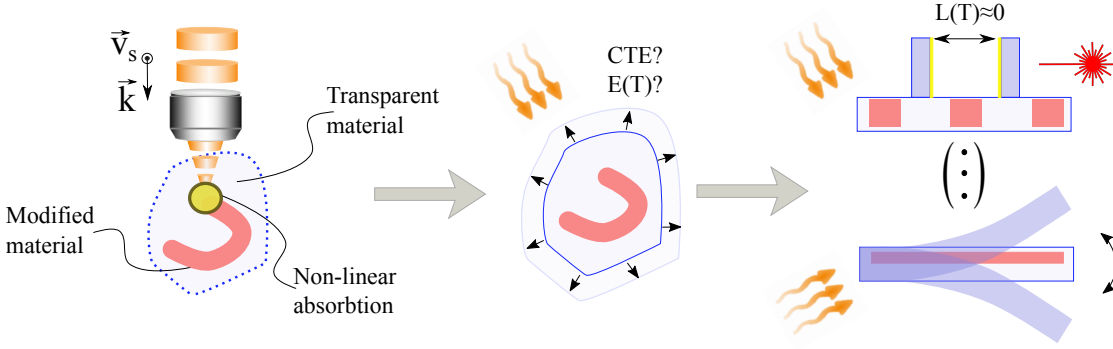
Figure 1.9 *– An overview of the proposed method used in this thesis for locally tuning thermomechanical properties. Left, schematic of ultrafast laser exposure of a transparent material. The middle figure illustrates the research question; what are the thermomechanical properties of ultrafast laser exposed fused silica? Right, illustrations of possible applications this research can lead to: for example, the reduction of thermal-dimensional changes of an optical resonator, or the creation of thermal actuators.*

behavior of a device made with the same technology. The ability to tune properties in the thermomechanical domain with a femtosecond laser would enlarge the potential for making highly integrated multifunctional devices. Furthermore, the control on the thermomechanical properties could further increase the performance of the devices mentioned in the review above, by increasing dimensional stability or a better control of parasitic deformations. Examples of applications could be the reduction of thermal dimensional changes of optical resonators or the creation of thermal actuators, see the right schematic in Figure 1.9. Note, the latter example could typically be itself the building block of a metamaterial or a part of the compensation mechanism like depicted in Figure 1.4.

1.4 Objectives and thesis outline

In this work, we propose an approach based on femtosecond laser exposure to *locally* engineer the CTE of bulk fused silica, according arbitrary shapes and *without adding any material* to the raw substrate.

Specifically, the objectives are;

1. To demonstrate experimentally that non-ablative ultrafast laser exposure can effectively affect the thermomechanical behavior of fused silica.

2. To characterize the thermomechanical properties obtained for a variety of exposure conditions.

3. To propose a model and a framework for predicting how laser-modified glass will behave.

This document is subdivided in two parts;

Part I describes the essential background information about ultafast laser exposed fused silica and formulates the problem in terms of locally varying thermomechanical properties and discusses inherent challenges related to the characterization of locally changed thermomechanical properties (Chapter 2). The measurement principles used in this work are explained in full details in Chapter 3. The last chapter of Part I, Chapter 4, explain the design and validation of the experimental-setups.

Part II embodies the characterization results made in this work. Chapter 5 discusses the results related to tuning the Young's modulus through direct laser-writing. There, we introduce a mathematical framework for predicting the Young's modulus for a given nanostructure orientation. Chapter 6, discusses the laser-tuned temperature dependent Young's modulus. An appreciable large part of this chapter is on the interpretation of this material property. Chapter 7, discusses the CTE change, where we demonstrate two distinct behaviors for two types of modifications. In the final chapter of Part II, Chapter 8 discusses the effect of thermal annealing on the thermomechancial properties. There, we could further relate the contribution of certain modification characteristics to the thermomechanical properties changes, such as the contribution of point defects or densified zones.

In the conclusion, we summarize the main results of this thesis work, the potential use of these findings and further research directions.

Methods Part I

2 Problem statement

One of our objectives is to control the macroscopic thermal expansion of fused silica by locally changing thermomechanical properties using ultrafast lasers. If there exists a change in thermomechanical properties after laser exposure, we envision various ways to control the thermal expansion behavior of a given material, for example, by selecting a certain type of modification, by changing the exposure conditions or by changing the volume fraction of the modified material. Towards this goal, we first need to review the key characteristics of laser-modified fused silica. Second, we describe which material properties are of importance based on background information and our existing knowledge of the thermomechanical behavior of bulk fused silica. As it turns out, the CTE is not the only material property of importance. Third, we briefly discuss the known methods used to characterize these properties. There, we introduce two characterization methods which are used in this work and explain the motivation behind these choices. Finally, at end of this chapter, a set of equations and conventions, used throughout this document, are defined.

2.1 Ultrafast laser exposed fused silica

Ultrafast laser micro-machining technologies make use of non-linear absorption phenomena to modify transparent materials such as glass. This effect can be triggered by a tightly focused ultrashort laser pulse in the bulk of the material. The threshold power intensity for material modifications to occur in fused silica is in the range of 10^{13} W/cm^2 [74]. At these laser intensities, the photon density is sufficiently high to ionize the material, by means of multi photon interactions. These interactions create seed electrons in the valence bands that further trigger additional absorption events like avalanche and tunnel ionizations [75]. When the free electron density exceeds a certain value, excited electrons behave like plasma. At a time scale of 10^{-15} to 10^{-12}s, a temperature rise occurs in the plasma due to collisions of the excited electrons with the glass matrix [76]. At these timescales and power intensities thermal diffusion can occur, although it is negligible. The plasma induced localized pressure change in the exposed volume generates a shockwave [77]. Sub-picoseconds after the shockwave emission, thermal diffusion occurs. The exposed volume cools down and converges to

equilibrium in the order of a microsecond [78]. The events described so far are caused by a single pulse, but are repeated for every subsequent pulse. The modified volume evolves in size [79, 80], structurally [81], material property changes [49] and point-defects density [82], with the number of pulses on one spot. Furthermore, as we will see later, for certain exposure conditions, the pre-modified material, due to previous pulses, triggers additional events leading to different types of modifications. Apart from the number of pulses on one spot, other exposure conditions have a significant contribution to the modification taxonomy, such as the intensity of a single pulse and its duration, the separation time between two pulses, confocal parameters and the laser beam polarization.
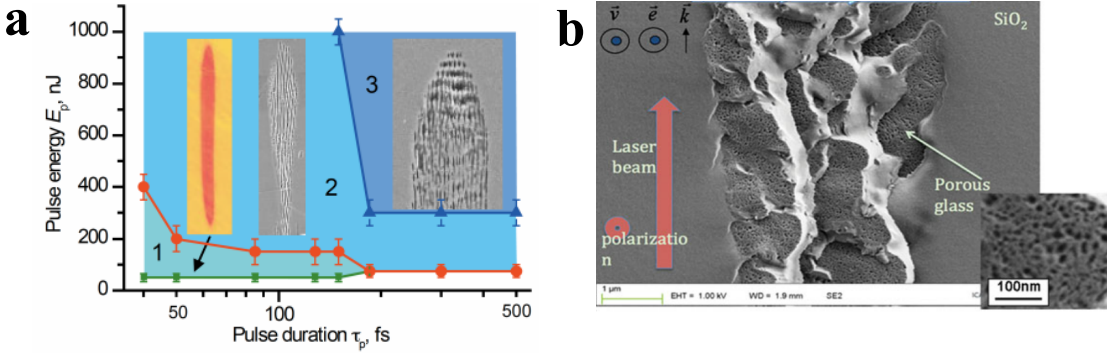
Figure 2.1 – a) Taxonomy of three types of modifications as a function of pulse duration and pulse energy, [83]. 1) Homogenous modification (Regime I), 2) nanograting modification (Regime II) and 3) a chaotic variant of a nanograting modification. **b**) A scanning electron microscope (SEM) image of a cleaved sample, revealing nanopores in a nanograting type of modification, [84].

Just above the modification threshold, a regime (so-called 'Regime I') is found for low pulse energy (<~ 200 nJ), and pulses shorter than 200 fs, as indicated in Figure 2.1a. These structural modifications are characterized by an apparent homogeneously modified volume, in which a higher refractive index is observed [36]. The change in refractive index is explained by a local densification of the material [85, 79]. The change in volume has been confirmed using a direct method, based on micromechanics [67].

Increasing further the pulse energy under similar pulse durations yields another type of modification (so-called 'Regime II'), see Figure 2.1a, characterized by the occurrence of self-organized, periodic structures spaced by roughly half the laser wavelength [86, 87], and commonly referred to as nanogratings [88]. These periodic arrangements of nanoplanes exhibit strong form-birefringence [60] that indicates a fine modulation of the refractive index. Later, it was shown experimentally that these nanoplanes consist of a porous structure [84], as shown in Figure 2.1b. Using SAXS analysis, the porosity was further investigated and two pore diameters (10 and 30 nm) were found inside these planes [89]. Raman spectroscopy pointed out the appearance of interstitial oxygen atoms [84, 67], which is highly likely present in the pores. Contrarily to the Regime I modification, this regime is associated with a net localized volume expansion [90]. Postmortem experimental studies show a clear evolution of the self-organization mechanism with an increasing number of incoming pulses [91, 92], as shown

in Figure 2.2a, with a temporal pulse separation far longer than the lifetime of the induced plasma and self-trapped excitons [93]. The orientation of the nanogratings are controlled by the laser polarization, the nanogratings are aligned perpendicularly to the laser beam's electrical field. Figure 2.2a depicts SEM images of the nanograting modification for three different polarization directions. This property offers the possibility to control the laser-induced anisotropy which has been proven to be useful for the control of the anisotropic etching-rate [94], the form-birefringence fast axis control [62], and the anisotropic expansion-induced refractive index change [70].
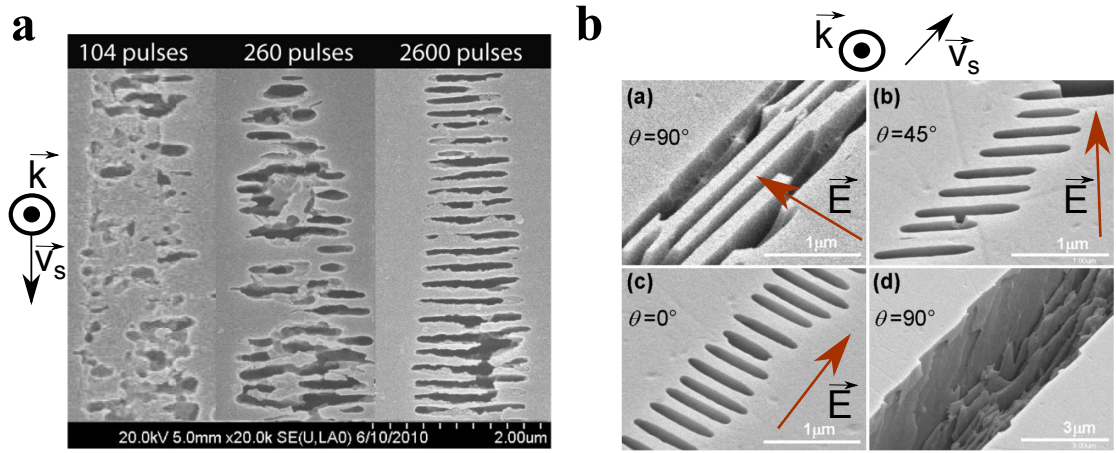
Figure 2.2 – *SEM images of laser exposed fused silica in the second regime. The laser is scanned with a certain velocity across the sample, $\vec{v}_s$ denotes the scanning direction and $\vec{k}$ laser beam propagation. The samples are cleaved, polished and briefly etched with hydrofluoric acid.* **a)** *Three exposures with an increasing number of pulses on one spot [87].* **b)** *Three polarization states; the nanogratings are orientated perpendicular with respect to the laser-beam's electric field, $\vec{E}$, [94].*

A universal model, which explains the essential physical processes that lead to nanograting formation, is to date not widely accepted. Here, we summarize a few of the main proposed hypotheses, others can also be found in [95, 96, 97, 98]. Shimotsuma *et al.* suggests a spatial modulation of the intensity due to the inference of the incident-light field with the electrical field of the plasma wave [99]. This hypothesis is not acknowledged for a set of reasons; 1) this hypothesis indirectly suggests that a single pulse is sufficient to trigger the self-organised behavior, however observations pointed out that the nanogratings are formed progressively as function of subsequent pulses. 2) to meet with the necessary oscillating frequency of the electron plasma waves, a minimum plasma temperature is required. However, in other works, it appeared that nanogratings are formed at significantly lower plasma temperatures - conducted from an energy budget. Another model was proposed, by Bhardwaj *et al.*, based on a local enhancement of the intensity due to generation of nanoplasmons [100]. In this model, the plasmons are created due to a dielectric difference, i.e. by pores or point-defects. The local plasma inhomogeneity evolves from a dot to a sheet like shape perpendicularly to the polarization. This model would explain the pulse-to-pulse evolution, with the pre-modified material being a precursor and the very localized decomposition of the SiO_2 molecule. In addition, to explain the self-organisation mechanism, it is suggested that the plasma

planes act like metallic waveguides. The lowest modes are supported, if the spacing between plasma-planes are near the incident light wavelength, explaining the periodicity. However, nanogratings in an already porous fused silica are also created with ultrafast laser exposure. Those structures share the same characteristics as the ones created in a non-porous fused silica, albeit with a spacing of alternating layers significantly smaller, $\lambda/10$ [101, 96]. This finding suggests that the spacing between the nano-layers is not only dictated by the laser's wavelength. Moreover, although the periodicity scales clearly with the wavelength [87], it significantly decreases with an increasing number of pulses- typically with layer spacing starting above $\lambda/2$n converging to values below it [99, 87]. This is pointed out in the work of Rudenko *et al.*, who performed numerical simulations of pre-modified material and demonstrated that the periodicity is related to the concentration of inhomogeneities (defects and/or pores) [102, 103] - indirectly also as function of the number of pulses. According to this work, the incident wave interferes with scattered near field waves emitted by nanoplasmas.
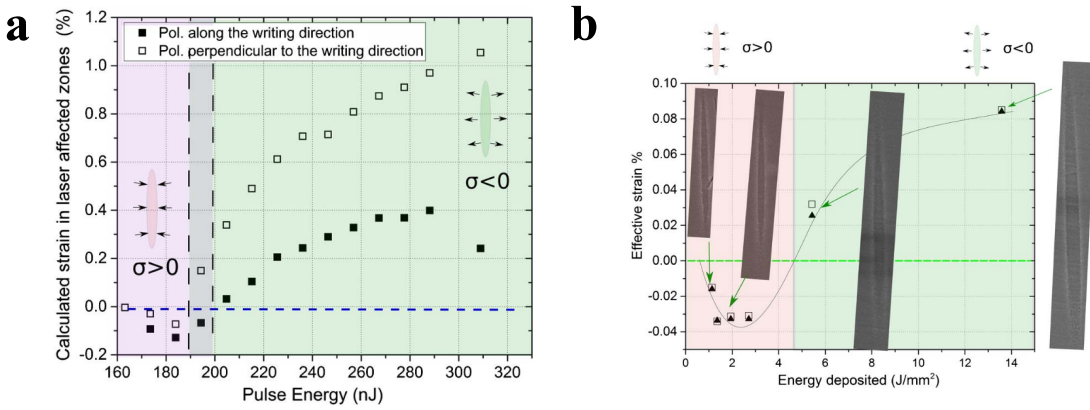
Figure 2.3 – *The experimentally determined volume change, with the aid of micromechanics, of the laser modified volume [67].* ***a****) The volume change as function of the pulse energy. This finding correlates well with Figure 2.1a, a Regime I modification below a pulse energy 200 nJ and Regime II modification above a pulse energy 200 nJ.* ***b****) The transition between a Regime I and II modification as function of the deposited energy.*

Although, the relation between laser-parameters and taxonomy is understood for a large part, still new findings are reported, refining the understanding, raising new questions and challenging the aforementioned models. For example, the transition from a Regime I to II modification is not only dependent on the pulse-intensity and -duration, but also on the deposited energy. Bellouard *et al.*, [67], showed with a micromechanical based method that the volume changes invert with an increasing deposited energy, see Figure 2.3. Furthermore, it appears that the confocal parameters have a significant contribution to exposure condition values of the Regime I/II transition. In [104], a collection of studies is reviewed and the taxonomy map versus the pulse energy and numerical aperture is assessed. Another regime, the cumulative regime, occurs when the separation time between two pulses is shorter than the cooling time, about μs, of one pulse [105]. The temperature accumulates with each pulse and goes beyond the melting temperature. In this regime, the nanogratings are erased - and self-organized bubbles are formed. Rudenko *et al.*, [106], reviews this behavior and studies the

erasure as function of the deposited energy. However, Kissi *et al.* reported that nanogratings "reappear" when the deposited energy is increased even further [107].

In the last two decades, large progress has been made in exploring and understanding the ultrafast laser-induced modifications in fused silica, with still unanswered questions and room for further exploration. Despite the gap of knowledge, this process has also proven its applicability in the fabrication of multifunctional devices, discussed in the pervious chapter. To the collection of studies, we would like to add the study of thermo-mechanical behavior of the ultrafast laser modified fused silica. This is to our best knowledge not done by previous works.

2.2   Analytical description

An important material property to characterize is the CTE. As a matter of fact, it is the only material property of importance, when the material can thermally expand freely, hence its not kinematically over-constrained, or when the material is homogeneous, hence without local CTE differences. However, in an over-constrained case or for an inhomogeneous material, the elastic properties become important. The CTE mismatch induces a stress upon the neighboring constituents, constraining the expansion of the material and leading to stress build-up. For a one-dimensional case and a linear elastic material, the thermal strain (ϵ_T) for a single constitute is defined as depicted in equation 2.1.

$$\epsilon_T = \frac{\sigma_{\alpha,T}}{E_T} + \alpha \Delta T \tag{2.1}$$

$\sigma_{\alpha,T}$ and ΔT are the stress due to CTE difference and temperature change, respectively. The material properties E and α are the Young's modulus and CTE, respectively. The subscript $\cdot_T$ indicates that the parameter is temperature dependent. We consider in this work that α is temperature invariant. The first term describes the strain due to thermal expansion mismatch and depends on E_T. The second term describes the thermal strain as a function of the CTE and the temperature difference.

In the previous section, we saw that the laser-exposed volume undergoes a volume change. This situation is schematically illustrated in Figure 2.4. A fused silica sample is locally laser exposed with an arbitrary pattern, in red, and to be called laser affected zone or "LAZ". The cross-sectional magnified view is given, in the left, for two type of modifications, Regime I and II. The Regime I modification undergoes contraction (ϵ_0) and imposes a tensile stress on the surrounding material (σ_0). On the contrary, the Regime II modifications expands ($+\epsilon_0$) and a compressive stress is imposed on the surrounding material. Note that the subscript $\cdot_0$, indicates that the stress and strain are temperature independent. Adding the additional strain
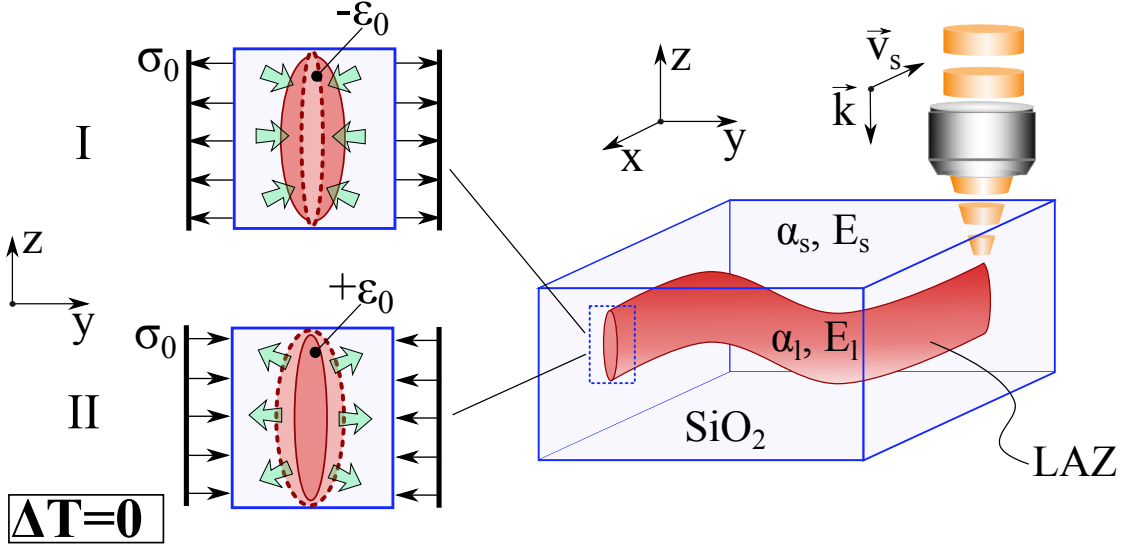
Figure 2.4 *– Right: an arbitrary laser exposed volume, shown in red and called "LAZ". The material properties α and E are indicated for the exposed and pristine volume. Furthermore, the translation and laser propagation direction is defined with the vectors $\vec{v}_s$ and $\vec{k}$, respectively. The two expansion situations depicted in the 2D magnified views for which no temperature variation is considered. The regime I modification is given at the top; the modified volume undergoes a contraction ($-\epsilon_0$) and creates tensile stress in the surrounding material. The regime II modification is given below; the modified volume undergoes an expansion ($+\epsilon_0$) and creates compressive stress in the surrounding material.*

component, equation 2.1 writes:

$$\epsilon_T = \frac{\sigma_{\alpha,T}}{E_T} + \alpha \Delta T + \frac{\sigma_0}{E_T} \tag{2.2}$$

The added third term denotes the thermal strain due a constant imposed stress, which in other words captures the prestressing effect of the laser exposure. This term is thermally dependent, since the Young's modulus (E_T) is itself temperature dependent. Note that contribution of this term depends on the sign and magnitude of σ_0. Deriving the effective CTE, by differentiating equation 2.2 with respect to the temperature and around $\Delta T = 0$ gives:

$$\left.\frac{\partial \epsilon_T}{\partial T}\right|_{\Delta T=0} = \alpha + \left(\frac{1}{E_T}\frac{\partial \sigma_{\alpha,T}}{\partial T} - \frac{\sigma_{\alpha,T}}{E_T^2}\frac{\partial E_T}{\partial T} - \frac{\sigma_0}{E_T^2}\frac{\partial E_T}{\partial T}\right)\Bigg|_{\Delta T=0} \tag{2.3}$$

Rewriting equation 2.3 and introducing a new variable $\beta = 1/E_0 \partial E_T/\partial T$, gives:

$$\left.\frac{\partial \epsilon_T}{\partial T}\right|_{\Delta T=0} = \alpha - \frac{1}{E_0}\frac{\partial \sigma_{\alpha,T}}{\partial T} - \epsilon_0 \beta \tag{2.4}$$

From equation 2.4 it becomes apparent that characterizing the CTE only is not sufficient. The

other material properties of the LAZ which should be characterized are E, β and ϵ_0. Note that $\sigma_{\alpha,T}$ is a function of the CTE difference, Young's moduli and temperature. Let us now examine what are possible characterization methods for both the Young's modulus and the thermal expansion.

2.3 Characterization methods

2.3.1 Survey of Young's modulus characterization techniques

Various methods exist for measuring Young's modulus. Some of them, such as tensile, torsion or bending tests, are based on applying a defined mechanical loading case, for which stress and strain information are retrieved and the Young's modulus is calculated from it. Other methods use plastic surface deformation, like for instance nano-indentation, or are based on the measurement of other physical properties that strongly depend on Young's modulus. This is for instance the case of mechanical resonance identification techniques.

For tests relying on a loading case, the difficulty arises when testing micro-scale structures. Alignment of the applied load, sensing of small displacements and forces, as well as the mounting and clamping of the specimen (especially brittle ones) and preparation of stress free specimens are common difficulties [108]. To tackle these issues researchers came up with several innovative solutions, including micro-beam testing [109, 110], bulge test [111] or monolithic on-chip tensile testers [112, 113]. The main advantages of a monolithic on-chip apparatus is that clamping and alignment issues are avoided, as the test specimen and the loading mechanism are both fabricated out of the same substrate. These structures are either loaded by means of integrated electrostatic comb-array [114, 115], thermal actuators [116], a nanoindentation tip [114]. Solutions for gauging the small load forces are based on i.e. electrostatic forces [116], a compliant lever system [117]. The small displacements are either measured in situ, using an SEM [118] or a TEM [119]; with the aid of an AFM [120]; with an integrated mechanical-amplified lever [115]; or with an integrated sensor such a capacitive sensor [121]. A monolithic in glass tensile tester, fabricated with the ultrafast laser machining technique, was realized by [42]. There, femtosecond laser exposure is used to apply a load, and the stress is measured by birefringence microscopy, while the strain is retrieved using a mechanical amplification, as illustrated in Figure 2.5b.

Nanoindentation force measurement on the other end, makes use of an indenter – i.e. a sharp-hard pyramidal tip, which indents the surface of the test-specimen. The material is expected to behave elastically at the onset of unloading. From this point forward, the measured load and displacement are used to determine the elastic parameters. The nanoindentation elastic theory makes the assumption that the material is a homogeneous continuum. Therefore, applying this technique to composites or thin-films, numerical simulations are needed to understand the microscopic stress-strain behavior at and in the vicinity of the indent location [122]. Related effects with nanoindentation are numerically-modeled, like the friction between

material and indent-tip [123]; pile-up and sink-in [124]; elastic-plastic behavior [125]; fiber constraints in fiber reinforced composites [126].

Finally, tests based on mechanical resonance are non-destructive tests, where the resonance frequency of a mechanical element is analyzed to determine the elastic constants of the material [127]. Micro- or nano-beams, either clamped at one or both sides, are used to measure the bulk properties or thin-films. Analyzing multiple vibration modes of thin plates have also been used to determine elastic constants and Poisson's ratio of an anisotropic material [128, 129, 130]. Noticeably and particularly relevant for this thesis work, the temperature dependent Young's modulus of fused silica was characterized by analyzing the resonance frequency of a long fiber or a bar in the 50s [131, 132].

In more recent works, the elastic constants of fused silica have been characterized with the use of Brillouin light scattering technique – based on inelastic interaction with photons and phonons [133]. In particular, this technique is used for in-situ measurements, for instance to retrieve the elastic constants during high compressive pressure and/or elevated temperatures. Guerette *et al.* characterized the temperature dependent Young's modulus using this method [134, 135].
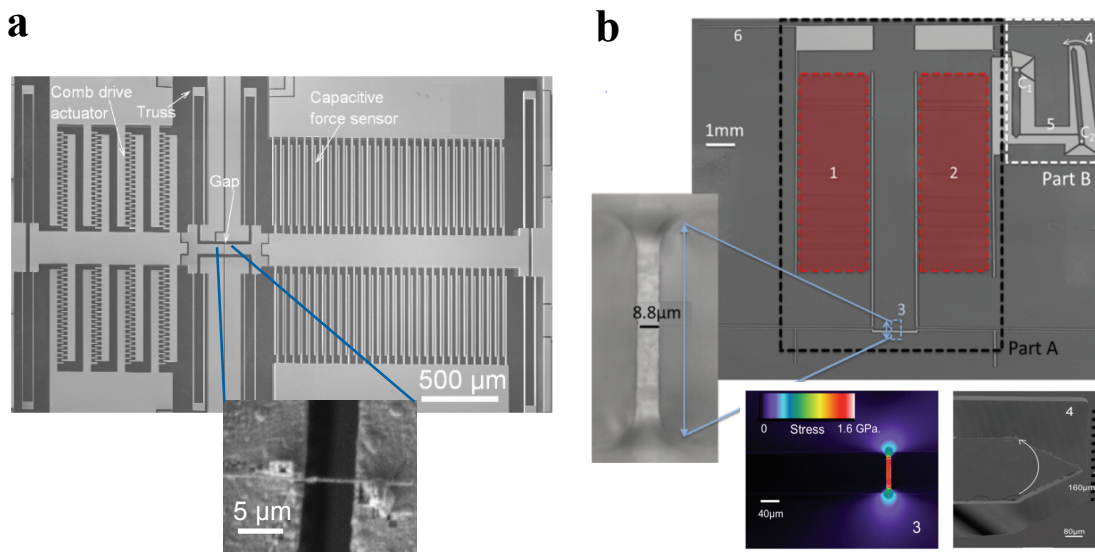
Figure 2.5 – Illustration of on-chip micro-tensile testers. *a)* A tensile tester where electrostatic force is applied and measured by a capacitive sensor. The test-specimen is not fabricated from the same material as the tester. *b)* A full monolithic fused silica tensile tester made with ultrafast laser machining technology. The force is created due to the volume expansion of the zones shown in red (1 and 2) using post-fabrication femtosecond laser-exposure steps. The stress is measured using the photo-elasticity effect, and more specifically birefringence microscopy (as shown in inset 3). Finally, the mechanical amplified displacements are monitored optically (part 4).

Let us summarize what has been reviewed so far and make critical notes with respect to our goals. Although, the methods for characterizing macroscopic material properties are well established and standardized, the characterization of microscopic material properties remains

challenging. Tensile test like methods provide a direct measurement of the elastic properties, however a great deal of effort must be made to minimize parasitics effects, like friction, and measure the small forces and displacements. The on-chip tensile test method is not very attractive when measuring temperature dependence of elastic properties. Determining the stress-strain curve for a large set of temperature setpoints is a time consuming procedure. Furthermore, the integrity of the on-chip force- and displacement-sensor might not be maintained throughout the heating and cooling process. Nanoindention is mostly popular for studying bulk materials, especially because of the simple sample preparation procedure as it can be applied locally anywhere on a material surface. Nonetheless, this technique must be accompanied with numerical simulation, especially when dealing with inhomogeneous materials. Mechanical resonance and Brillouin light-scattering methods are very attractive for characterizing the thermal elastic properties, as it gives a nearly instantaneous measurement. Additionally, Brillouin light-scattering method is capable of probing locally inside a transparent material. However, yielding for both methods, knowledge must exist about temperature dependency of other material properties. Brillouin light-scattering method requires the knowledge about the temperature dependent density (thermal expansion) and refractive index, where for the mechanical resonance methods the knowledge of the temperature dependent density is sufficient. The temperature dependent refractive index of the ultrafast laser modified fused silica is to our knowledge yet unknown, and therefore, it would require an additional measurement.

Based on these considerations, we therefore favor the mechanical resonance characterization methods for measuring the Young's modulus at various temperatures.

2.3.2 Survey of thermal expansion characterization techniques

The main standardized thermal-expansion measurement techniques can be divided in two categories: mechanical dilatometry and optical methods [136, 137].

In mechanical dilatometry, the specimen is placed in a furnace and brought in contact with rods (so called 'push-rods') made of fused silica. The rods displacement, induced by the specimen's thermal expansion, is monitored outside the furnace. According to the ASTM standard E228 17, this technique is used for materials having a CTE above 0.5×10^{-6} °C^{-1} for a 1000°C range [138] and for specimen lengths ranging from 20 to 60 mm and a diameter-width from 5 to 10 mm, respectively. Although this method does not seem suitable a priori for ultra-low CTE materials, it has also been used for small temperature ranges, for instance by Scott. Using this method, materials such as Zerodur® have been measured in the temperature range from -50 to 50 °C and with an accuracy of 3×10^{-9} °C^{-1} [139].

Optical methods are recommended for materials with CTE values lower than 5×10^{-6} °C^{-1}, and for a temperature range from -150 °C to 700 °C (ASTM E289-17 [140]). A large variety of optical-based methods exist for measuring temperature-length differences, among which, interferometric techniques have shown a significant higher accuracy over other optical methods.

Fabry-Pérot cavities, Fizeau and polarization interferometers are some examples of techniques used. An impression of a typical Fabry-Pérot-CTE measurement setup is given Figure 2.6a (adapted from [141]). The figure depicts a schematic of a thermal chamber, with an optical window at the top. There, the interferometer is placed on a copper block; a magnified schematic is given in the lower-left of the figure. The specimen (S) is sandwiched between two optical flats (o.p.), where the top-one forms the output coupler of the cavity and the bottom-one is a perfect reflector. Using this method, an uncertainty on the CTE characterization of ± 2.54 x 10^{-7} °C^{-1} has been reported, for a 50 mm-long polycrystalline copper specimen with an average CTE of ~ 15 x 10^{-6} °C^{-1} . Polarization interferometers, e.g. a Michelson interferometer, are the most commonly used for these type of measurements [142, 143, 144, 145, 146, 147]. An example of such a setup (adapted from [144]) is given in Figure 2.6b. The test specimen (gauge block) is placed in a chamber, and the interferometer light enters from the top. In the same figure (top part), a schematic of a double-pass interferometer is depicted and shows two beam lines, one serving as reference, reflecting on the base plate, and the other one, acting as a probe, reflecting on the top of the test specimen. The intensity of the superimposed reference and probe-beam is measured by a photo-detector, in the top left of the figure. A beating frequency is generated as function of the path difference by shifting the wavelength of the two beams with respect to each other, using an acousto-optic modulators (AOM). Using the signal of the second photo-detector as a reference signal, a lock-in amplifier further suppresses the noise. With this setup, they were able to determine the CTE of 100 mm-long steel gauge blocks, with an uncertainty of ± 7 x 10^{-9} °C^{-1} and an average CTE of 9.8 x 10^{-6} °C^{-1}. In [148], a similar principle is used, although they use a four-quadrant-photodiode, instead of single photodiodes, to measure simultaneously the parasitic movements of the sample, i.e. tilts and bending. The Physikalisch-Technische Bundesanstalt (PTB) institute in Germany built an ultra-precise Twyman-Green interferometer [149] that measures the absolute length, by phase stepping and under cryogenic conditions. The uncertainty on the measurement for a 35 mm long single-crystal silicon specimen was reported to be ± 3 x 10^{-9} °C^{-1}, with an average CTE of 0.0802 x 10^{-6} °C^{-1} [150].

Beyond the standardized methods, various solutions adapted to small-scales specimens, such as thin films and nanowires have been proposed. Scanning joule expansion microscopy uses the atomic force microscope (AFM) to measure thermal length changes of an electrically conductive material, where the sample is heated by Joule's heating [151]. Other methods based on AFM principles using various heat transfer mechanisms are reviewed in [152]. MEMS based solutions have been explored too, such as measuring the dimensional changes with capacitive based on-chip sensor [153]. The characterization of thin films has been done by measuring the temperature-induced change of curvature of a bimorph structure. A thin film is deposited on a thick substrate, with known substrate material properties. A difference in thermochemical properties between the thin film and the substrate causes the bimorph to bend. It should be noted that this method is a coupled problem, meaning that the Young's modulus should be known to retrieve the values of the CTE [154]. In [155], they employed this method to measure the CTE of dielectrics and metals, where the substrate length is in the

a

b
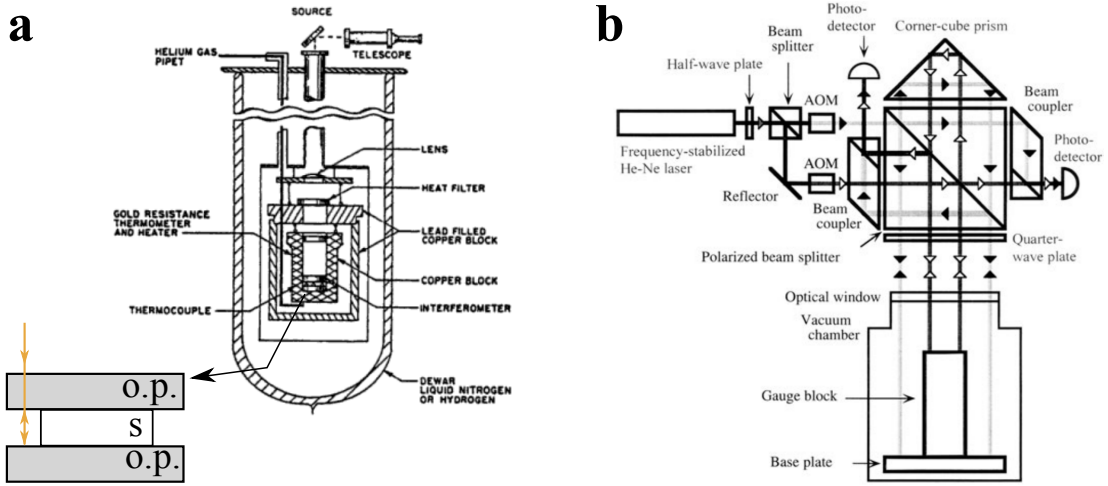
*Figure 2.6 – An impression of interferometric CTE characterization setups. **a**) A setup based on a Fabry-Pérot cavity [141], **b**) a double pass interferometer [144].*

order of 100 μm. They report an uncertainty in the range of 1 ppm/$^\circ$C. In parallel, the Young's modulus is retrieved by analysing the resonant frequencies of the same test structures. In [156], a method to discriminate between elastic properties and thermal expansion coefficient of the bimorph thin film was reported.

The interferometric dilatometer shows the highest accuracy in terms of CTE measurements and is a well established method. However, the volume of the characterized samples are significantly larger compared to the laser modified volume. For example, exposing a volume of 50 x 5 x 5 mm with a laser scanning speed of 8 mm/s, would require approximately a fabrication time of 75 days. Therefore, smaller exposure and micro-mechanical solutions are favored. Measuring principles which incorporate an AFM allow for measuring the CTE difference at a small scale. These methods are typically applied to test specimens with dimensions below the micrometer scale. These dimensions are around the fabrication resolution of the ultrafast laser technique. Based on this review, we chose to use the bimorph structure which allows us to study the thermomechanical problem in greater detail, as elucidated in the problem description. This structure enables us to measure both thermal expansion and the initial laser induced volume variation, which are essential for the determination of the CTE, as will be seen in the next chapter.

2.4 Conventions and composite material properties

Being anisotropic, the modified volumes are characterized in some cases in two directions. In this document, the notation is defined based on the exposure strategy and not with respect to a coordinate frame. To clarify this point, the conventions and further corresponding equations are explained in this section. In Figure 2.7a, a schematic is drawn of an ultrafast laser exposed material, which is a combination of laser affected zones (LAZ) and pristine material, the whole

is referred as the "average modified volume". The laser translates linearly, in this case along the x-axis, and the scanning direction is denoted with $\vec{v}_s$. The LAZs are the cylinders, with elliptical cross-section shown in red with the cylinder axis orientated along $\vec{v}_s$. The LAZs are arranged perpendicularly to $\vec{v}_s$ and are separated with a distance l_s, forming layers of average modified volume in the x y plane. Furthermore, these planes are stacked in z-direction (in Figure 2.7a two layers are stacked on top of each other). We consider that there is no spacing between the layers in the z-direction.

The material properties$(E, \alpha, \beta, \epsilon)$ are defined either along or perpendicular with respect to $\vec{v}_s$, which are denoted with the superscripts $\parallel$ and $\perp$, respectively, see Figure 2.7. The subscripts s and l indicate if the material properties are referring to the pristine substrate and the average modified volume or to the LAZ, respectively. Finally, the material properties of the average modified volume- a volume with exposed and unexposed regions- are indicated with a hat ($\sim$) on top of the notation, as illustrated in Figure 2.7 a and b.
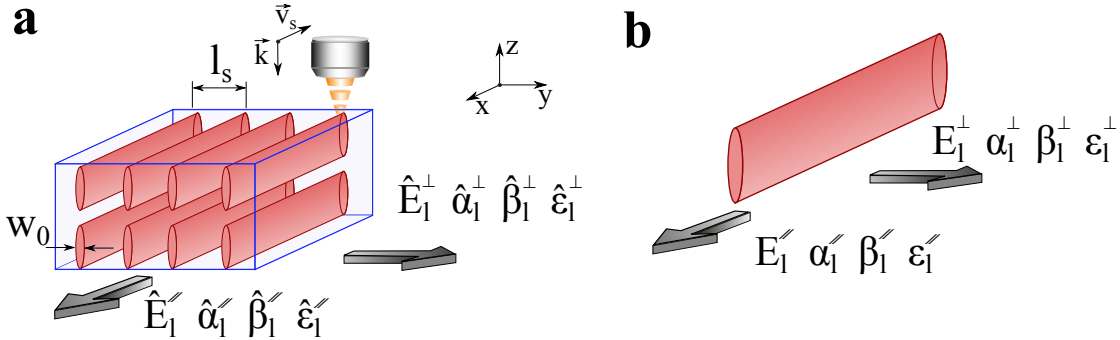
Figure 2.7 *– Definition of the material properties notations E, α, β and ϵ. **a**) depicts an average modified volume, which consists of laser affected zones (LAZ) and pristine material. The corresponding material properties are denoted with an hat ($\sim$). The notation for an individual LAZ are given. Properties are defined along and perpendicular $\vec{v}_s$, with the superscripts $\parallel$ and $\perp$, respectively. The LAZs are separated in the x-y plane with a spacing l_s. **b**) The LAZ and material properties definition.*

The average material properties are expressed in terms of the volume fractions V_l the LAZ volume fraction, and V_s the pristine substrates volume fraction. The analytical expressions of the average material properties are given in equations 2.5-2.12. Equations 2.5, 2.6, 2.9 and 2.10 are adapted from [157, 158], and equations 2.7 and 2.11 are derived from equations 2.5 and 2.9 (the thermal derivatives of $\hat{E}_l^\perp$ and $\hat{E}_l^\parallel$).

$$\hat{E}_l^{\perp} = \frac{E_l^{\perp} E_s}{E_l^{\perp} V_s^{\perp} + E_s V_l^{\perp}} \tag{2.5}$$

$$\hat{\alpha}_l^{\perp} = \alpha_l^{\perp} V_l^{\perp} + \alpha_s V_s^{\perp} \tag{2.6}$$

$$\hat{\beta}_l^{\perp} = \frac{\beta_s V_s^{\perp} E_{l,0}^{\perp} + \beta_l^{\perp} V_l^{\perp} E_{s,0}}{V_s^{\perp} E_{l,0}^{\perp} + V_l^{\perp} E_{s,0}} \tag{2.7}$$

$$\hat{\epsilon}_l^{\perp} = \epsilon_l^{\perp} V_l^{\perp} + \epsilon_s^{\perp} V_s^{\perp} \tag{2.8}$$

$$\hat{E}_l^{/\!/} = E_l^{/\!/} V_l^{/\!/} + E_s V_s^{/\!/} \tag{2.9}$$

$$\hat{\alpha}_l^{/\!/} = \frac{\alpha_l^{/\!/} E_l^{/\!/} V_l^{/\!/} + \alpha_s^{/\!/} E_s V_s^{/\!/}}{E_l^{/\!/} V_l^{/\!/} + E_s V_s^{/\!/}} \tag{2.10}$$

$$\hat{\beta}_l^{/\!/} = \frac{E_{l,0}^{/\!/} \beta_l^{/\!/} V_l^{/\!/} + E_{s,0} \beta_s^{/\!/} V_s^{/\!/}}{E_{l,0}^{/\!/} V_l^{/\!/} + E_{s,0} V_s^{/\!/}} \tag{2.11}$$

$$\hat{\epsilon}_l^{/\!/} = \epsilon_l^{/\!/} \tag{2.12}$$

3 Measurement principles[1]

The previous chapter discussed the coupled problem of controlling the macroscopic thermal expansion of a composite-like material created through laser-exposure, as summarized in equation 2.4. The macroscopic thermal expansion depends not only on the CTE, but also on the elastic properties of the different phases. Finally, the temperature-dependent elastic properties are of importance as the laser-exposed material undergoes a volume change and induces an initial strain. Therefore, to achieve our objectives of controlling macroscopic properties, the following material properties need to be characterized; i) the CTE, ii) the volume variation, iii) the Young's modulus and iiii) the temperature dependance of the Young's modulus.

To characterize these properties, we have used two methods;

1. by measuring the deflection of a *bimorph structure* over a given temperature range.

2. by measuring the initial and thermal frequency shift of a *mechanical resonator* after laser exposure.

With the bimorph experiment, we intend to characterize the CTE (i) and the volume expansion (ii), and with the resonance-based method, the Young's modulus (iii, iiii).

3.1 Bimorph

3.1.1 Measurement strategy

As we have seen before, fused silica exhibits one of the lowest CTE among commercially available materials ($\sim$0.6$\cdot$10^{-6} K^{-1}), only surpassed by a few others - such as Zerodur® and Sitall. This already low-CTE for the bulk substrate material makes thermal expansion measurement of laser-induced modifications difficult to perform due to the very small amplitude

---

[1]Part of this chapter has been published in [159] and [160]

of the effects. To overcome this problem, we use a method based on a cantilever amplifying mechanism illustrated in Figure 3.1. The cantilever is locally exposed just below its top surface [67, 90], such that exposed and unexposed regions form an equivalent bimorph structure made of two materials, with different CTEs, stacked one on top of another. The laser-exposed layer consists of an ensemble of discrete lines, forming a plane parallel to the cantilever top-surface (Figure 3.1 B-B). Just like a thermal bimorph, a difference of thermal expansion coefficient between pristine and laser affected zones will cause the structure to bend upon temperature changes, upward or downward, depending on the sign of the difference between the two CTEs. The cantilever's tip displacement (δ) results from an amplification effect due to the strain introduced inside laser affected zones (LAZ). The relation between δ, exposed length, and radius of curvature is given in Equation 3.1.

$$\delta(T) = \frac{L_l(L_c - L_l/2)}{r_T} \tag{3.1}$$

Here, L_l denotes the cross-sectional length of the LAZ, L_c the length of the cantilever, and r_T is the temperature dependent radius of curvature as shown in Figure 3.1. In our model, we are representing cross-sections of laser affected lines by plain ellipsoids that define our 'Representative Volume Elements' (RVE). Laser affected zones may have finer structures - in particular for the so-called 'nanogratings regime' in which one can find nanoplanes, themselves consisting of nanoporous material. However, for this particular problem, and as we will see later on, the level of granularity for describing the laser affected volume is sufficient for describing the thermomechanical behavior of the different regimes at the scale we are considering.

Timoshenko [154] and others [161, 162, 163] formulated an analytical description of the thermal deflections of a bimorph/multilayer structure. However, these expressions are not sufficient to describe our problem, as in these models a non pre-stressed state as initial condition is assumed. In [67], it was shown that the modified regions shrink or expand when the exposure conditions correspond to Regime I and II, respectively. Consequently, these volume variations induce an initial bending, pre-stressing the cantilever, and causing a linear variation of the bending strain (ϵ_0) along the z-axis, see Figure 3.1. The magnitude of the strain induced during initial laser exposure depends, in particular on the Young's modulus of the bulk unexposed material. Since the Young's modulus is itself temperature-dependent ([131, 164]) the strain induced in the *pristine* material as a result of the laser-exposure of the top layer becomes also temperature-dependent (Note that C. J. Bell *et al.* [27], used this effect to compensate for the positive CTE of fused silica). Therefore, the bending of the cantilever resulting from a temperature variation contains two terms: one that is inherent to the pre-loading effect due to the laser exposure, and another one, that truly depends on the difference of CTE between laser-affected zones and pristine ones. This situation is depicted in Figure 3.2.
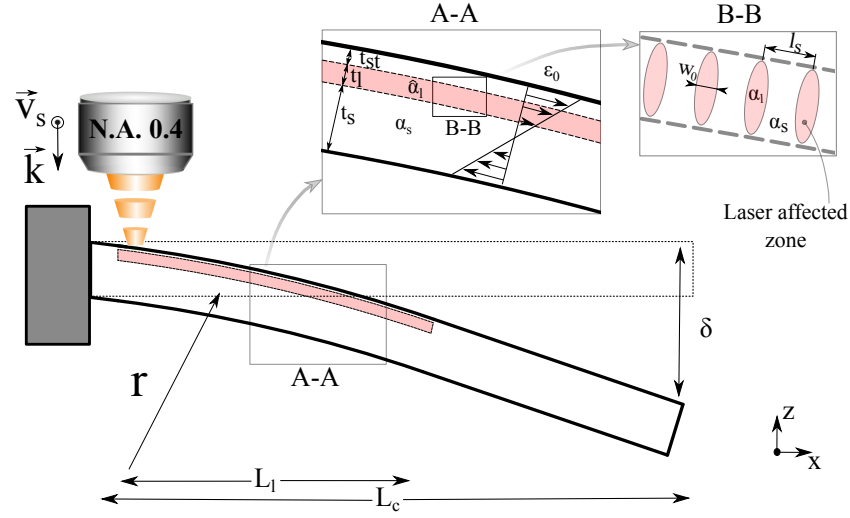
Figure 3.1 – *A schematic cross section of a cantilever where the near top layer is exposed to a femtosecond laser. The red zone represents the laser affected zones (LAZ). The cantilever bends with the radius r and δ is the amplified motion of the cantilever's tip. In the magnified image A-A is the initial strain (ϵ_0) depicted with the thicknesses of the different layers labeled. In the magnified image B-B are the individual written lines depicted as red ellipses. The line spacing, l_s, and modified width, w_0, are defined in the figure. Furthermore, the thicknesses of the different layers are denoted as t_{st}, t_l and t_s; the length of the cantilever L_c, and the modified zone length L_l. Finally, α_s, α_l and $\hat{\alpha}_l$ are the coefficients of thermal expansion of the pristine material, the modified material and of the modified layer (which is a composition of laser affected and unaffected material), respectively.*

3.1.2 Pre-strained multilayer mathematical model

To estimate the preponderance of these two effects, a mathematical model is derived based on a method inspired from [165], in which a closed form solution for multilayer systems is described. In summary, in this model we introduce an external moment that causes the initial bending radius. Furthermore, as a first approximation, we assume that the Young's modulus is linearly dependent on temperature [131], [164]. Using a Taylor expansion, we then separate the thermal bending into one term, $r_\alpha(T)$, that accounts for the difference in CTEs, and another one, $r_\beta(T)$, that accounts for the effect of the initial cantilever stress-loading. This separation is possible with the assumption that the deformation due to the exposure is much larger than the ones from the thermal expansion ($1/r_T << 1/r_0$). As we will see later on
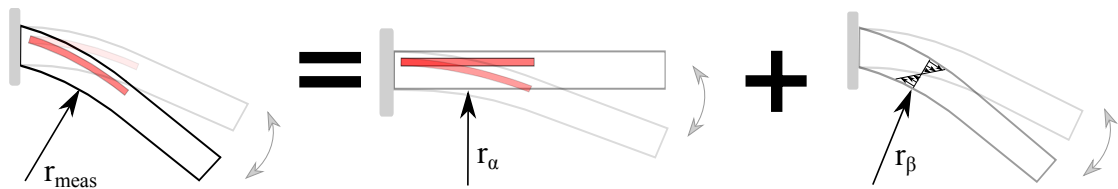
Figure 3.2 – *Schematic illustrating the superposition of two effects at the origin of the bending of the cantilever due to temperature variations: the thermal bending due to the CTE's difference and the thermal bending effect due to the initial strain in the material.*

in the chapter discussing the experimental results, this approximation is justified. Further simplifications are made by stating that the thickness of the laser affected zone is much smaller compared to the thickness of the unaffected one (i.e. $t_l << t_s$).

We define the strain of a three-layer cantilever as;

$$\epsilon(z) = c + \frac{z - t_b}{r} \qquad \text{for;} -t_s \leqslant z \leqslant t_l + t_{st} \tag{3.2}$$

Where c is the constant strain component, r is the bending radius due to thermal deflections. t_b is the distance between the bending axis and the bottom surface, and z is the position variable depicted in Figure 3.1, and is defined as zero at the interface between the bottom and exposed layers. The strain $\epsilon(z)$ is defined as the sum of the thicknesses of the different layers, t_s, t_l and t_{st}, which are defined in Figure 3.1. The stresses (σ_s, σ_l and σ_{st}) in the different layers are expressed by the set of Equations 3.3-3.5:

$$
\begin{aligned}
\sigma_s &= E_{s,T}(\epsilon - \alpha_s)\Delta T &\text{for;} -t_s \leqslant z \leqslant 0 &\tag{3.3}\\
\sigma_l &= \hat{E}_{l,T}(\epsilon - \hat{\alpha}_l)\Delta T &\text{for;} \, 0 \leqslant z \leqslant t_l &\tag{3.4}\\
\sigma_{st} &= E_{s,T}(\epsilon - \alpha_s)\Delta T &\text{for;} \, t_l \leqslant z \leqslant t_l + t_{st} &\tag{3.5}
\end{aligned}
$$

$E_.$ and $\alpha_.$ are the Young's modulus and thermal expansion coefficient, respectively. The first subscript $\cdot_l$ and $\cdot_s$ refer to the modified ("laser affected zone") and pristine volumes, respectively. The second subscript $\cdot_{,T}$, indicates that the material parameter is temperature-dependent. In this problem, we consider that the Young's modulus is temperature-dependent and is expressed using a first order linearized equation [131].

$$E_{s,T} = E_{s,0} + \frac{dE_{s,T}}{dT}\bigg|_{\Delta T=0} \Delta T \tag{3.6}$$

$$\hat{E}_{l,T} = E_{l,0} + \frac{d\hat{E}_{l,T}}{dT}\bigg|_{\Delta T=0} \Delta T \tag{3.7}$$

A solution for radius, r, can be found by solving the three following Equations: 3.8, the sum of forces due the uniform strain component should be zero; 3.9, the sum of forces due the bending strain should be zero; and 3.10, the sum of moments should be equal to an external moment. The external moment represents the moment induced by the initial volume expansion of the modified material.

$$E_{s,T}(c - \alpha_s \Delta T)t_s + \hat{E}_{l,T}(c - \hat{\alpha}_l \Delta T)t_l + E_{s,T}(c - \alpha_s \Delta T)t_l = 0 \tag{3.8}$$

$$\int_{-t_s}^{0} \frac{E_{s,T}(z-t_b)}{r} dz + \int_{0}^{t_l} \frac{\hat{E}_{l,T}(z-t_b)}{r} dz + \int_{t_l}^{t_l+t_{st}} \frac{E_{s,T}(z-t_b)}{r} dz = 0 \qquad (3.9)$$

$$\int_{-t_s}^{0} \sigma_s(z-t_b) dz + \int_{0}^{t_l} \sigma_l(z-t_b) dz + \int_{t_l}^{t_l+t_{st}} \sigma_{st}(z-t_b) dz = M \qquad (3.10)$$

In Equation 3.10, the moment M represents the moment that causes the initial bending induced by volume expansion of the LAZ. Substituting and rewriting the latter equation with respect to the bending radius gives:

$$\frac{1}{r} = \frac{3\left\{ E_{s,T}(c-\alpha_s)\left[t_s^2 - t_{st}(2t_l + t_{st}) \right] - \hat{E}_{l,T} t_l^2 (c-\hat{\alpha}_l) \right\} \Delta T + M}{E_{s,T}(C_1 + C_3) + \hat{E}_{l,T} C_2} \qquad (3.11)$$

With C_1, C_2 and C_3 as geometrical constants:

$$C_1 = t_s^2 (2t_s + 3t_b) \qquad (3.12)$$

$$C_2 = t_l^2 (2t_l - 3t_b) \qquad (3.13)$$

$$C_3 = t_{st}(6t_l^2 + 6t_l t_{st} + t_{st}^2 - 3t_b(2t_l + t_{st})) \qquad (3.14)$$

Linearizing equation 3.11 using Taylor expansion around $\Delta T=0$ gives:

$$\frac{1}{r_0} + \frac{1}{r_T} = \frac{M}{E_{s,0}(C_1 + C_3) + \hat{E}_{l,0} C_2} - \frac{\frac{dE_{s,T}}{dT}(C_1 + C_3) + \frac{d\hat{E}_{l,T}}{dT} C_2}{\left[E_{s,0}(C_1 + C_3) + \hat{E}_{l,0} C_2 \right]^2} M \Delta T \qquad (3.15)$$
$$+ \frac{3\left\{ E_{s,0}(c-\alpha_s)\left[t_s^2 - t_{st}(2t_l + t_{st}) \right] - \hat{E}_{l,0} t_l^2 (c-\hat{\alpha}_l) \right\}}{E_{s,0}(C_1 + C_3) + \hat{E}_{l,0} C_2} \Delta T$$

Where r_0 is the temperature invariant radius, and r_T is the temperature-dependent radius. Note, that the material constants are not dependent on temperature anymore. Using this linearized equation, we can express the moment M in terms of r_0 by setting $\Delta T=0$.

$$\frac{1}{r_0} = \frac{M}{E_{s,0}(C_1 + C_3) + \hat{E}_{l,0} C_2} \qquad (3.16)$$

Substituting M into equation 3.15 and subtracting the constant term gives the temperature

dependent radius r_T:

$$\frac{1}{r_T} = -\frac{\frac{dE_{s,T}}{dT}(C_1+C_3)+\frac{d\hat{E}_{l,T}}{dT}C_2}{E_{s,0}(C_1+C_3)+\hat{E}_{l,0}C_2}\frac{1}{r_0}\Delta T$$
$$+\frac{3\{E_{s,0}(c-\alpha_s)[t_s^2-t_{st}(2t_l+t_{st})]-\hat{E}_{l,0}t_l^2(c-\hat{\alpha}_l)\}}{E_{s,0}(C_1+C_3)+\hat{E}_{l,0}C_2}\Delta T \tag{3.17}$$

Considering the dimensions of the exposed cantilever, we can state that $C_1+C_3 \gg C_2$ so that Equation 3.17 becomes:

$$\frac{1}{r_T} = -\frac{dE_{s,T}}{dT}\frac{1}{E_{s,0}}\frac{1}{r_0}\Delta T$$
$$+\frac{3\{E_{s,0}(c-\alpha_s)[t_s^2-t_{st}(2t_l+t_{st})]-\hat{E}_{l,0}t_l^2(c-\hat{\alpha}_l)\}}{E_{s,0}(C_1+C_3)}\Delta T \tag{3.18}$$

The simplified analytical model for the measured cantilever bending caused by a temperature variation writes:

$$\frac{1}{r_T} = \frac{1}{r_\alpha}+\frac{1}{r_\beta}$$
$$= \left[6(\hat{\alpha}_{l,0}-\alpha_{s,0})\left(\frac{\hat{E}_{l,0}}{E_{s,0}}\right)\left(\frac{t_l}{t_s^2}\right)-\frac{1}{E_{s,0}}\left(\frac{dE_{s,T}}{dT}\right)\frac{1}{r_0}\right]\Delta T \tag{3.19}$$

In this equation, we found that the terms for thermal deflection due to the thermal expansion difference (r_α) and due to the pre-strained material one (r_β) which is directly related to the temperature-dependent Young's modulus. Due to the assumptions made, this linearized equation holds only for small deflections around the equilibrium position at $\Delta T = 0$, hence for $\frac{1}{r_T} \ll \frac{1}{r_0}$. We will see later that this assumption is justified.

3.2 Resonance

3.2.1 Measurement strategy

The resonance frequency of a mechanical structure depends on its mass and its stiffness ($f \sim \sqrt{k/m}$). Therefore, modifying the constitutive material of a vibrating structure by laser irradiation is expected to induce a noticeable frequency-shift of its resonance, as both, Young's modulus and mass distribution changes occur. Here, we use this principle to evaluate the local change of Young's modulus after laser exposure. Our resonating element consists of a free-end cantilever, shown in Figure 3.3 a), where the red colored zones illustrate the laser-modified volumes. Considering a maximum volume expansion of the exposed volume of 0.03% [90], we estimate that the frequency change due to mass redistribution is negligible. The lowest
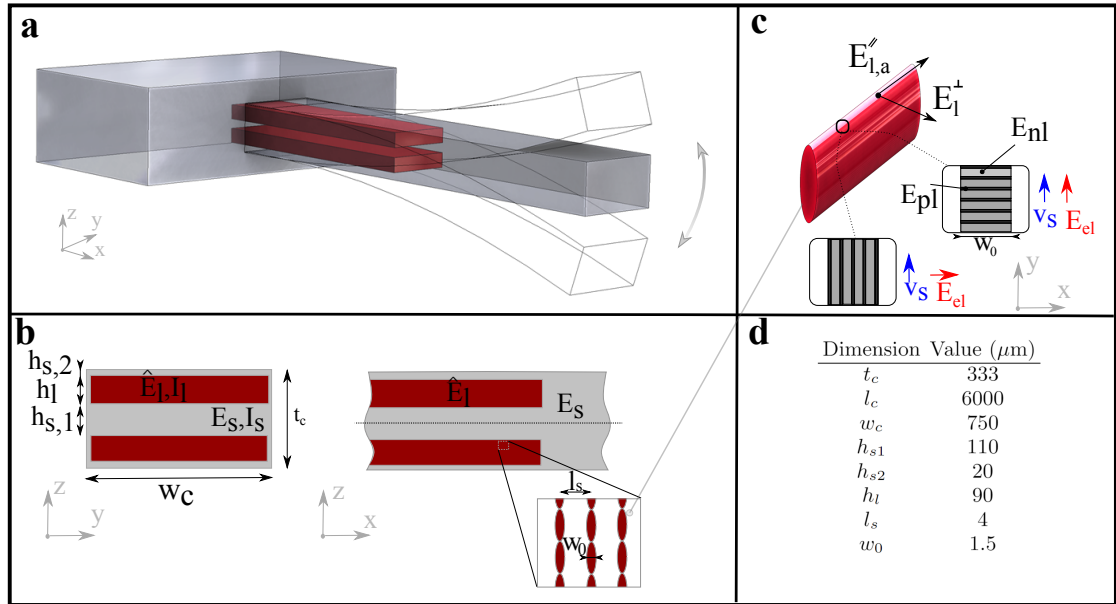
Figure 3.3 – a): *Schematic of the test-device: a cantilever (in gray) is locally exposed by the laser in its upper and lower volumes (shown in red).* ***b***): *Front and side cross-sectional views of the laser exposed volumes with the relevant dimensions indicated in the table, at the bottom left.* ***c***) *A laser affected zone (LAZ) with the transverse and axial Young's modulus indicated, $E_l^{\perp}$ and $E_l^{\parallel}$, and in the magnified views, the orientation of the nanogratings detailed for two polarization cases, $0°$ and $90°$ defined with respect to the writing direction.*

resonant frequency of a clamped-free cantilever is expressed in equation 3.20. ρ and V are the mass density and the volume of the cantilever. E. and I. are the Young's modulus and the second moment of inertia, respectively, with the subscripts $._l$ and $._s$ referring to the laser affected zones (LAZ) and the non-exposed ones, respectively. λ is the wavenumber, which corresponds to a resonance mode.

$$f = \frac{\lambda^2}{2\pi} \sqrt{\frac{\hat{E}_{l,T} I_{l,T} + E_{s,T} I_{s,T}}{\rho_T V_T l_T^3}} \tag{3.20}$$

with $\rho_T = \rho_0/(1 + \alpha \Delta T)$, $V_T = V_0(1 + \alpha \Delta T)$, $l_T = l_0(1 + \hat{\alpha}_l \Delta T)$, $I_{l,T} = I_{l,0}(1 + \hat{\alpha}_l \Delta T)^4$ and $I_{s,T} = I_{s,0}(1 + \alpha_s \Delta T)^4$, equation 3.21 becomes

$$f = \frac{\lambda^2}{2\pi} \sqrt{\frac{\hat{E}_{l,T} I_{l,0}(1 + \hat{\alpha}_l \Delta T) + E_{s,T} I_{s,0}(1 + \alpha_s \Delta T)}{\rho_0 V_0 l_0^3}} \tag{3.21}$$

The temperature-dependent elastic constants are linearized to the first order, i.e. $E_{s,T} = E_{s,0} + dE_{l,T}/dT\Delta T$. The thermal derivative of the frequency, evaluated at $\Delta T = 0$, is;

$$\left.\frac{\partial f}{\partial T}\right|_{\Delta T=0} = \frac{\lambda}{4\pi} \frac{1}{\sqrt{\hat{E}_{l,0} I_{l,0} + E_{s,0} I_{s,0}}} \frac{1}{\sqrt{l_0^3 \rho_0 V_0}} \left[I_{l,0}\left(\frac{d\hat{E}_{l,T}}{dT} + \hat{E}_{l,0}\hat{\alpha}_l\right) + I_{s,0}\left(\frac{d\hat{E}_{l,T}}{dT} + E_{s,0}\alpha_s\right) \right] \tag{3.22}$$

Simplifying further the equation, with the assumption that the terms containing the coefficient of thermal expansion ($\alpha_.$) are much smaller (by an order of magnitude ~ 4) than with the ones containing elastic constant thermal derivatives ($\partial E_./\partial T$), gives

$$\left.\frac{\partial f}{\partial T}\right|_{\Delta T=0} = \frac{f_0}{2} \frac{1}{\hat{E}_{l,0} I_{l,0} + E_{s,0} I_{s,0}} \left[I_{l,0}\left(\frac{d\hat{E}_{l,T}}{dT}\right) + I_{s,0}\left(\frac{dE_{s,T}}{dT}\right) \right] \tag{3.23}$$

rewriting the equation in terms of $\beta_.$, i.e. $dE_{l,T}/dT = E_{l,0}\beta_l$, gives,

$$\left.\frac{\partial f}{\partial T}\right|_{\Delta T=0} = \frac{f_0}{2} \left[\frac{I_{l,0}\hat{E}_{l,0}\hat{\beta}_l + I_{s,0}E_{s,0}\beta_s}{\hat{E}_{l,0} I_{l,0} + E_{s,0} I_{s,0}} \right] \tag{3.24}$$

$\hat{\beta}_l$ and $\hat{E}_{l,0}$ are the average properties of the modified volume, which are further specified in equations 2.5-2.12, in terms of l_s and w_0 (see Figure 3.3).

3.2.2 Fabrication

In previous work [90, 67], the bulk material of the cantilevers was modified in a post-exposure step, after the fabrication step that also involves a laser-exposed step. Consequently the free-clamped cantilever bends, due to the volume expansion. In our case, we apply a multilayer exposure, as illustrated in Figure 3.3, meaning that the second exposure layer is applied to a pre-stressed structure. Ultimately this leads to a position error of the subsequent layers (second, third and so on). Therefore, we chose to do the fabrication and modifying exposures in one step - to minimize the location error of the exposed volume inside the resonator - followed by the etching step, as depicted in Figure 3.4. Appropriate buffer zones are chosen between the modified zones and the contour of the cantilever, to prevent the laser-modified

volume under investigation from etching. The deposited energy is constant throughout the exposed volume, by irradiating the material at constant translation speeds.

1)   2)   3)
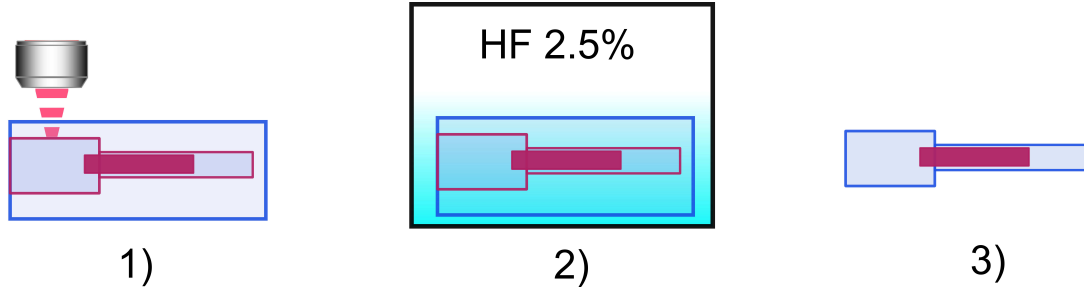
Figure 3.4 – *The schematic overview of the fabrication strategy: 1) The geometry of the resonator and the LAZ -subject of this study- is exposed in one step by the ultrafast laser. 2) The exposed sample is immersed in a low concentration hydrofluoric acid bath. 3) The resonator is released from the wafer.*

In this fabrication strategy, the stress will be released during the etching step, causing the structure –the resonator- to move with respect to the substrate. To prevent damage on critical parts throughout the exposed volume of the structure, sacrificial fixtures, forming anchoring points, are added to the least critical zones to absorb the high stress level. In Figure 3.5, a schematic is depicted of the resonator and fixtures located not near the exposure. Figures 3.5a and c show the microscope images of the detached fixtures, located at the base and tip of the resonator. Figure 3.5b depicts the cross-polarization microscope image, which reveals the induced tensile stress of a non-detached fixture. Finally, 3.5D-D depicts the side-view of the resonator, with the exposed volume, near the top and bottom surface, visible.
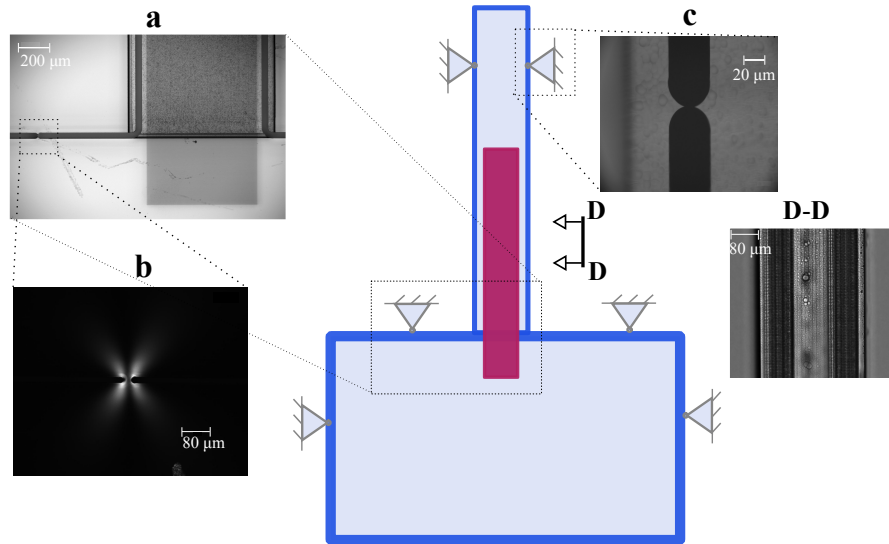
Figure 3.5 – *An illustration of the exposed resonator with the fixtures schematically depicted. a) A microscope image of an exposed cantilever near the anchor, b) a crossed-polarization image of a fixture under tension, c) the release of the fixture after sufficient etching time, D-D a side view of the cantilever with the exposed zones visible.*

An objective of this study is to characterize regime I and II modifications, typically created with

a pulse width shorter and longer than 200 fs [83], respectively. To study regime I modifications using this fabrication strategy, it is necessary to create regime I and II modifications during the same exposure step - where the regime II modifications serve as the HF sensitive material. In this work, the pulse width is controlled to create the two regimes. For this, we use the system *Satsuma* and an optical parametric amplifier (OPA) from the laser-manufacture Amplitude, which has a positively chirped - non-Fourier limited- output with a pulse width of 500 fs. A short, 50 fs, and Fourier-limited pulse is obtained after the compressor, with a set of prisms, as depicted in Figure 3.6. A motorized flip-mirror is added to this setup, in order to by-pass, and maintain, the long-pulse, or to compress the pulse. Note, that the resonators that contain regime II modifications were exposed using a single femtosecond laser, an Yb-doped fiber amplified system (from Amplitude Systémes, emitting 380 fs pulses at a wavelength of 1030 nm.
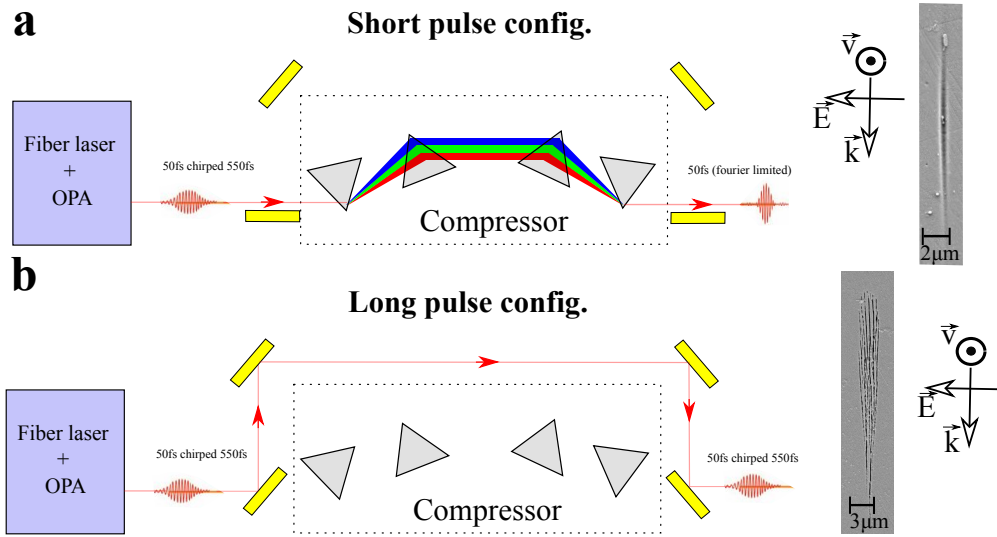
Figure 3.6 – *Schematics of the pulse width control. **a**) The positive chirped output, with a pulse width of 550 fs, of the OPA passes through the compressor, a set of prisms, and is compressed down to 50 fs. **b**) A schematic depicting the long pulse configuration, where a flipmirror is used to bypass the compressor and hence maintains the long pulse. SEM images are shown for laser exposed fused silica using the two pulse widths. It is observed that two types of modifications are generated; on top a homogeneous modification (Regime I) and below a nanograting modification (Regime II).*

4 Experimental setups [1]

4.1 Thermal chamber

To investigate temperature-dependent cantilever deflections, a stable and uniform temperature distribution across the specimen is needed, which is particularly challenging considering the low thermal conductivity of fused silica. To achieve this goal, a dedicated environmental chamber was realized. The low thermal conductivity precludes the use of conduction mechanism through the specimen to achieve a homogeneous temperature. Furthermore, to be able to probe optically the out of plane motion of the bimorph structure described in the previous chapter, an optical viewport is needed on top of the chamber. This window represents a thermal leak in our chamber, as it is not well isolated, which may create a temperature gradient in the volume where the specimen is placed. To overcome these two issues, we have chosen an approach based on gas convection to regulate the specimen temperature.
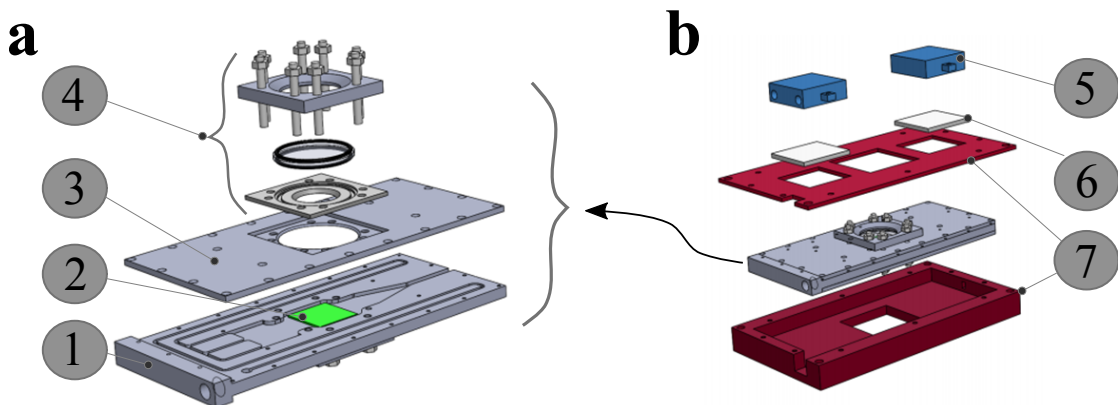
Figure 4.1 – *The exploded view of the thermal chamber in two parts.* ***a****) The base plate (1) containing the gas channels and the sample shown in green (2). On top of the base plate a cover plate (3) seals the chamber and the ensemble on top (4) forms the optical viewport.* ***b****) The isolating housing (dark red) (7), in white the thermoelectric devices (6) and in blue the cooling blocks (5).*

---

[1]Part of this chapter has been published in [159] and [160]

In practice, a preheated (or pre-cooled) inert gas (N_2) flows in a laminar regime across the chamber volume and thermalizes the specimen by convection. A close-loop control algorithm is used to keep the gas at the desired temperature and to apply heating or cooling ramps. Heating and cooling of the gas is done in elongated 1m-long serpentine channels made in an aluminum substrate cooled or heated up using thermoelectric devices. With this scheme, the measured thermal fluctuations throughout the chamber volume are in the range of ~10 mK.

In Figure 4.1 an exploded view of the complete environmental chamber is given. In Figure 4.1a, the aluminium base plate (1) is in the bottom, which contains the gas channels – done by CNC milling. An aluminum cover plate (3) and thermally conductive material seals the gas channels. The three components (4) on top form the viewport. Figure 4.1b, the aluminium core described before (1-4) is isolated by a thick housing made out of Bakelite (7) – a material with a low thermal conductivity and a reasonable machinability. The thermoelectric devices are shown in white (6), and covered by water-cooled blocks (5) to transfer the subtracted heat and the inherent Joules heating.

Finite element simulations were conducted to simulate the temperature distribution in the sample space to optimize the design. Figure 4.2a, the temperature distribution given for a flowing gas is shown and in Figure 4.2b a line graph depicts the temperature distribution in the sample space. In this FEM simulation, a set point temperature of 100°C (ΔT=75 °C) is used. As the gas passes through the sample space, and hence below the viewport, a decrease in temperature along the propagation direction of a maximum of 1 °C is observed. Increasing the flow velocity up to 5 mm/s decreases the spatial temperature difference below 0.02 °C.
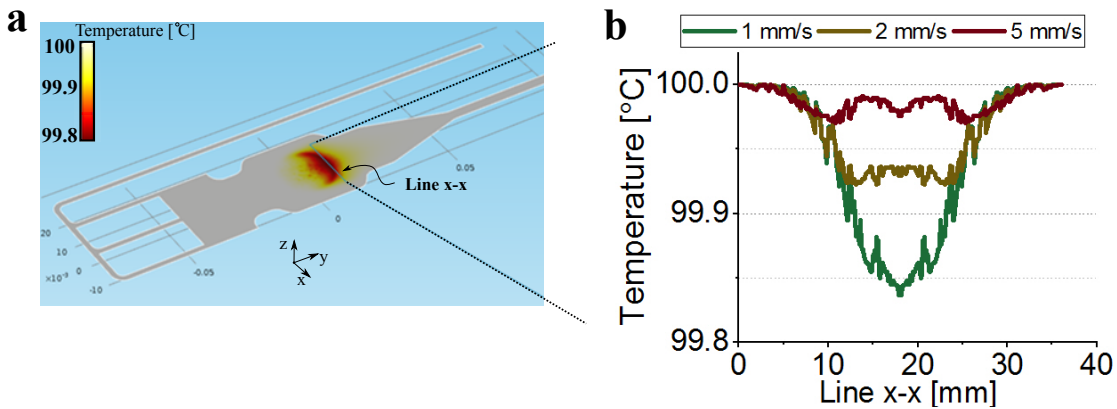
Figure 4.2 – a) *A thermal-flow FEM simulation with the temperature of the gas is shown.* **b)** *A graph depicting the temperature distribution in the sample space, for a set of flow rates.*

The temperature control is validated by measuring the gas temperature with a negative thermistor (NTC). Thermal fluctuations are measured over a period of 15 min for various setpoints ranging from -10 °C to 100 °C, shown in Figure 4.3. The PID controller temperature is tuned such that over the complete temperature range, the temperature fluctuations are minimized. With these PID parameters, a maximum fluctuation of 0.07 °C, at 95 °C, and a minimum of 0.0045 °C, at 15 °C are characterized. With the aid of a gain scheduling scheme, the perfor-

mance at the higher temperatures could be further improved.
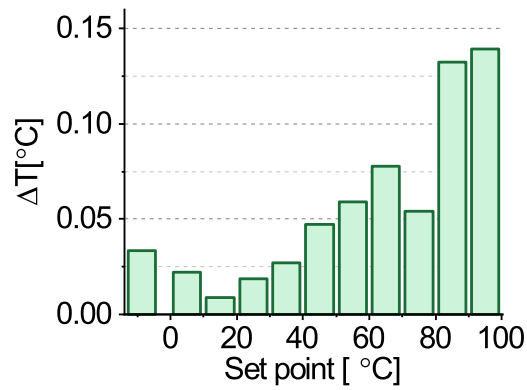
Figure 4.3 – *The thermal fluctuations are validated over temperature-set points ranging from -10 °C to 100 °C - measured with a negative thermistor.*
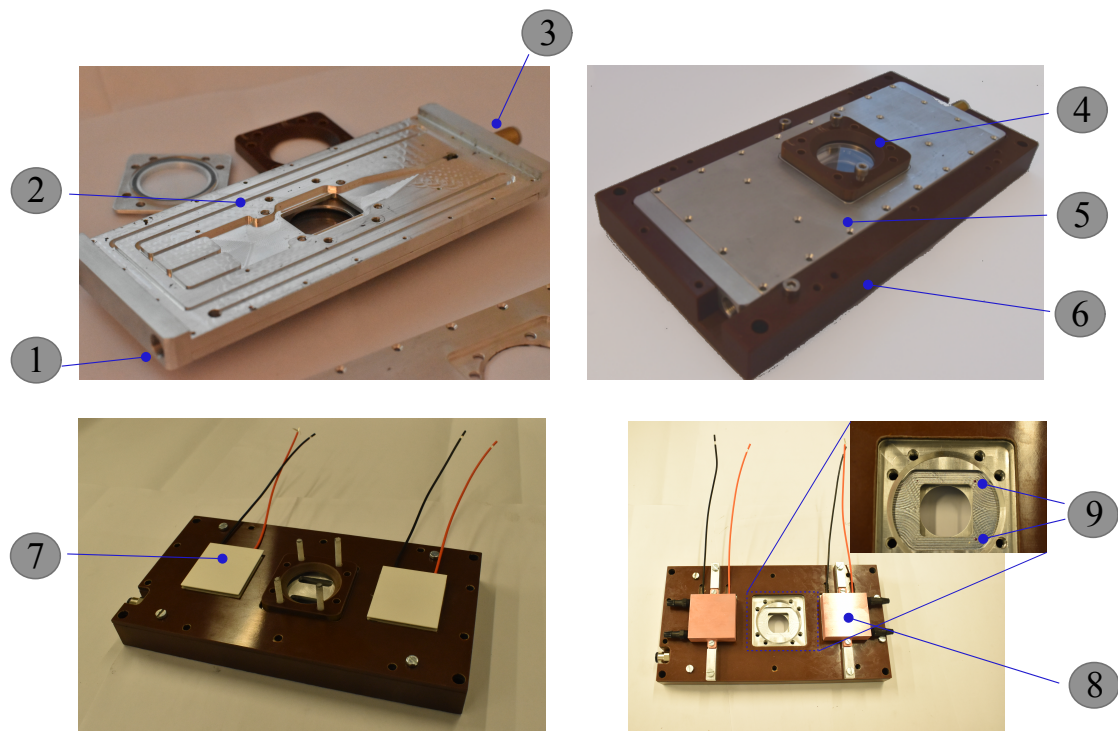
Figure 4.4 – *Pictures of the thermal chamber at different moments of the assembly process. 1) The gas inlet, 2) the gas channel, 3) the gas outlet, 4) the optical window assemble, 5) aluminium cover plate with gas-tight sealing, 6) thermal isolation, 7) thermoelectric peltier devices, 8) water-cooling blocks 9) kinetic specimen support (ruby spheres).*

4.2   Bimorph deflection measurements

A digital holographic microscope (DHM), from Lyncée Tec, is used to measure the cantilever out-of-plane deflections, with nanometric resolution. The temperature controller (that regulates the temperature in the chamber) and the DHM are synchronized, such that the recorded holograms are acquired at known-temperature points. A commercial software (Koala from Lyncée Tec) reconstructs an intensity and phase image from the recorded hologram, depicted in the top-right Figure 4.5, where the intensity image is used, in a post-processing step, to track parasitic motions of the sample in lateral directions that are inherently induced by the chambers thermal-expansion itself. The phase image is used to measure out-of-plane motions of the cantilever tip, relative to a reference taken on the specimen. With this, the metrological loop is minimized by measuring the thermal deflections relative to the specimen's base itself, minimizing errors caused by thermal expansion, force distortions and misalignments. To prevent further parasitic thermal stress, the specimen is placed on a kinematic mount supported by precision ruby spheres ensuring three well-defined contact points. With this strategy, the specimen can expand freely.
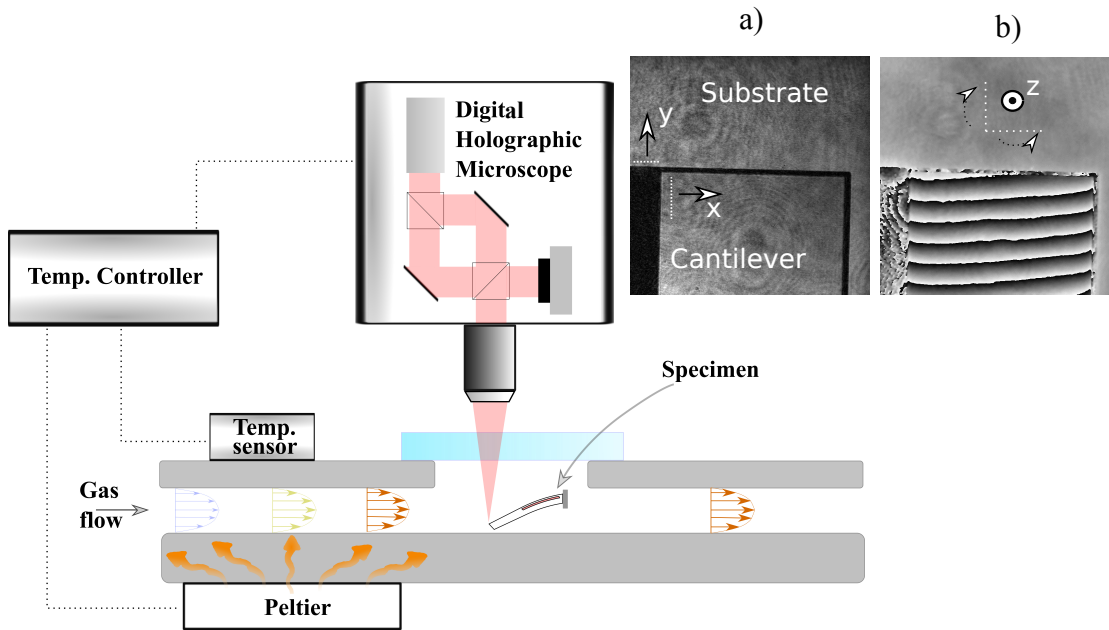
Figure 4.5 – *Schematic of the experimental setup for measuring cantilever deflections. The exposed cantilever is placed in a 'miniature' environmental chamber and thermalized thanks to a laminar flow of a pre-heated/pre-cooled inert gas (N_2). The deflection is measured using a digital holographic microscope (DHM) that measures the motion of the cantilever surface through a window. In the top right, the intensity (a) and phase image (b) acquired from the DHM are depicted. The parasitic motions of the substrate are recorded and the intensity image is used to track down the in-plane motion while the phase image measures the out-of-plane motion.*

To validate the performance of the experimental procedure, two types of calibration experiments are preformed; 1) a known step-height is measured as function of temperature, 2) the temperature induced motions of a bimorph structure, with known material constants,

is measured. For the calibration experiment, step-heights, of approximately 200 nm, are fabricated in a fused silica wafer using an etching mask method. A staircase temperature profile is applied, with temperature steps of 5 °C, out of which 20 data points from each temperature setpoint are collected. Figure 4.6a) depicts the measured error in the step height measurement, which is an average of the collected datapoints (the error bar represents the 95% confident interval). In the temperature range of interest, [10-40] °C, the uncertainty is +/- 8 nm. This value is considered in uncertainty calculations discussed in the next chapter. For the second calibration experiment, a bimorph structure is fabricated. In practice, a fused silica cantilever, realized using the ultrafast laser machining technology, is covered with a thin silver layer (556 nm) using a physical vaporized deposition (PVD) method. The measured and estimated motion, using the equations determined in the previous section, are shown in Figure 4.6. It demonstrates that the thermal behavior of such structures can be measured and estimated with a reasonable accuracy. However, no further conclusion on the measurement accuracy can be made, since the material parameters are known with a limited accuracy. In particular, the material properties of the deposited thin silver layer might differ significantly from the nominal bulk properties.
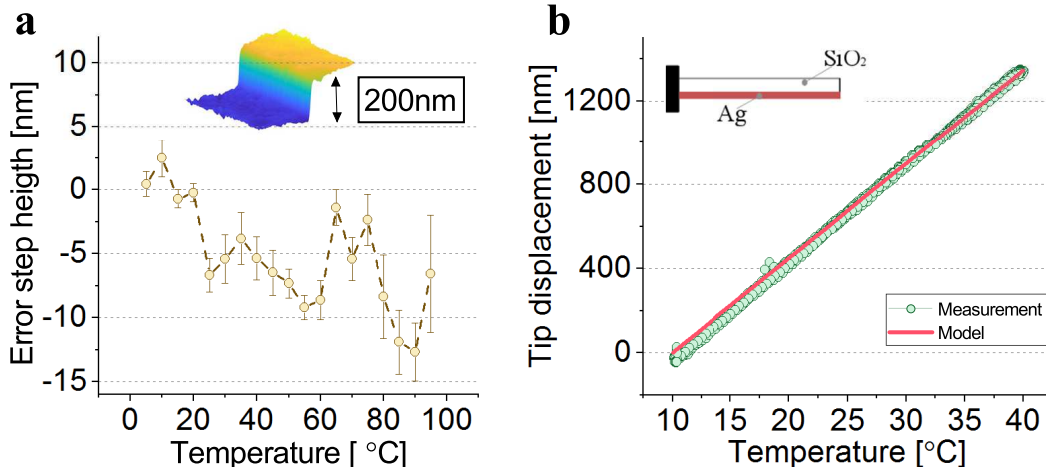
***Figure 4.6 – a)** Step height error measurement versus temperature. Data points are based on an average of 20 samples and error bars are defined as the 95% confident interval of this estimate. **b)** Measured and modeled deflections for a cantilever with a Ag coating deposited on it, as function of temperature.*

In the final part of this section, we discuss the measurement of a laser-exposed cantilever and the error of an inclined plane, induced by the parasitic lateral displacement of the specimen. As discussed in the previous section and illustrated in Figure 3.2, the laser-exposed cantilevers are initially bent due to the volume change of the LAZ. This situation, illustrated in Figure 4.7, causes a dependency between the parasitic lateral motions (i.e. along to the cantilever main axis) and the measured tip-displacement. An example of the temperature profile is shown in Figure 4.7; a periodic staircase temperature profile with steps of 5 °C from 10 °C to 40 °C is applied. The lateral parasitic motions, extracted from the intensity plot, are shown below; these movements have an amplitude of approximately 10 μm. In the figures further below, the tip displacement is depicted, where uncorrected and corrected data are given. The error

magnitude induced by the lateral parasitic motions, is dependent on the magnitude of the initial deflection.
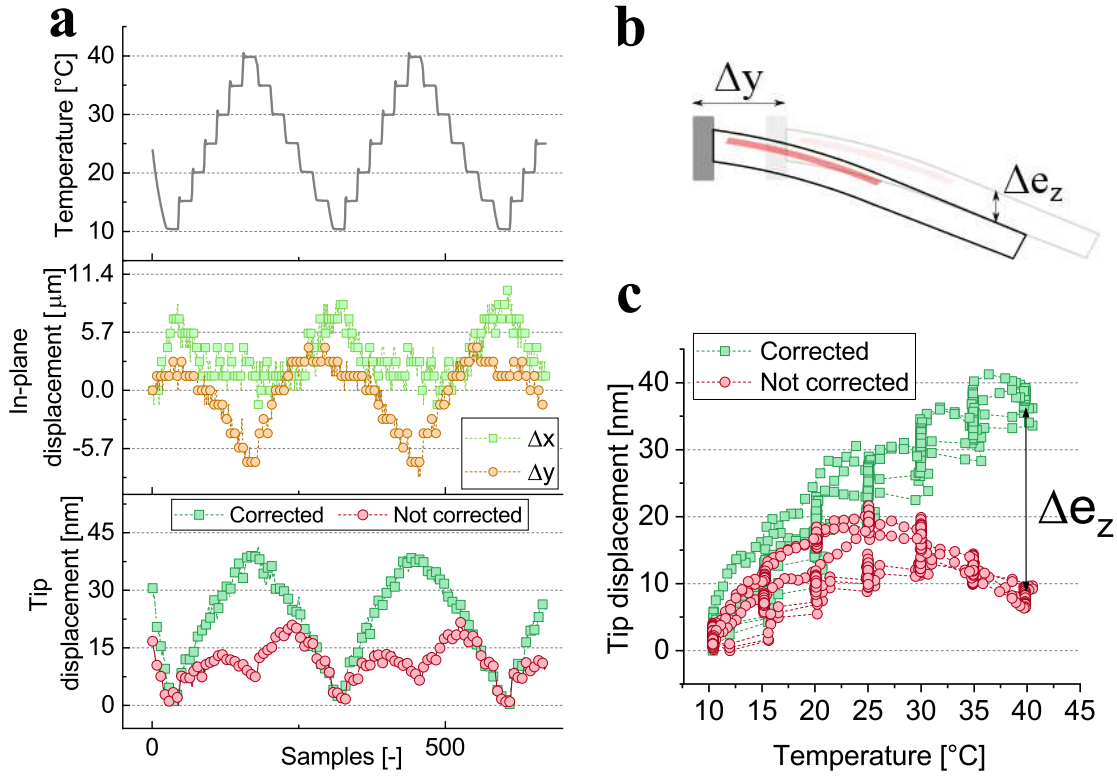
Figure 4.7 – a) Top: recorded temperature profile, middle: in-plane displacement and bottom: tip displacement as function of the recorded data points. Top graph: the steps size of the temperature profile is 5 °C spanning from of 10 °C to 40 °C. Middle graph: parasitic in-plane motions along the x- and y-directions, extracted from the intensity plot. Bottom graph: tip displacement, where ○ and □ are the non- and corrected data. **b)** An illustration of a bent bimorph structure and the definition of e_z. **c)** The corrected and not-corrected data as function of the temperature.

4.3 Frequency resonance measurements

A piezoelectric transducer excites the resonator, while a contactless displacement sensor (Keyence LKH022) measures the tip displacements. The resonant ensemble is placed in the environmental chamber discussed in the previous section. To track down and maintain the system at its resonance frequency, a phase-lock loop method is applied using a lock-in amplifier (L) (Stanford Research Systems SR850) and a proportional-integral (PI) controller, see Figure 4.8. The lock-in amplifier determines the phase delay ϕ between the input (S_i) and output signal (S_o). At ϕ =-90° the resonator is in resonance, as illustrated in the amplitude and phase diagram in Figure 4.8. The -90° phase delay is used as a reference point for a PI controller. The PI controller closes the loop by sending a new frequency to the signal generator (S). The frequency is recorded and further synchronised with the recorded temperature.

Examples of temperature-induced frequency shifts are depicted in Figure 4.9, for two resonators, R1 and R2, with a regime II exposure versus the reference resonator, R0. In this example, the thermal frequency shift decreases approximately by 5 Hz over a temperature range of 30°C. From the slope ($\partial f / \partial T$) measured on these graphs, we determine the material property $\Delta\beta$ ($1/E_0 \partial E/\partial T$), see equation 3.24, with respect to the β of the reference resonator.
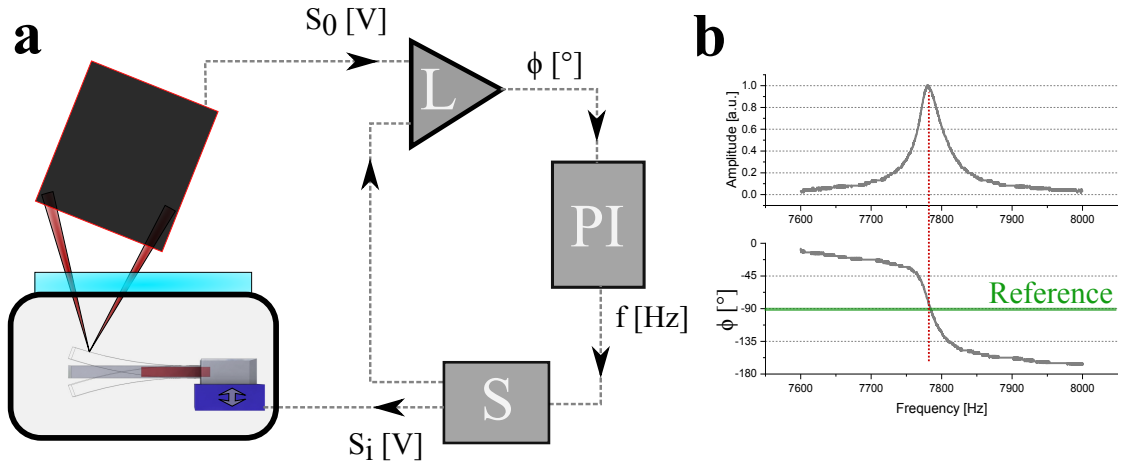
Figure 4.8 – a) *Schematic of the experimental setup for the frequency measurement. The resonator is placed in the environmental chamber that controls the temperature. The resonator is excited by a piezo, in dark blue, and the response is measured by a laser triangular displacement sensor. Furthermore, the resonator is kept at his resonance by a closed-loop arrangement. The phase (ϕ) between the input (S_i) and output signal (S_o) is determined by a lock-in amplifier (block L), the loop is closed by a PI controller (Block PI), and finally, an updated frequency (f) is send to a signal generator (Block S). The frequency f is stored for further analysis.* ***b***) *The amplitude and phase delay information of the lock-in amplifier are shown for frequencies around the resonance.*
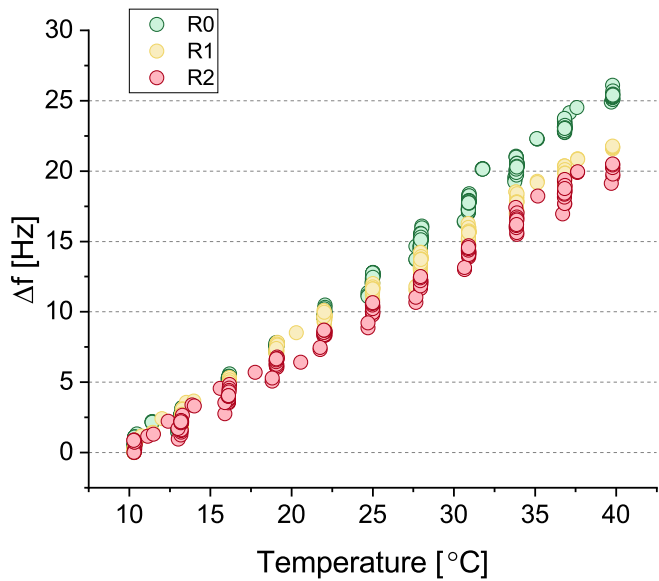
Figure 4.9 – *An example of measured frequency shifts versus temperature, for an unexposed (R0), and two exposed resonators (R1 and R2).*

Characterization of laser exposed Part II thermomechanical properties

5 Young's modulus [1]

The Young's modulus change is studied for the two different types of laser modified materials, Regime I and II. First, we present the results on the LAZ's Young's modulus of Regime I and second the results of Regime II. Furthermore, for Regime II we make an estimation of the local properties of nano-layers and conclude by proposing an interpretation about these local properties changes.

In these experiments, 1 mm-thick fused silica (Corning 7980 0F) substrates were used, each of them containing five resonators. On each substrate, one resonator is left unexposed and is used as a reference.

5.1   Regime I: "homogeneous modifications"

To generate a Regime I modification, a laser source (a combination of a fiber laser and a OPA from Amplitude) emitting at 850 nm and a pulse length of 50 fs, with repetition rate of 120 kHz is used. The method depicted in Figure 3.6 is applied for the fabrication of these resonators, which enables to generate Regime I and II modifications in one exposure step, by switching from a 50 fs to 550 fs pulse width. Furthermore, the modifications are generated with varying deposited energies, by changing the writing speeds, for fixed pulse energy, 250 nJ.
In Figure 6.1 the measured frequency shift is depicted as function of deposited energy and where the data point at 0 J/mm^2 deposited energy corresponds to the reference resonator. The frequency shifts are positive and rather small. Using equations 2.5 and 3.20, the Young's modulus is calculated and depicted on the right axis of Figure 6.1 - the error bar corresponds to the dimensional uncertainties. These values are in good agreement with Young's modulus measurement described in [166], who report a measured increase of 2 to 3 GPa, characterized by the nanoindentation technique. The increase in Young's modulus is expected as this modification is associated with a denser structure [67].

_____

[1]Part of this chapter has been published in [160]
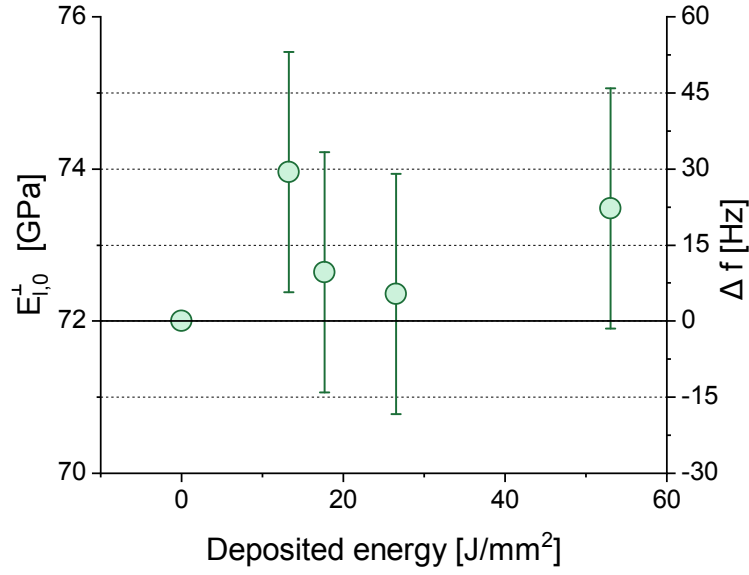
Figure 5.1 – *Measured frequency shifts and estimated $E_{l,0}^{\perp}$ as function of deposited energy, for a regime I modification. The exposure conditions are; pulse energy of 250 nJ, repetition rate of 120 kHz, pulse width of 50 fs, N.A. of 0.4 and a wavelength of 850 nm. The substrate contains high content of OH, ~1000 ppm.*

5.2   Regime II: "nanogratings"

Nanogratings have a complex structure consisting of nanoplanes parallel to one another. To be able to discriminate between the two Young's moduli of nanolayers defining the nanogratings, two sets of exposed cantilevers are used, with orthogonal polarization states. Using a composite expression for the effective Young's modulus of the entire LAZ, one can formulate two independent equations, out of which the actual values of the Young's modulus for the nanolayers can be extracted. In practice, two nanograting orientations, oriented along and perpendicular with respect to the cantilever principal axis, are selected for solving the system of equations. The deposited energy is changed by varying the translation speed from 1 to 10 mm/s, with a fixed pulse energy of 240 nJ and a repetition rate of 750 kHz. Finally, for these experiments the lines were written perpendicular to the cantilever, as depicted in Figure 3.3c. Figure 5.2 shows the measured frequency shift and the corresponding estimate of the Young's modulus for the transverse direction, using equation 3.20, for the two polarization cases, with respect to the reference resonator and as function of the deposited energy. For a zero-degree polarization, nanogratings are oriented transversally to the writing direction, a slight positive frequency shift is observed revealing a stiffer material than the pristine material. For a polarization of 90°, i.e. nanogratings orientated parallel to the writing direction, large negative values of the resonance frequency shift are observed. For this case, $E_{l,0}^{\perp}$ decays from 50 GPa to 35 GPa, going from lower to higher deposited energies. Athanasiou *et al.* [42] made an estimate, by indirect means of the transverse Young's modulus with similar exposure conditions - a polarization of 90°, pulse energy ~210 nJ and deposited energy ~20 J/mm². They

report a significant decrease of the elastic constant, with an estimated value of ~30 GPa. At this stage, it is not clear if the difference of about 10 GPa with our observation is due to the difference in exposure conditions or the measurement method. Nevertheless, both methods show a similar trend.
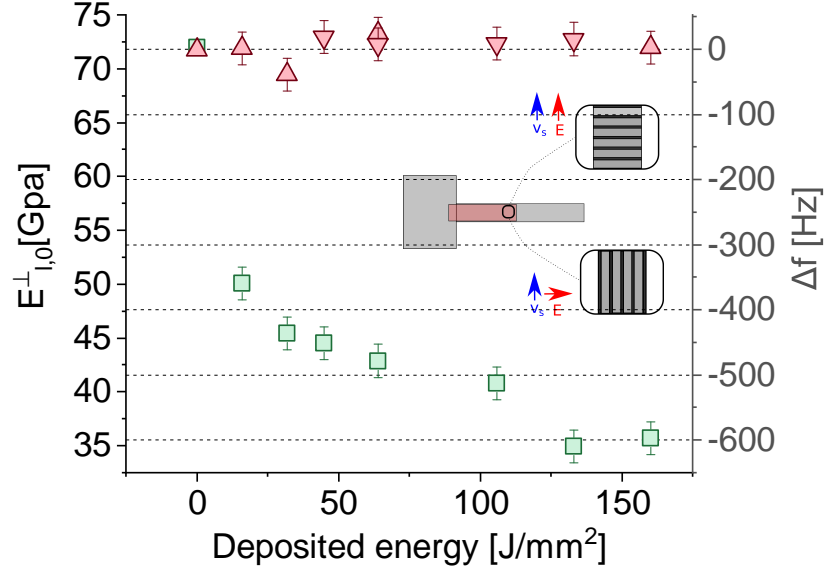
Figure 5.2 – *Measured frequency shifts and estimated $E_{l,0}^{\perp}$ as function of deposited energy, for two polarization cases. The triangles and squares represent the 0° and 90° polarizations respectively, for which the angles are defined relatively to the writing direction. Further exposure conditions are; pulse energy of 240 nJ, repetition rate of 750 kHz, pulse width of 300 fs, N.A. of 0.4 and a wavelength of 1030 nm.*

For polarizations aligned along and perpendicular to the writing direction, the nanogratings are parallel and serially arranged, respectively, with respect to the cantilever long axis. For the two nanolayer arrangements, we can express $E_{l,0}^{\perp}$ in terms of volume fractions and local Young's moduli. This is outlined in equations 5.1 and 5.2, where E_{pl} and E_{nl} are the Young's modulus of the porous layer and of the surrounding layer, respectively. V_{nl} and V_{pl} are the corresponding volume fractions. V_{pl} defines the ratio between the width of porous nanolayers and the spatial modulation period of nanolayers. Based on the observations from others [92, 60], we chose $V_{pl} = 0.1$. By definition, the volume fraction of the intermediate layers is expressed by $V_{nl} = 1 - V_{pl}$.

$$E_{l,0}^{\perp} = E_{nl}V_{nl} + E_{pl}V_{pl} \quad \text{for } 0° \text{ polarization} \tag{5.1}$$

$$E_{l,0}^{\perp} = \frac{E_{pl}E_{nl}}{E_{nl}V_{pl} + E_{pl}V_{nl}} \quad \text{for } 90° \text{ polarization} \tag{5.2}$$

The estimated values of the local elastic properties are depicted in Figure 5.3. It is found that the porous layers (E_{nl}) have values of Young's modulus   90% lower compared to the host material (SiO_2) and that the intermediate layers (E_{pl}) (in between porous layers) stiffen, eventually reaching a mean value of 80 GPa.
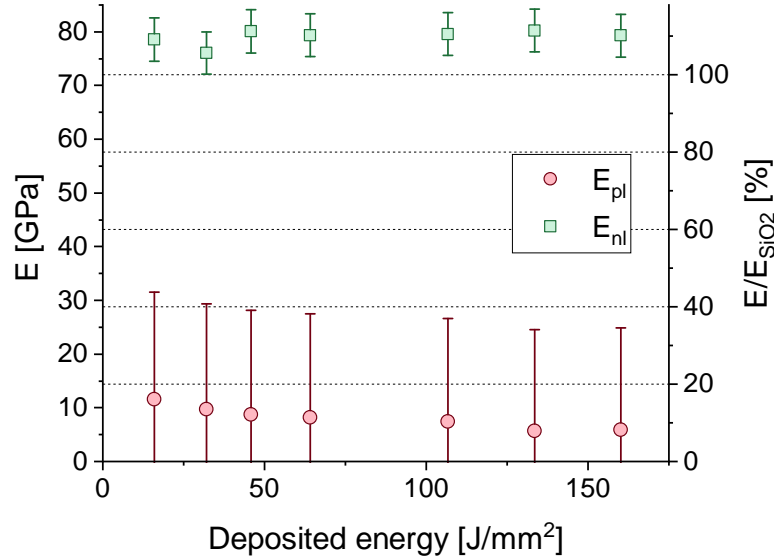
Figure 5.3 – *Estimated local properties of porous (E_{pl} - ∘) and non-porous layers (E_{nl} - □). The Young's modulus of the pristine material is 72 GPa.*

The decrease in Young's modulus for the porous layer can be understood as the lowering of the material density as the addition of pores effectively limits the number of interatomic bonds that can store elastic energy when being strained [167, 168]. The presence of free molecular oxygens, found by Raman and fluorescent spectroscopy [84, 67, 49], supports a decrease in the matrix connectivity. The increase of Young's moduli (E_{pl}) is an interesting observation and is to date, not directly supported by other types of experimental observations, due to the lack of a suitable technique having the resolution to effectively measure only the interstitial layer. Note that for a so-called 'Regime I, modification', a Young's modulus increase of about 2 to 3 GPa was measured using nanoindentation [166]. Here, the observed stiffening effect implies that this zone gets denser. Furthermore, a densification of these non-porous layers is also indirectly suggested in [88], where they estimate an increase of the refractive index of this layer by analyzing the strong form-birefringence induced by the nanogratings. The increase of the Young's modulus, refractive index, and possible densification, is like a Regime I modification [67, 36, 166] which exhibited similar characteristics. Previous works [84, 49] made similar observations. Lancry *et al.* [84] proposed a plasma density profile where, in the non-porous layers, the density meets the conditions for a Regime I modification, while in the position of the porous nanolayers, a decomposition threshold for SiO_2 molecules is exceeded. In this work, the measured values of the local Young's modulus increase and its corresponding

refractive index increase, measured in [60], from 2 x 10^{-2} to 5 x 10^{-2}, are significantly higher than the one found for the Regime I modification [169, 170], where an increase 10^{-4}-10^{-3} is reported. The mechanism, which have been accounted for the refractive index increase for laser irritated fused silica are i.e.: (i) compaction due to rapid cooling down from temperatures near and above the glass temperature -eventually resulting in higher fictive temperatures [171] (ii) increase of densification due to bond breaking and reorganization [172] (iii) color centers increase [173] (iiii) or simply, mechanical compression [133, 174]. The increase of either the Young's modulus or refractive index cannot only be accounted by densification due to thermal quenching, and consequently an increase of the fictive temperature, as it may for a Regime I modification. The studies about fictive temperature increase show a $\Delta E \approx 1.3$ GPa [175], and $\Delta n \approx 600$ x 10^{-6} [175, 176, 177] for a $T_f = 1600\,°C$, as no dramatically higher values can be expected as the fictive temperature is limited by the melting temperature. Furthermore, the authors in [49, 172] argue that this thermally-driven reorganization is too slow for these ultrashort time scales. As no increase of the Young's modulus is expected due to the formation of color centers, rather a decrease due to the lack of connectivity of the SiO_2 network, it is more likely that a mechanism based on the occurrence of fast compressive stress combined with thermal quenching is responsible for the high value increases, observed in our experiments. In hot-compression studies reported in [174], an external pressure is applied on heated samples assisting an accelerating micro-flow towards a denser structure. In combination with rapid cooling, high densification configurations are quenched and stabilized. While cold-compressed fused silica behaves elastically at pressures below 9 GPa [133], thermally-quenched compressed silica shows residual densification and an increase in Young's moduli, with significantly higher thermal stability [174]. A similar effect could occur here, considering the presence of hotspots within the porous layers [84], that pressurize the surrounding material -already at elevated temperatures- due to the intense localized plasma state. The pressure is maintained after the rapid cooling as free-oxygen molecules are not recombined with the glass matrix and remain trapped in a gas phase within the porous structure. To support our hypothesis, we note that pressures in the order of 2 GPa at elevated temperature are sufficient to reach the values we obtained for the Young's modulus and refractive index [178]. Note that in another work [179], the local stress in a single layer was indirectly predicted to reach about 2 GPa, which further supports the present observations. This is in essence contradicting the ideas that suggest that the formation of porous layers is not the driving force for compaction, but rather are cracks as a consequence of the neighboring densifying material [93, 49]. Additional evidence [79], based on scanning thermal microscopy, supports the fact that nanoporous layers are not cracks.

We like to extend this discussion towards a more general ongoing discussion. As briefly described above and broadly reviewed by i.e. P. F. McMillan [180], fused silica can undergo transformations towards different amorphous states, also coined by M. Grimsditch as 'amorphous polyamorphism' [181]. Roughly two amorphous states are recognized, the low (LDA) and high density amorphous state (HDA). However, unlike amorphous ice, fused silica possesses multiple unique sub-states in the LDA and HDA domains [135], which can be reached

depending on the thermal- and pressure-history. In the next chapter, examples are highlighted on the dependence of fused silica's properties to the pressure-temperature path. To thermodynamically formulate the state of a metastable material, such as glass, additional state variables needs to be defined. The fictive temperature is meant to be the third state variable, besides the state variables; temperature and pressure, to quantify the thermal history from equilibrium (liquid) to a metastable state (actual temperature) for thermodynamic calculations. However, it seems that the fictive temperature information is insufficient to describe metastable state changes due to different thermal histories, as differences in material properties are obtained for glasses with an equal fictive temperature [182]. Therefore P. K. Gupta introduced in addition another state variable, called the fictive pressure [183]. According to J.C. Mauro this approach seem not adequate enough to describe the state of the glass [184], nevertheless the quenching pressure and temperature seems both of importance. As mentioned in the previous paragraph, for the nanograting modification, we believe that additional internal pressures are needed to reach the state as we obtain in our estimation on the local properties.

Non-linear picture of the plasma density wave, adapted from M. Lancry et al. [5]
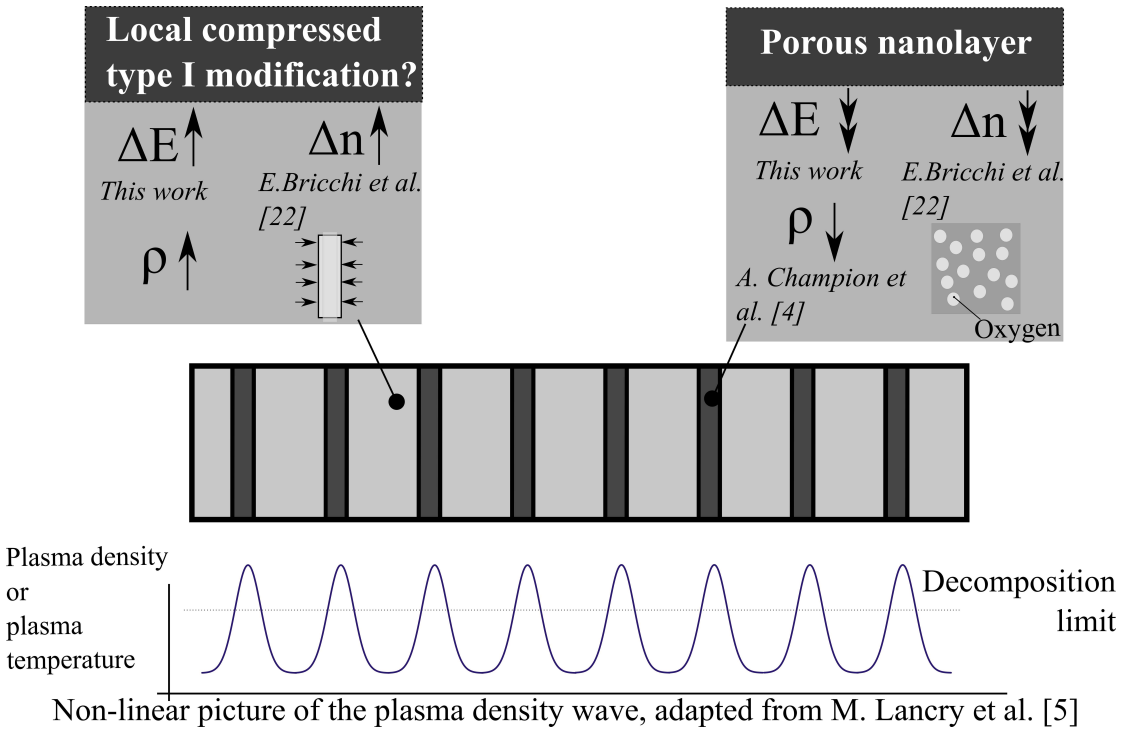
Figure 5.4 – *An illustrative summary of the discussion to explain our observations, with in the middle an illustration of the nanograting structure. Top-right: an illustration of the predicted material properties and chemical composition signature of a porous layer - the refractive index change estimated by [60], the oxygen filled pores [84] and elastic modulus estimated in this document. In the top-left, a refractive index increase [60] and the elastic modulus increase. Below the spatial distribution of plasma density, with peaks exceeding the decomposition limit, adapted from [84].*

5.3   Modeling of in-plane elastic properties

In the previous part, we derived the local material properties from experiments. In this section, we use these values to predict in-plane elastic properties as function of arbitrary nanograting orientations. Specifically, we test the validity of our model for two loading directions, axial and transverse. In practice, the LAZ is loaded along the cantilever's longitudinal axis, for instance a writing direction along the cantilever corresponds to an axial loading of LAZ as depicted in Figure 5.5. For these two writing directions, along and transverse, we vary the nanograting orientation by changing the laser beam polarization. Furthermore, the model is validated for two deposited energies, 20 and 64 J/mm^2, by varying the translation speed - the remaining exposure conditions are kept constant, repetition rate of 750 kHz and pulse energy of 240 nJ.

To model the in-plane transverse and longitudinal stiffness coefficients of a LAZ as function of the nanograting orientation (θ), we first establish the stiffness matrix of a projected portion of the nanogratings in the local coordinate frame (1-2), as illustrated in Figure 5.5. Secondly, to obtain the elastic properties in the global coordinate frame we introduce a rotation to the local coordinate frame with respect to the global coordinate frame (x-y). We treat the nanograting modification equivalently as a fiber-composite, and we assume that it is defining an orthotropic material [162]. The local coordinate frame 1-2 is defined such that the 1 and 2 direction are along and transverse to the nanogratings, respectively. The in-plane stress-strain relationship for an orthotropic material is expressed by the matrix form in equation 5.3. With $\underline{Q}_l$ as a symmetric 3x3 stiffness matrix, $Q_{l,11}$ and $Q_{l,22}$ are the stiffness elements along and transverse to the nanograting orientation, respectively, and $Q_{l,12}$ and $Q_{l,21}$, are the cross-coefficients. Finally, Q_{1212} is equal to the shear modulus ($G_{l,12}$).

$$\begin{bmatrix} \sigma_{11} \\ \sigma_{22} \\ \tau_{12} \end{bmatrix} = \underline{Q}_l \begin{bmatrix} \epsilon_{11} \\ \epsilon_{22} \\ \gamma_{12} \end{bmatrix} = \begin{bmatrix} Q_{l,11} & Q_{l,12} & 0 \\ Q_{l,21} & Q_{l,22} & 0 \\ 0 & 0 & Q_{l,1212} \end{bmatrix} \begin{bmatrix} \epsilon_{11} \\ \epsilon_{22} \\ \gamma_{12} \end{bmatrix} \tag{5.3}$$

$$= \frac{1}{1 - \nu_{l,12}\nu_{l,21}} \begin{bmatrix} E_{l,11} & E_{l,11}\nu_{21} & 0 \\ E_{l,22}\nu_{12} & E_{l,22} & 0 \\ 0 & 0 & G_{l,12}(1 - \nu_{l,12}\nu_{l,21}) \end{bmatrix} \begin{bmatrix} \epsilon_{11} \\ \epsilon_{22} \\ \gamma_{12} \end{bmatrix}$$

The elements of the matrix are expressed in terms of the material properties $E_{.}$, $\nu_{.}$ and $G_{l,12}$. Where $E_{l,11}$ and $E_{l,22}$ are the Young's modulus in the longitudinal and transverse directions. $\nu_{l,12}$ and $\nu_{l,21}$ are the Poisson's ratios and they can also be determined by the rule of mixtures, like for instance, for the longitudinal direction, $\nu_{l,12} = \nu_{nl}V_{nl} + \nu_{pl}V_{pl}$. For the Poisson's ratio in the transverse direction, we use the symmetry property of $\underline{Q}_l$ and rewrite the diagonal elements, as $-\nu_{21} = E_{l,11}/E_{l,22}\nu_{l,12}$. We can further detail the coefficients $E_{l,11}$ and $E_{l,22}$, as we did during the discrimination experiment, in terms of the experimentally retrieved Young's moduli of the local layers, as $E_{l,11} = E_{nl}V_{nl} + E_{pl}V_{pl}$ and $E_{l,22} = E_{nl}E_{pl}/E_{nl}V_{pl} + E_{pl}V_{nl}$. $G_{l,12}$ is also expressed in terms of the local shear modulus, G_{nl} and G_{pl}, and the volume fractions as $G_{l,12} = G_{nl}G_{pl}/G_{nl}V_{pl} + G_{pl}V_{nl}$. Assuming that the layers are isotropic, we can express

the local shear modulus in terms of the corresponding Young's modulus and Poisson's ratio, $G_{nl} = E_{nl}/2(1 + \nu_{nl})$ and $G_{pl} = E_{pl}/2(1 + \nu_{pl})$.
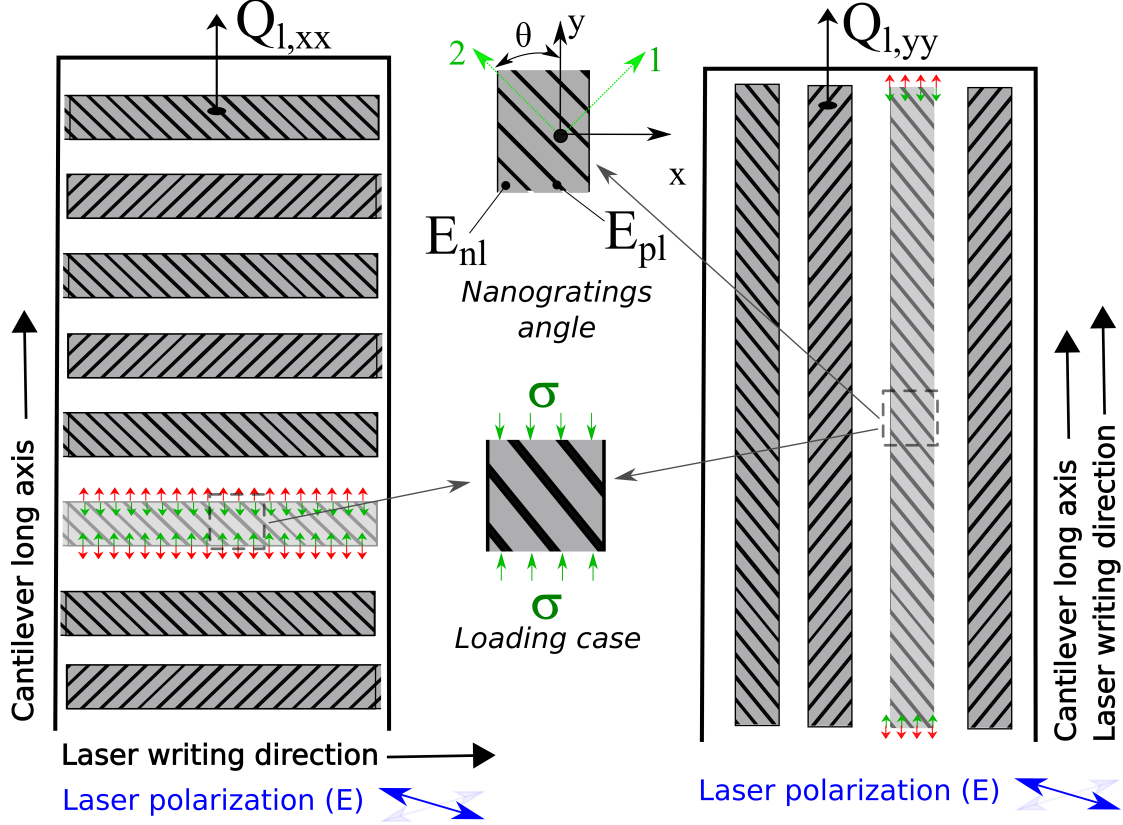
Figure 5.5 – *Schematic of the writing direction strategy, the definition of the nanograting orientation and definition of $Q_{l,xx}$ and $Q_{l,yy}$. On the left, the transverse laser-written lines and on the right, the longitudinal laser-written lines, with respect to the cantilever long axis. Furthermore, for both cases the nanogratings are mirrored with respect to the cantilever long axis for each subsequent line. In the middle, the magnified view illustrates nanogratings with a local coordinate frame (1-2) and the global coordinate frame (x-y) and below the loading direction (when the cantilever is set to vibration).*

At this stage, we have expressed in-plane elastic properties as a function of the local material properties. In the next step, we introduce a rotation operator, in order to model the nanograting orientation, by means of a coordinate transformation from the 1-2 (local) to x-y (global) coordinate frame, see equation 5.4.

$$\begin{bmatrix} \sigma_{xx} \\ \sigma_{yy} \\ \tau_{xy} \end{bmatrix} = \underline{R}_\sigma \underline{Q}_l \underline{R}_\sigma^T \begin{bmatrix} \epsilon_{xx} \\ \epsilon_{yy} \\ \gamma_{xy} \end{bmatrix} = \begin{bmatrix} Q_{l,xx} & Q_{l,xy} & Q_{l,xxy} \\ Q_{l,yx} & Q_{l,yy} & Q_{l,yxy} \\ Q_{l,xxy} & Q_{l,yxy} & Q_{l,xyxy} \end{bmatrix} \begin{bmatrix} \epsilon_{xx} \\ \epsilon_{yy} \\ \gamma_{xy} \end{bmatrix} \tag{5.4}$$

$$\text{with; } \underline{R}_\sigma = \begin{bmatrix} \cos^2\theta & \sin^2\theta & -2\cos\theta\sin\theta \\ \sin^2\theta & \cos^2\theta & 2\cos\theta\sin\theta \\ \cos\theta\sin\theta & -\cos\theta\sin\theta & \cos^2\theta - \sin^2\theta \end{bmatrix}$$

The elements $Q_{l,xx}$ and $Q_{l,yy}$ are of particular interest for us as these are the quantities we measure. These two terms are expressed in equations 5.5 and 5.6, and can be expressed as functions of the local Young's moduli, E_{nl} and E_{pl}, the nanograting orientation, θ, and the local Poisson's ratios, ν_{pl} and ν_{nl}. As the Poisson's ratio, are not known, we will evaluate $Q_{l,xx}$ and $Q_{l,yy}$ for a set of different values of ν_{pl} and ν_{nl} equal to the one of fused silica -ν_{SiO_2} =0.17.

$$Q_{l,xx} = Q_{l,11} \cos^4 \theta + \frac{1}{2} \left(Q_{l,12} + 2 Q_{l,1212} \right) \sin^2 2\theta + \sin^4 \theta Q_{l,22} \tag{5.5}$$

$$Q_{l,yy} = Q_{l,22} \cos^4 \theta + \frac{1}{2} \left(Q_{l,12} + 2 Q_{l,1212} \right) \sin^2 2\theta + \sin^4 \theta Q_{l,11} \tag{5.6}$$
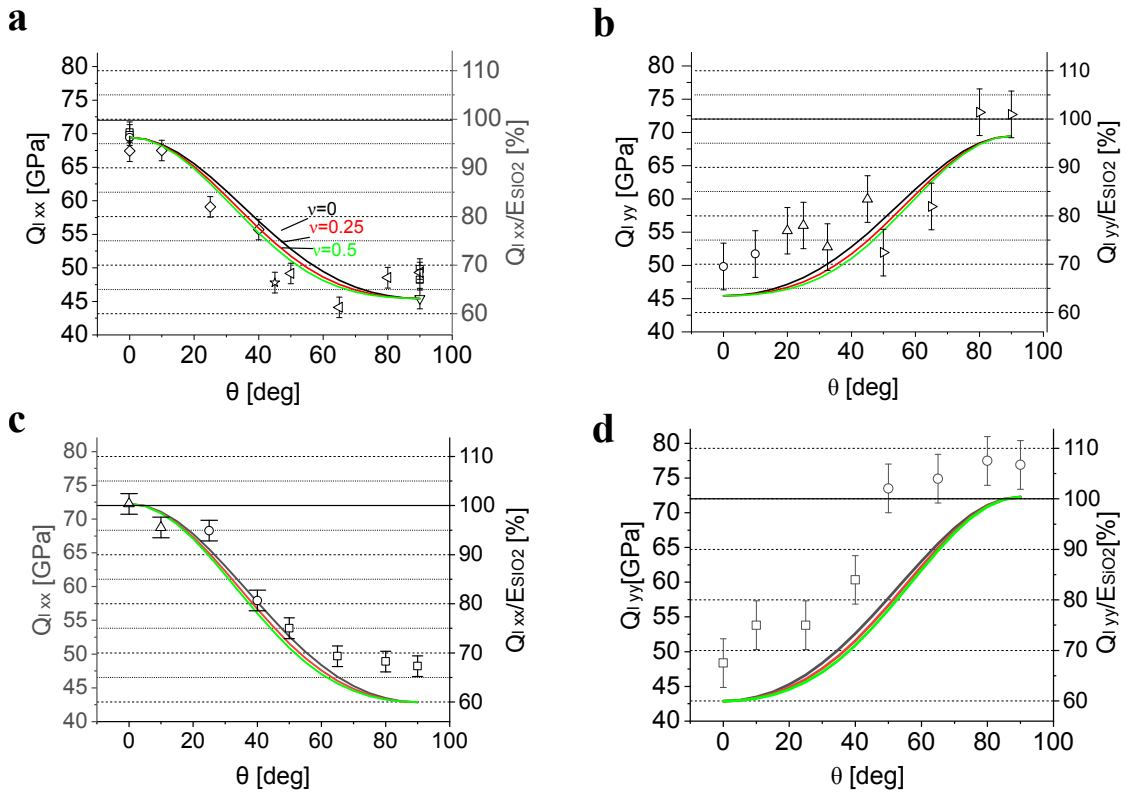
Figure 5.6 – *Estimation of the LAZ's Young's modulus, $Q_{l,xx}$ and $Q_{l,yy}$, as a function of nanograting orientations (θ) –defined with respect to the x-axis of the global coordinate frame- for a deposited energy of 20 J/mm^2, figure **a** and **b**, and 64 J/mm^2, figure **c** and **d**. The experimental estimation is illustrated by a set of markers that correspond to a given specimen measured. The result of the modeling is shown with solid lines for different Poisson's ratios (ν). The remaining exposure conditions are; pulse energy of 240 nJ, repetition rate of 750 kHz, pulse width of 300 fs, N.A. of 0.4 and a wavelength of 1030 nm.*

In one exposure, the lines are written along alternating positive and negative writing directions, as illustrated in Figure 5.5. The polarization for the writing directions is controlled such that the nanogratings are mirrored with respect to the axis along the cantilever, to avoid parasitic effects due to the expansion in the transverse direction of the cantilever. The estimations of the model and experiments for both loading directions are depicted in Figure

5.6, for deposited energies of 20 J/mm^2 (figures a and b), respectively, as a function of the nanograting orientation (θ) – defined with respect to the x-axis of the global coordinate frame. Figures a and b are corresponding to the transverse, $Q_{l,xx}$, and axial properties, $Q_{l,yy}$. The experimental estimations are illustrated by markers specific to a given measured specimen. The mathematical estimation is shown with a set of solid lines representing different Poisson's ratios (ν_{pl}). The experimental values follows the same trend as the model. For both deposited energies and considering $Q_{l,xx}$, the stiffness decreases steeply from 0° to 45° and saturates from 45° and 90°, as the model does. For the experimental estimation of $Q_{l,yy}$ a similar trend is observed, but mirrored. For the transversal direction and lower deposited energies, Figure 5.6a, the model is over-estimated for 0°<θ<90°. To explain this discrepancy, it is possible that the nanogratings are not well developed for theses polarizations and low deposited energies. Indeed, Zimmermann *et al.* [92] show that the nanogratings orientation other than parallel or perpendicular to the writing direction requires a higher pulse number to fully develop. Therefore, to validate this expectation we conducted the same experiment, but at a higher deposited energy, 64 J/mm^2 shown in Figures 5.6c and d. For both, axial and transverse directions, no dip is found, only an increase from lower to higher values. Indeed, it suggest that the dip in Figure 5.6a might be due to underdeveloped nanogratings for ranging orientations 0°<θ<90°.

For the case of axial properties and both deposited energies, the model under-estimates the experimental retrieved values, except for two data-points in Figure 5.6b. It seems that there exists a bias of nearly 5 Gpa between axial and transverse directions. It should be noticed that the model is constructed based on experimental values regarding a transverse loading. Shear-lag could be one possibility to explain the difference in results. The stress or strain transfers from inclusion to the host material, and vice versa, does not appear instantaneously [185], see Figure 5.7. The stress in the inclusion gradually develops, starting from the front- and back-end of the inclusion, and stabilizes towards the middle of the inclusion. Obtaining the transverse loading case, the discontinuing nature of this situation would not allow for efficient stress/strain transfer. The lag-length, l_{lag}, depends on the Young's modulus ratio between the host material and inclusion and the volume fraction - in our case V_l. For the volume fractions and stiffness ratios in our experiment, l_{lag} is small, below 1 μm, according to Cox's model for shear-lag [186, 187].

Another possible scenario, which may play a role, is that there is stress induced transversely to the loading direction, as there might be a difference in Poisson's ratios between pristine material and laser modified written lines [158]. In effect, more elastic energy is stored resulting in a higher effective Young's modulus. This effect would typically be noticeable in axial direction of a fiber type inclusion.

These effects described above are not captured in our model, which is based on simplistic mechanics. To improve the model, one could consider more sophisticated approaches. Models postulated by Eshelby take into account the shape of the inclusion [188]. Other composite modeling methods could also be applied in [189]. Nonetheless, these models seem particularly necessary when there exists a high contrast between material properties of the host material
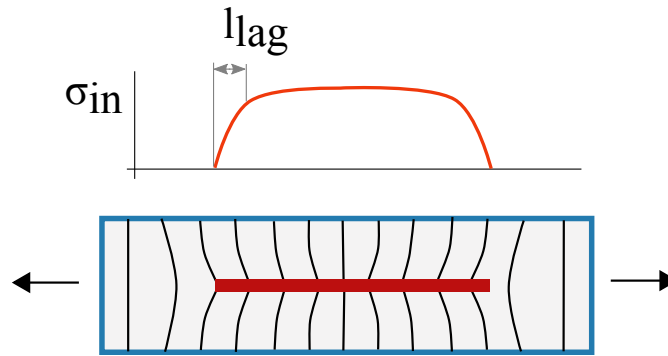
Figure 5.7 – *A two phase material being uniaxially loaded. The red area is the inclusion and in light gray volume the host material. The vertical lines represents the displacement field. σ_{in} is the stress in the inclusion, and with l_{lag} as the shear-lag length.*

and the inclusion. In our case, the contrast of Young's modulus between pristine material and laser affected volume seems to be low ($E_l/E_s \sim 1/2$). Although, at the nano-scale, the contrast between porous and non-porous layer, starts to be significant ($E_{pl}/E_{nl} \sim 1/10$).

5.4 Summary

The key results of this study are summarized below.

- A Young's modulus increase, 2-3 GPa, is measured for the homogeneous laser-induced modification (Regime I).

- The elastic properties of the nanograting modification (Regime II) are characterized to be anisotropic, for which the axis of anisotropy is dictated by the orientation of the nanograting.

- The local elastic properties of the nanograting modification, i.e. the porous and non-porous layers, are estimated, and for which the increase of non-porous layer's properties are estimated to be remarkably higher than found for a regime I modification. We speculate that the densification mechanism of this layer is based on the combination of internal pressures and rapid cooling from temperatures near the glass temperature.

- A mathematical model, which predicts the in-plane elastic properties as function of the nanograting orientation, is implemented and experimentally validated. The model seems to capture experimental observations reasonably well.

- However, for elastic properties in the axial direction, an appreciable discrepancy is observed between the model and experimental values. This observation suggests that more sophisticated modeling approaches should be implemented to capture the fine details of the stress-strain relation.

6 Temperature dependent Young's modulus

The temperature dependence of the Young's modulus of silica compared to other materials is uncommon. While the vast majority of materials see their modulus decreasing upon heating, fused silica displays an opposite behavior and gets stiffer when the temperature increases [132, 131]. Understanding this puzzling behavior remains a challenging topic, despite nearly a century of research [190] and recent work based on molecular simulations [191]. In this chapter, we explore how this temperature dependence evolves after localized exposure to the femtosecond laser.

For this specific study, the specimens described in the previous chapter are used. In practice, the effect of temperature on the resonant frequency of the beams is monitored over a temperature range from 10-40 °C. The changes are described with two metrics: the 'temperature coefficient of frequency' or 'TCF' that captures changes of the resonant frequency with a changing temperature, and the normalized Young's modulus change with temperature, or β_l. We further investigate for certain exposure conditions the role of OH-content in the glass composition on the change of β_l. Specifically, we compare low OH-content substrates (~1 ppm) (Heraeus,Suprasil 3002) with high-OH content glass (~1000 ppm) (Corning 7980). Furthermore, the Cl content of Suprasil 3002 is in the range of 1000 ppm – 3000 ppm and for the Corning 7980 substrates it is in the order of 100 ppm.

Furthermore, on each substrate, a reference resonator is added. Note that a mean value of TCF for all reference resonators is found around 109 ppm/°C. The error-bars in this chapter are regarding the measured TCF, and not to the estimated β_l. The main source of error for TCF is related to the clamping force of the resonator on its base. To support this observation, we have noticed that the deviation in TCF measurement is minimized when choosing thicker substrates/bases. For a 1 mm-thick substrate/resonator-base, the deviation is in the order of $+/- 3.6$ ppm/°C.

6.1 Results

We first will present our findings regarding regime I and II modifications as function of deposited energy, which are regarding the transverse properties ($\beta_l^\perp$). Figure 6.1 depicts the change in TCF and the estimated $\beta_l^\perp$ for resonators exposed with a pulse-width of 50 fs and pulse-energy of 250 nJ, creating a regime I modification. The TCF of the reference resonator is significantly higher compared to the mean TCF (109 ppm/°C). This discrepancy might be caused by the composition of the substrate itself. Overall, for the four exposed resonators, a lower TCF is measured compared with the reference resonator, (at 0 J/mm^2). An average TCF shift, over the complete deposited energy range, of -4.6 ppm/°C is found. The changes are too small to identify a clear trend as function of the fluence. The corresponding mean shift of $\beta_l^\perp$ is estimated to be -16 ppm/°C, using the composite equations in Chapter 2, equation 2.7, meaning that the positive temperature-elastic coefficient of the modified volume is reduced by 7%.
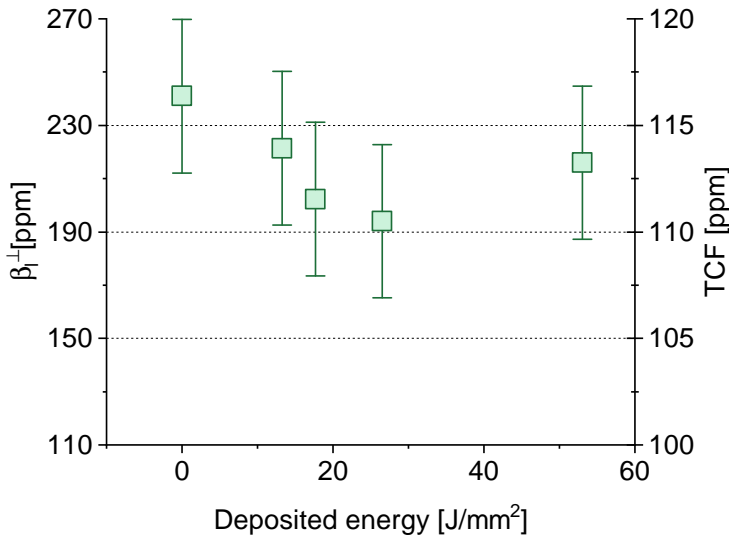
Figure 6.1 *– TCF and $\beta_l^\perp$ as function of the deposited energy, for a regime I modification. The mean reduction of the positive temperature-elastic coefficient is reduced by 7%. The exposure conditions are; pulse energy of 250 nJ, repetition rate of 120 kHz, pulse width of 50 fs, N.A. of 0.4 and wavelength of 850 nm. The substrate contains high content of OH, ~1000 ppm.*

Let us now discuss the change of $\beta_l^\perp$ regarding a Regime II modification, which is preformed for two nanograting orientations, along and perpendicular to the loading direction. In Figure 6.2a and b, results are presented which are regarding a substrate with an OH-content of 1000 ppm, Corning 7980, and in Figure 6.2c and d are the results regarding the low OH-content substrates, Suprasil 3002. As a reminder, the high OH-content substrate is the type used throughout this document.
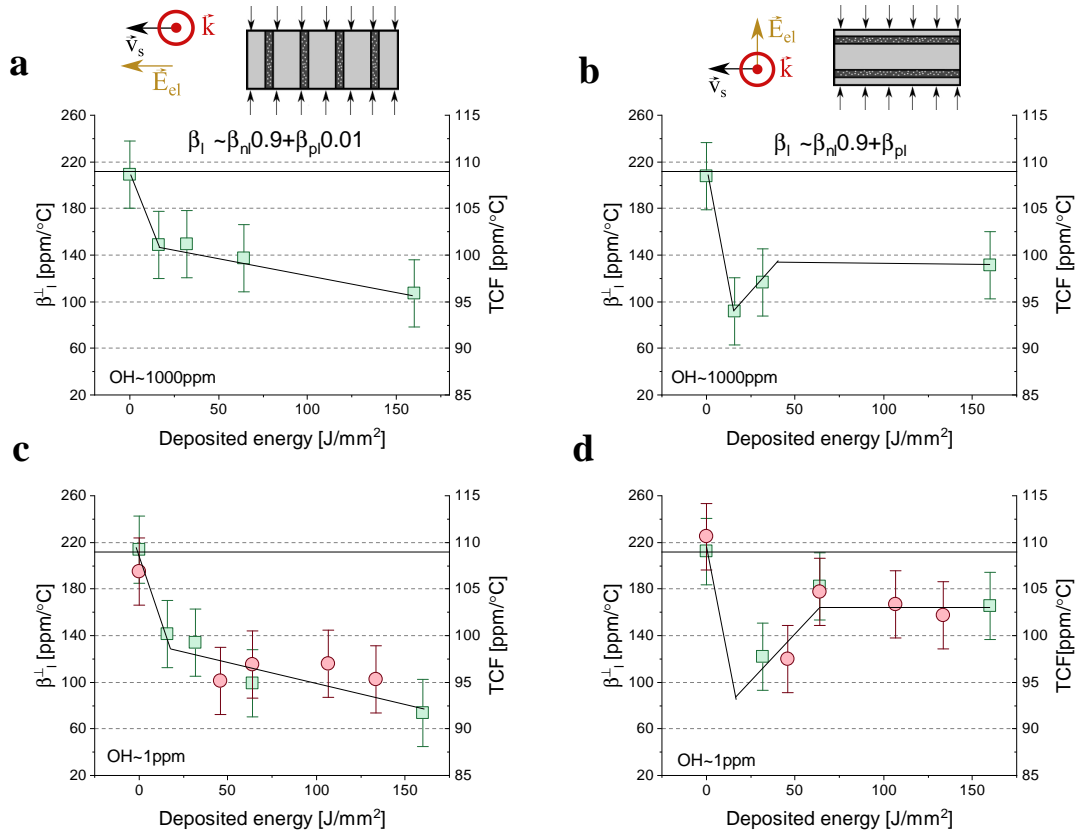
Figure 6.2 – *TCF and $\beta_l^\perp$ as function of the deposited energy, for a Regime II modification.* **a, b**) *are results regarding a high-content OH glass (Corning 7980) and* **c, d**) *are regarding to a low-content OH glass (Heraeus, Suprasil 3002). Where, the left figures (**a** and **c**) are regarding a polarization of 0° and the right figures (**b** and **d**) are regarding a polarization of 90°. On top, the orientations of the nanogratings with respect to the loading direction are illustrated. Furthermore, an estimation on the dependence of β_l versus the individual plane properties, β_{np} and β_{pp}. The markers in one figure make the distinction between substrates. The lines are drawn to guide the eye. $\beta_l^\perp$ reduces for all the cases, and at a certain deposited energy, down to approximately 50%. The exposure conditions are; pulse energy of 240 nJ, repetition rate of 750 kHz, pulse width of 300 fs, N.A. of 0.4 and a wavelength of 1030 nm.*

The first observation we want to highlight is that the reduction of $\beta_l^\perp$ is significantly larger than for a Regime I modification. For all cases, we find a reduction of up to approximately 50%, albeit at different deposited energies for the two nanograting orientations considered here. A second observation to highlight is the difference in behavior between the two nanograting orientations. For nanogratings aligned along the loading direction (figures a and c) $\beta_l^\perp$ gradually decays for an increasing deposited energy, while for the orthogonal case, (figures b and d), a rapid decay is observed, for the low deposited energies, reaching a minimum of 50%. Note that lines are drawn as visual guide but do not have a physical meaning. For the orthogonal direction, the reduction becomes smaller at higher deposited energies and saturates above 50 J/mm². It should be noticed that a similar behavior – a rapid increase towards a peak value, followed by a decay and saturation, is also observed for volume expansion

65

[90] and CTE measurements [159]. The rapid decay, in figure b and d, could be linked to the laser induced CTE increase, created in this regime [159], as an increased CTE would reduces TCF, see equation 3.23. However, based on the CTE values predicted in Chapter 7 and taking volume fractions into account, this is unlikely to be the case. The influence of the increased CTE would result in a ~1 ppm/°C reduction of the TCF. Furthermore, if the CTE would be dominant in this measurement, the TCF would be sensitive to the removal of point-defects, achieved with thermal annealing at 300 °C [159]. As we shall see later in Chapter 8, this does not occur in this temperature range. Notice that the athermal [1] volume expansion and CTE in other works [90, 159], also reported a similar behavior for nanograting orientations along the loading direction- similar to the case of figures a and c. Interestingly, such behavior is not observed for β_l (figure b and d). Following this chain of thoughts, we do not expect the increase in CTE of laser affected volumes to interfere with the measurement. However, the induced strain resulting from the volume expansion in the neighboring pristine material may play a part in the reduction of the β_l. This hypothesis is further discussed in the next section. The difference observed between the two nanograting orientations provides us with information about the nanogratings' individual layers temperature-elastic coefficients. Intuitively, we can predict that for nanogratings aligned along the loading direction, the non-porous planes are dominant, as these planes are an order of magnitude stiffer than the porous planes and occupy 90% of the volume. The contribution of both planes cannot be neglected for the orthogonal case. This intuition is supported by estimates made in equation 6.1 that considers nanogratings aligned along the loading direction (as shown in Figure 6.2a and c), and equation 6.2 that considers nanogratings aligned perpendicular to the loading direction (as shown in Figure 6.2b and d). The subscripts nl and pl refer to the non- and porous layers, respectively. In the right-hand side, the expression of the dependence between β_l and the local properties β_{nl} and β_{pl} is depicted, where for $V_{nl} \sim 0.9$, $V_{pl} \sim 0.1$ and $E_{pl} \sim E_{nl}0.1$ is chosen, as applied in Chapter 5. From this analysis, it becomes apparent that the trend in Figure 6.2a and c is mostly governed by non-porous layers temperature-elastic coefficient β_{nl}. Furthermore, according to this analysis, we can conclude that the low-deposited-energy minimum, 6.2b and d, should be due to the porous layer. In the next section, we discuss which structural rearrangement could explain these results.

$$\beta_l^{\perp} = \frac{E_{nl}\beta_{nl}V_{nl} + E_{pl}\beta_{pl}V_{pl}}{E_{nl}V_{nl} + E_{pl}V_{pl}} \qquad \rightarrow \qquad \beta_l^{\perp} \sim \beta_{nl}0.9 + \beta_{pl}0.01 \tag{6.1}$$

$$\beta_l^{\perp} = \frac{\beta_{nl}V_{nl}E_{pl} + \beta_{pl}V_{pl}E_{nl}}{V_{nl}E_{pl} + V_{pl}E_{nl}} \qquad \rightarrow \qquad \beta_l^{\perp} \sim \beta_{nl}0.9 + \beta_{pl} \tag{6.2}$$

---

[1]Athermal; An adjective, indicating if the referred quantity is not temperature dependent. For example, in this case, the change in volume expansion is a consequence due to the laser irradiation and not due to the thermal expansion.

6.2 Interpretation

The anomalous properties of amorphous silica are known and studied for nearly a century. These are: the Boson peak [192], the softening upon compression [193], the low-temperature plateau behavior of the thermal conductivities [194], the relation between fictive temperature and density [171], a negative CTE [195, 196] and the one discussed in this chapter, the positive temperature-elastic coefficient. The Boson peak - found in the Raman spectrum band $30\text{-}120\text{cm}^{-1}$ - and the low-temperature plateau behavior of the thermal conductivities - 2.2K <T<90K-, are generally related to the excess of vibration modes in the THz frequency range. The mechanism behind these anomalies and how they correlate one with another have been debated [197]. The conundrum was even bigger for researchers back in time, as the structural model based on SiO_2 tetrahedra network itself was still heavily debated [198, 199, 200]. Experimentally, it is hard to retrieve the molecular structure of glass formers, as the amorphous structure is isotropic, which does not allow us to study the 3D information at macroscopic level as it does for crystalline materials [201]. Consequently, pre-defined models, at the molecular level, are necessary to decipher characterization results made with for instance, X-ray or neutron diffraction methods. An important point is that it is a challenging task to interpret femtosecond laser-induced material-properties changes, because the mechanism itself responsible for the positive temperature-elastic coefficient is not established. In an attempt to understand laser-induced changes, we review previous studies and debates/hypothesis. Although the main focus is on the positive temperature-elastic coefficients, we highlight findings about other anomalies that may allow us to suggest an interrelation between them.

6.2.1 Review on the nature of SiO_2 positive temperature-elastic coefficient

Early record of a positive temperature-elastic coefficient was made by R.B. Sosman in 1927, cited in [202]. The negative CTE below room temperatures was reported in 1942 by J.A. Beattie, cited in [195]. Furthermore, it is noteworthy that the CTE, at and above room temperature, is remarkably low in comparison with other glass formers or even silica's crystalline polymorphs. Anderson *et al.* related these material properties based on thermodynamic relations and postulated that the low-CTE causes a thermal-stiffening effect, cited in [175]. His hypothesis was rejected later on, as other glasses with significant higher CTEs such as GeO_2, BeF_2, also display a positive temperature-elastic coefficient [203]. Other theories suggests that fused silica's open structure would allow transverse vibrations of the bridging oxygen bonds as depicted in Figure 6.3a. This vibration mode would become more dominant than longitudinal ones, due a significantly lower stiffness, causing a shrinkage of Si-Si interatomic distance resulting in a negative CTE [204]. The same low-stiffness bridging oxygen is related to low temperature acoustic losses (an excess of vibrations modes) [205]. Although this could not be the case for fused silica, as X-ray-diffraction measurements pointed-out that there is an insufficient amount of 180° Si-O-Si bond angles [206], $\theta_{Si-O-Si}$ (Figure 6.3a), which would support these transverse vibration modes. Furthermore, this theory would not explain the positive temperature-elastic coefficient.

67
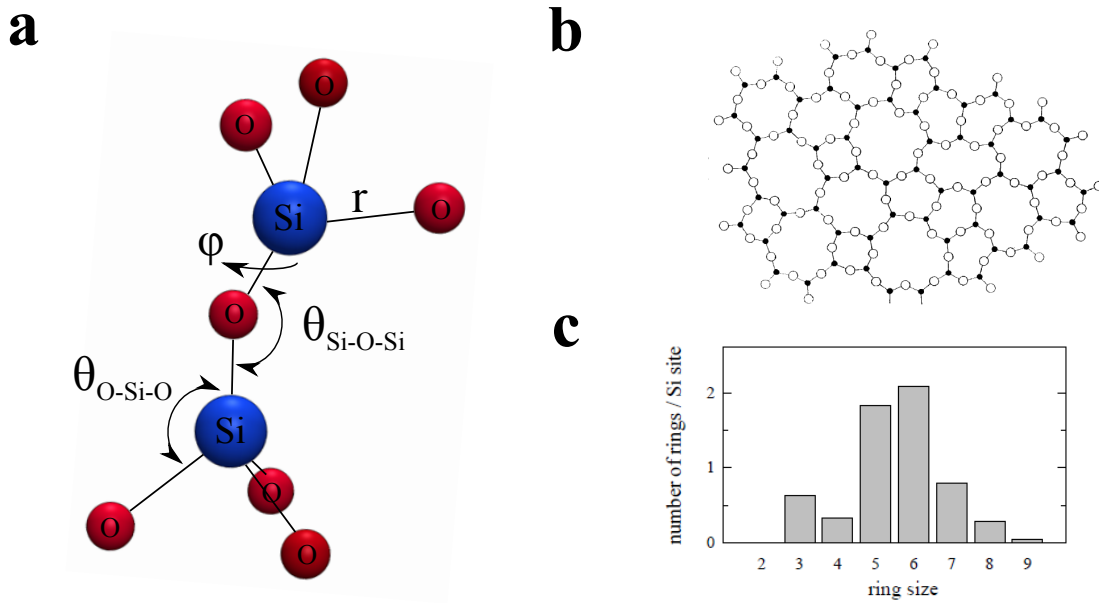
Figure 6.3 – **a***) Two silica, tetrahedrally coordinated silicon by four oxygens and which share both an oxygen, referred as the bridging oxygen. $\theta_{Si-O-Si}$ is the angle of the bridging oxygen, furthermore, r and θ_{O-Si-O} are the short range characteristics of the tetrahedral structure.* **b***) An early impression of fused silica's network envisioned by Zachariasen made in 1932 [198].* **c***) The ring statistics of fused silica, calculated based on the ab-initio molecular dynamics method [207].*

In earlier work (1954), Babcock *et al.* introduced the idea that the anomalous behaviors are due to two co-existing structural phases [190]. Specifically, the two phases would be similar as the low- and high- temperature forms of cristobalite, a polymorphic phase of silica [206]. The idea of a hybrid structure causing the anomaly behavior is adopted, and/or related to, in several works [208, 175, 19, 209]. Before we go deeper in exploring these ideas, let us first discuss key characteristics of glassy and crystalline phases of silica. The main building block of nearly all phases is a silicon atom surrounded by four oxygen atoms forming a tetrahedral molecular geometry. The exception to this is the six-coordinated stishovite, a high pressure phase of silica. Tetrahedra are interconnected one with another by sharing an oxygen, see Figure 6.3a, and the spatial arrangement of tetrahedra, if regular, define different crystalline polymorphic phases. When this arrangement is irregular, an 'amorphous' phase is found and consists of rings of various sizes. The different polymorphs are reached by a bondbreaking irreversible process, due to a pressure and/or thermal load, called a reconstructive transformation. Some of the crystalline phases, such as quartz, tridymite and cristobalite, can also undergo a thermally-driven reversible transformation, i.e. from a α- to a β-form, called a displacive transformation. The former and latter forms exists at low and high temperatures, respectively. Essential information is that the low temperature forms (α) possess a lower density and lower elastic modulus compared to their high temperature counterparts (β). Similarities between cristobalite and fused silica is found in the neutron scattering [210], X-ray measurements [206], Raman spectrum [211], infrared spectrum [212] and have remarkably similar density. In general, the amorphous material shows broader vibration peaks in these spectra, compared to

its crystalline counterparts, but shares similar peak positions. These similarities are mostly found back in the mid-range characteristics, as there are nearly no differences found at short-order range (tetrahedral molecular geometry) among the phases. The mid-range is mainly characterized by the $\theta_{Si-O-Si}$ [199] and ring statistics [213].

In-line with the characteristics described above, Vukcevich suggested that cristobalite has a double potential well [19], as drawn in Figure 6.4. The two minima, $\phi_{\alpha,0}$ and $\phi_{\beta,0}$, correspond to the equilibrium position, $\theta_{Si-O-Si}$, of cristobalite's low- and high-temperature forms. With Δ indicating the threshold energy for a $\alpha \rightarrow \beta$ transformation. $\theta_{Si-O-Si}$ for the α- and β-form is characterized to be $147°$ and $151°$ [192], respectively. According to his theory, the potential well is a superposition of the potential energy of two states and the electrostatic repulsive force between the SiO_2. The "normal" thermal expansion of the tetrahedral SiO_2 causes a decrease of bridging-oxygen angles. The rigid rotation of the tetrahedral SiO_2 shortens Si-Si distance, which effectively increases the repulsive force. The change in balance between the repulsive force and potential energy causes that $\phi_{\beta,0}$ to be the global minimum, at temperatures $T > T_{\alpha \rightarrow \beta}$. Obtaining fused silica large variation in the $\theta_{Si-O-Si}$, Vukcevich theorized that fused silica has two potential wells with two minima, however, unlike their crystal counterparts, do not have distinct transformation temperatures. Instead, the material would gradually transform for an increasing heat, converging to the β form, resulting in a contraction and stiffening effect for higher temperatures [19].
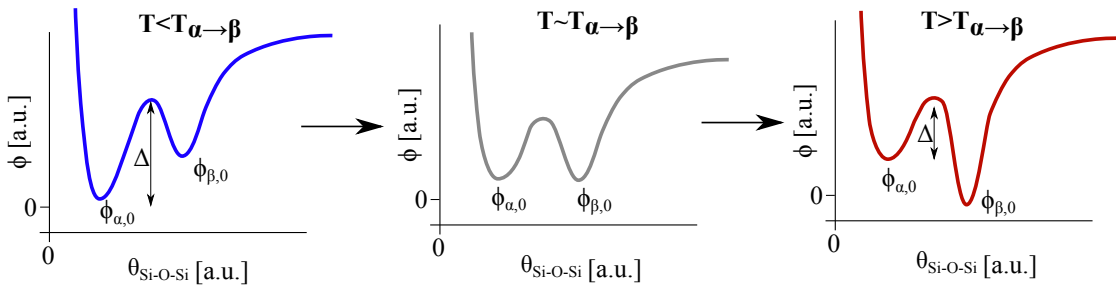
Figure 6.4 *– Cristobalite's potential energy as function of $\theta_{Si-O-Si}$ at three different temperatures, envisioned by Vukcevich [19]. The two minimum locations, $\phi_{\alpha,0}$ and $\phi_{\beta,0}$, correspond to the equilibrium angles ($\theta_{Si-O-Si}$) of cristobalite's low- and high-temperature forms. For temperatures below the transition temperature of $\alpha \leftrightarrows \beta$ ($T<T_{\alpha \rightarrow \beta}$) the minima of the α-form is lower than the β-form, hence $\phi_{\alpha,0}<\phi_{\beta,0}$. For increasing temperatures the potential energy minima shift with respect to each-other, such that for $T>T_{\alpha \rightarrow \beta}$ the potential minimum becomes $\phi_{\alpha,0}>\phi_{\beta,0}$. Δ represents the threshold energy for a $\alpha \rightarrow \beta$ transformation.*

In the period Vukcevich published his work, researchers started to recognize that amorphous silica has more structural order -even though an accurate two-dimensional picture was already drawn by Zachariassen in 1932 [198], see Figure 6.3b, as previously predicted using continuous random network models [214]. The SiO_2 molecules forming closed ring-structures, constructed by three to twelve-membered rings, where the six-membered ring is the most abundant [213, 215, 200, 207, 210], see Figure 6.3c. With the aid of molecular dynamics simulation Huang *et al.* studied in several works the anomaly behaviors [216, 217]. Although the

simulation-results could not fully reproduce the experimental-observations [216], a positive temperature-elastic coefficient and the softening upon compression are demonstrated. According to their analysis, $\theta_{Si-O-Si}$ cannot specifically be accounted to an anomalous behavior, but rather due to abrupt localized Si-O-Si bond rotation around the Si-Si axis affecting the ring-geometry. These changes would gradually occur throughout the bulk for a range of temperature or pressures, converging to a network containing symmetric ring-geometries, see Figure 6.5. The driving force for the abrupt rotation of the Si-O-Si bond would be due to the tension in the network imposed by the "normal" thermal expansion of the tetrahedral SiO_2. The convergence to a more symmetric structure would equivalently occur for cristobalite $\alpha \leftrightarrows \beta$ transformation, specifically for the six-membered ring. The symmetric form of the six-membered ring -the β form- would be stiffer than the asymmetric form- the α-form, explaining the thermal stiffening effect. Although the symmetric six-membered ring occupies more volume, the CTE of the β-form is lower - a possible mechanism causing the low CTE of this form is given in [218]. It should be stressed that it is not stated that the material is composed by two crystalline phases (α and β), the microcrystal theory has been rejected long before. Nevertheless, fused silica material temperature dependent properties share similarities with the low- and high-temperature forms of the crystalline phases, but over a broader temperature range due to its amorphous character. Recognize, that Huang's observations can be described as a double potential well, however in this case as function of the rotation the Si-Si axis.
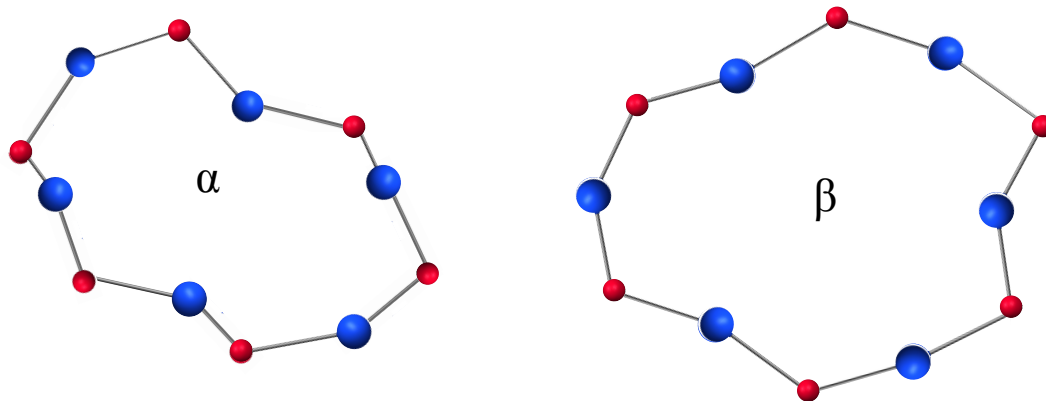

Figure 6.5 – *The six-membered ring for cristobalite's α and β form. The six-membered ring of the former, the low temperature form, is the non-symmetric form. The high-temperature form, β, is symmetric and forms a stiffer structure.*

6.2.2 Review of the change in positive temperature-elastic coefficient

Let us first start discussing mechanical compression studies. Fused silica softens with (cold-)compression pressures from 100 kPa to 3 GPa, at room temperature. In these pressure regimes, it is observed that the intensity of the (anomalous) Boson peak reduces [219, 220, 221]. Furthermore, evidences are given that the average and spread of $\theta_{Si-O-Si}$ become both smaller [219, 220], subtracted from the mainband information using *in-situ* Raman spectroscopy measurement. Compressing fused silica beyond 9 GPa, the material undergoes irreversible densification; up to pressures of 50 GPa the SiO_2 coordinate number converges from 4 to 6 and a so-called "high density phase" is reached [222] - converging locally to stishovite-like structures [223]. Unloading from the irreversible pressure regime and subsequently reloading the material shows that the softening upon pressures is permanently reduced or either not present anymore [181, 224]. Guerrette *et al.* studied the temperature-dependent modulus for hot-compressed and quenched Suprasil 300 silica glass (class I) and demonstrated a reduction of more than 80% of the positive temperature-elastic coefficient - for compression pressures equal to 6 GPa and temperatures of 1100 °C [135]. When considering the mechanical-densified structure, a clear distinction should be made between cold- and hot- compressed silica. Martinet *et al.* studied the Raman spectra versus densification for the two methods [225], and observed that the vibration frequency and the population of the breathing three-membered ring mode is mostly affected by cold compression. This was also observed in [219]. While in the case of hot-compression, nearly no increase is obtained in three-membered-ring's population, but rather an increase of five- and seven-membered rings at the expense of the six-membered ones [174]. In addition, material properties such as Young's modulus, and elastic pressure limit are significantly different, for cold and hot compression densification methods [174], obtained at similar densification ratios, which indicates that the end result is dependent on the pressure-temperature pathway [226]. Finally, the influence of shear stress on the elastic limit should not be left unnoticed as fused silica's irreversible pressure regime appears at lower stress under the action of shear stress, and a larger amount of the three-membered rings is obtained for similar densification [227]. The lack of correlation between densification and three-membered rings formation is also demonstrated in [228, 229, 230]. Applying different loading conditions, thermally, mechanically or a combination of the two, gives distinct results, nevertheless it seems that they share common changes, which are the reduction of the six-membered ring, $\theta_{Si-O-Si}$ and the increase of coordination. The dependence of the pressure-thermal history on the structure of permanent densified glass is further discussed in greater detail in [180, 231]. In other studies, correlations are made between thermal history (fictive temperature) and anomalous behavior [175, 221]. In the case of fused silica, the density increases along with the fictive temperature and, as for mechanical compression, $\theta_{Si-O-Si}$, is inversely related to the fictive temperature [232]. Specifically, Le Parc studied the positive temperature-elastic coefficient for a class I fused silica. He showed that for a fictive temperature difference of 400°C, a change of approximately 4% is found[175]. In earlier work by D. Fraser, it was shown that the TCF of a torsion bar is reduced by 7% and 22% for a class I and III fused silica, respectively, corresponding to a fictive temperature change of 400°C [233]. Likewise for the

other anomalous behaviors [221] and structural changes [232], no large changes are reported.
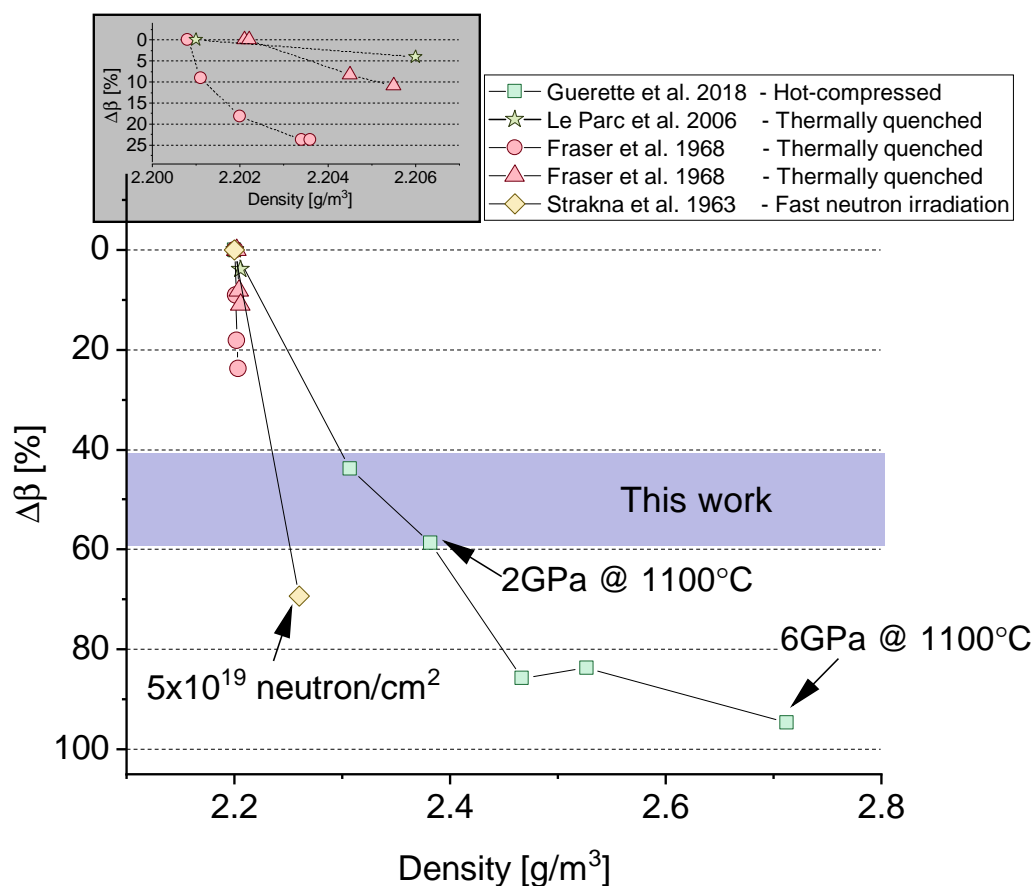
Figure 6.6 – *A summary of $\Delta\beta$ found in the literature. The dataset are found in, Guerrette et al. 2018 [135], Le Parc et al. 2006 [175], Fraser et al. 1968 1968 [233], Strakna et al. [234].*

Apart from mechanically- and thermally- driven compaction, it is known that irradiation-induced compaction has also an impact on the anomalous properties. Strakna *et al.* investigated the elastic positive temperature-coefficient of fast-neutron irradiated fused silica -knock-on radiation- for the temperature range 100 K to 300 K [235]. The positive temperature-elastic coefficient reduced by approximately 70%. In other work, it is shown that the main band shifts towards higher frequencies and becomes narrower due to fast neutron irradiation [236]. Typically, in the case of knock-on radiation maximum reduction of 10° for $\theta_{Si-O-Si}$ and a maximum density increase of ~3% (~2.26g/m^2) [237], are found. For the ionization type of radiations, a more gentle reduction is found, approximately 6% in the case of γ radiation. The diminishing of the other anomalies due to irradiation have been also reported [234, 238], i.e. the excess of low temperature vibration modes.

Finally, the relation found between the fraction of the Si-molecules and anomalous behavior in composite glasses has been reported [239, 240]. In these works, the temperature dependency of the Young's modulus is nearly suppressed. In recent work, Shi *et al.* showed, based on a neutron scattering, that the population of the six-membered rings increases along with the Si-concentration, at the cost of the four- and five-membered rings [210]. Finally, in these works, [239, 210], it is recognized that there exists a correlation between the anomalous behavior and the temperature behavior of $\theta_{Si-O-Si}$, subtracted from the main band of the Raman spectra. In general, the reduction of fused silica's anomalous behaviors find close correlations due primarily to compaction, even though compaction mechanisms are different in nature. For instance, no bonds are broken when compressing the material in the elastic regime, and yet, similar results are observed for bond-breaking compaction, due to irradiation for example. Some investigators argue that the material is compacted to a more homogenized structure [203]. Otherwise, some would argue that the boundary Δ between the two minima in the double potential well, as sketched in Figure 6.4, is increased by external or internal irreversible stresses [241, 217]. These arguments and findings support the ideas of two coexisting phases being responsible for the anomalous behavior.

The reduction of β found in the literature is summarized in Figure 6.6 and is plotted versus the density. No strong correlation is found between the densities among the various studies. Our result, regarding the non-porous layer embedded in the nanograting modification, is plotted independently of the density as an horizontal zone.

6.2.3 Femtosecond laser induced positive temperature-elastic coefficient reduction

In view of the preceding literature review, let us revisit our results from the previous section. The Regime I modification shows nearly no reduction in the TCF, whereas the Regime II modification exhibits a remarkably high reduction. We estimate, by calculating the local laser affected material property β_l, a maximum reduction of ~7% and ~50% for Regime I and II, respectively. The former seems to be in close-agreement with the other ionization-type radiations, where the reduction obtained for a Regime II is exceptionally high for this category. Moreover, in the former modification, for both non- and porous layers β_l seems to reduce. Interestingly, they appear to have distinct trends versus the energy deposited. As discussed above, the reduction of the positive temperature-elastic coefficient is observed with different structural rearrangements. In the following, we argue how the observations from other works might interrelate with our results.

Compaction solely due the change of thermal history seems not to reach the 50% reduction we obtained in our results. Furthermore, a factor three difference is obtained between the low- and high-OH content silica [233]. This correlation is not found in our case, assuming that the thermal history is similar for both cases. Based on the former observations and the magnitude of the reduction, we suggest that the fictive temperature has no preponderant effect on β_l.

The knock-on radiation (neutron radiation) and temperature assisted mechanical compression is capable of suppressing the abnormal behavior beyond the values we obtain. Moreover, both for the elastic and irreversible compression regimes a diminishing anomalous behavior, i.e. the Boson peak, is observed. However, no data is found in the literature, which relates elastic compression and the positive temperature-elastic coefficients. In the case for the nanograting regime, in between the modified-volume the unexposed material is compressed by the modified volume expansion, where pressure values correspond to the elastic regime [179]. To further understand the preponderance of elastic compression, we design an additional experiment, where we study the induced stress and β_l as function of the modified volume fraction (V_l). The stress is indirectly measured using the bimorph structure described in Chapter 3.1 and the stress estimation is discussed in details in Appendix A. Figure 6.7a depicts the stress evolution as function of V_l and Figure 6.7b the measured TCF and estimated $\beta_l^{\perp}$. The exposure conditions are given in the captions of the figures. The TCF seems to scale proportionally with the line spacing, where the stress starts to decay to a maximum value above a line spacing 4 μm. Based on our comparative study, we like to state that the elastic compression has no significant influence on the TCF's reduction, as no correlation is found between $\hat{\sigma}_l$. Note, that the TCF is not linearly dependent on V_l, which is not surprising as we expect an interfering effect for closely packed exposure strategies [159]. The saturating behavior of stress and strain is, in Appendix A, also demonstrated for other substrate thicknesses, a larger volume fraction range and other exposure conditions. At this point we have further established that the change of the resonator TCF is due a change of β_l and not a secondary effect.
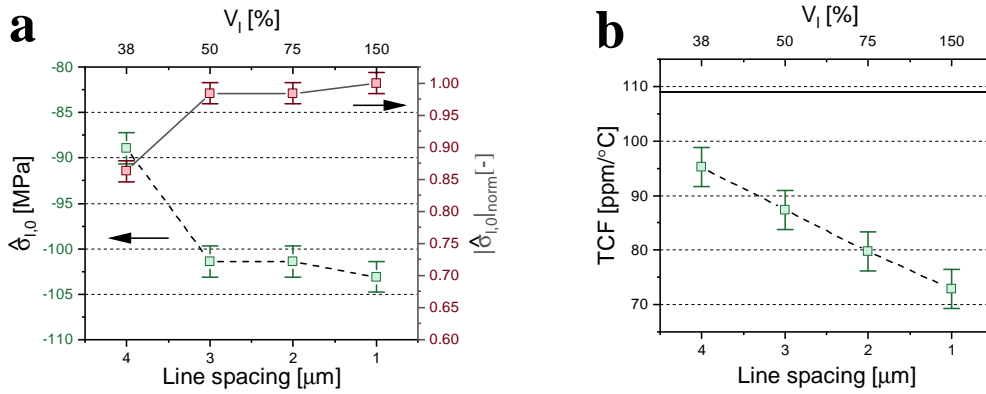
Figure 6.7 – *Two volume fraction studies, demonstrating that there is no correlation between induced stress and TCF. **a**) The temperature invariant average stress due to volume expansion in the LAZ ($\hat{\sigma}_{l,0}$) conducted from a bimorph structure. **b**) The TCF versus the line spacing and volume fraction, conducted from the resonance experiment. The exposure conditions are; pulse energy of 300 nJ, repetition rate of 750 kHz, scanning velocity of 5 mm/s, pulse width of 300 fs and a wavelength of 1030 nm.*

Neutron and femtosecond laser irradiated fused silica share similar characteristics in the Raman spectra i.e an increase of the D2-peak is observed - an increase of the three-membered

ring population -, narrowing and red-shift of the mainband. Although, there is a clear distinction in the magnitude of changes. Both Shcheblanov *et al.* [242] and Vukelic *et al.* [243] discussed, for femtosecond laser irradiated SiO_2, that three-membered-ring's structures are created at the cost of mainly the six-members (and higher order ring members). Furthermore, Shcheblanov *et al.* observed, based on a MD-simulation, that the Si-coordination is converging to higher numbers, from 4 to 5 [242]. In the same work, a maximum change of bridging bond angle is approaching 4 °-conducted from the Raman spectra's mainband-, where for the neutron irradiation, values in the order 10 ° are achieved. In addition, the density increase is an order of magnitude larger, and the three-membered ring population is bigger for the neutron irradiation. Nevertheless, we envision that the generation of three-membered rings at the cost of the six-membered rings could be responsible for the reduction of β_l. The sharp D_1 and D_2 peaks correspond to a symmetric form which would be, intuitively, the stiffer temperature-form. Therefore no stiffening effect upon a temperature increase is expected for these ring-numbers, as this would be the case for the six-membered rings in fused silica and cristobalite. Furthermore, unlike higher order ring members, the three- and four-membered rings has a lower degree of freedom, implying a higher threshold energy (Δ in Figure 6.4) between two possible ring geometries. However, no sustainable large difference is found in the D_1 and D_2 information for a Regime I and II modification, for similar pulse energies applied in our work [79]. As a matter of fact, we found in the literature for high pulse energies, $\geq 1\mu J$, higher values of the D_2-peak for the Regime I modification, a factor of three to five [244, 49], than found for the Regime II modification. This does not correlate with the β_l for the two types of modifications and, hence, cannot solely be explained by the generation of the (symmetric) low number ring-members. In simulations from Shcheblanov *et al.*, the structural changes are observed for a Regime I modification and hence the generation of the porous layers is omitted. We believe that the addition of porous layers plays a significant role in the reduction of β_l.

The mechanism responsible for these low values might be due to the same mechanism as discussed in the previous chapter for the Young's modulus. We envision that a mechanism equivalent to hot compression is responsible for the high Young's modulus [160] and refractive index [60] obtained for the non-porous layer. At the porous-layer locations, higher pressures are generated, which would pressurizes the non-porous layer. The pressure and elevated temperature would lead to higher densification. According to the work of Guerette *et al.*, pressure quenched at 2 GPa and 1100°C would result in a reduction of ~50% [135]. We would like to emphasize, that we predicted similar pressures to explain the high Young's modulus of the non-porous plane [160]. Hot-compression would lead to seven-membered rings at the cost of the six-membered ones, in the addition of the ionizing based transformation. It is not clear, for us, if this transformation is the basis of the low values we obtain for β_l. It may be indeed, that the seven-membered-ring's high-temperature form is of lower stiffness, compared with his low-temperature form counterpart. Guerette *et al.* [174] mention that for hot compressed conditions, the material is converted to a more homogeneous structure, with smaller pore sizes. This could mean, that the network does not allow displacive transformation, simply

due to the lack of space. The latter thought, implies that the energy threshold for a displacive transformation has increased. Future studies should reveal if these statements are indeed true. Finally, this work opens-up other question, such as; how does the other anomalies behave under the action of femtosecond laser irradiation and how does it correlate with the results obtained in this chapter.

6.3 Summary

Let us summarize the key findings in our experiments and from the literature:

- A reduction of the temperature-elastic coefficient is found for regime I and II modifications. The regime I modification reduces down to about ~7%, while the regime II modification is lowered by ~50%.

- Using an approximation, we estimate the contribution of the individual layers, embedded in the nanograting modification, to the reduction of temperature-elastic coefficient. There, we could conclude for the non-porous layers that the temperature-elastic coefficient decreases as function of the deposited energy.

- In the literature, a similar mechanism as for the low- to high-temperature transformation of silica's crystalline phases, is responsible for fused silica's (abnormal) positive temperature-elastic coefficient. Huang *et al.* pointed out that in particular the six-membered ring is responsible for the stiffening effect [216].

- In Figure 6.6, a summary is given of works reporting a reduction of the temperature-elastic coefficient imposed by various densification methods.

- Based on our literature review and our measurements, we suggest that a combination of internal pressures at elevated temperatures *might be* responsible for the densification mechanism observed in nanogratings and the related changes of thermomechanical properties.

7 Thermal expansion [1]

Although, chronologically this work was performed before the elastic-property related work presented before, we place this chapter here, since we use the elastic-property information for a refined estimation of the CTE. Nevertheless, the work presented in [159] was an important milestone in this thesis work, as we gave experimental evidence of the capability to locally tune fused silica's CTE with a laser.

As discussed in Chapter 3.1, to study this material property change, the thermal deflections of a bimorph structure placed in a temperature controlled environment is measured with a digital holographic microscope. In this chapter, the volume variations due to laser exposure are reported as well. Each substrate contains eight cantilevers and are fabricated out of 500 μm-thick fused silica substrates (Corning 7980-0F) using a two-step process combining femtosecond laser exposure and chemical etching as described in [90] and Chapter 3.1. The substrates have a 1000 ppm OH content and traces of Cl in the order of 100 ppm (class III fused silica). To study a wide range of exposure conditions, two femtosecond laser systems having different pulse characteristics are used. The first one emits 50 fs-pulse (an OPA from Amplitude Systèmes, emitting at 850 nm) and is capable of producing regime I type of transformations, while the second one is a Yb-doped fiber amplified system (Amplitude Systèmes, 380 fs at a wavelength of 1030 nm) and is capable of producing regime II type of transformations.

Two types of experiments are conducted; first, we investigate the preponderance of possible effects affecting the thermal response of the bimorph structure, and second, we study the thermal response for different laser exposure conditions.

7.1 The effect on the thermal response of a pre-strained bimorph

In the problem description in Chapter 2 and in Chapter 3.1, it is discussed that the effective thermal expansion behavior of the bimorph structures might be not only due to the CTE difference between the laser exposed and pristine volume. The pre-strained material, due to the volume variation of the laser exposed material, and the temperature dependent

---

[1]Part of this chapter has been published in [159]

Young's modulus, causes also a change of volume expansion upon a temperature change. To demonstrate the contribution of the pre-strained effect we designed an experiment for which laser-exposure conditions are kept constant, but the filling factor of the exposed volume is varied. The motivation is to validate our model (Equation 3.19) by effectively changing the average CTE ($\hat{\alpha}_{l,0}$) of the LAZ and the initial bending strain (ϵ_0). The filling factor was altered by changing the line spacing between the individual lines (l_s in Figure 3.1). The modifications were written using the fiber laser emitting 380 fs at a wavelength of 1030 and 250 nJ-pulses, at a translation speed of 1.7 mm/s and a repetition rate of 800 kHz.

It is known that the femtosecond laser exposed regions exhibit an increase in defects, such as non-bridging oxygen hole center (NBOHC) and E' centers [245], and the generation of interstitial oxygen [67]. In order to minimize possible long-term changes, for instance due to the outgassing of trapped oxygen or quenching of defects, the samples are thermally annealed to remove these points defects and interstitial oxygen. The thermal response of the samples is measured, before and after annealing, using the previously described experimental setup. The annealing step is done in a furnace under normal atmospheric conditions, at 300 °C for 10 hours. These annealing conditions are adopted from [82]. Additionally the initial deflection at room temperature due to the volume expansion after femtosecond laser exposure, is measured using a white light interferometer (WYKO NT1100) and is reported in Table 7.2 -these values are used to estimate r_0. It should be pointed out that annealing has no large effect on δ_0 and therefore, variation of the $r_\beta(T)$ remains small after annealing.

Table 7.1 – **Measured initial tip deflections (δ_0) after exposure and annealing, with a measurement uncertainty of 200 nm. The third column lists the difference between the two measurements.**

l_s (μm)	δ_0 (μm) before annealing	δ_0 (μm) after annealing	Difference (%)
2	-76.1	-78.7	3.4
4	-65.7	-64.7	-1.5
6	-50.5	-50.2	-0.6
8	-40.8	-40.8	0
10	-34.4	-34.5	0.29

The graph in Figure 7.1, considers an example of thermal tip displacements in nanometers as function of temperature. The slope of the curve before annealing is negative. In other words, the cantilever bends down due to a temperature increase. After annealing an opposite effect is observed. One might conclude that the difference of the thermal expansions ($\Delta\alpha = \alpha_s - \alpha_l$) is switching sign due to the annealing step. This behavior is confirmed when observing the thermal displacement rate ($\partial\delta/\partial T$) for all the line spacing, see Figure 7.2a. When observing the trend as function of the volume fraction (V_l), one would expect an increasing magnitude of thermal deflection rate for higher volume fractions, if the CTE difference dictates the thermal behavior of the bimorph. However, this is not observed for the unannealed case in Figure 7.2a; the magnitude of the thermal deflection rate does not increase, instead, it converges to a zero value for higher volume fractions. This indicates that another effect is interfering with the
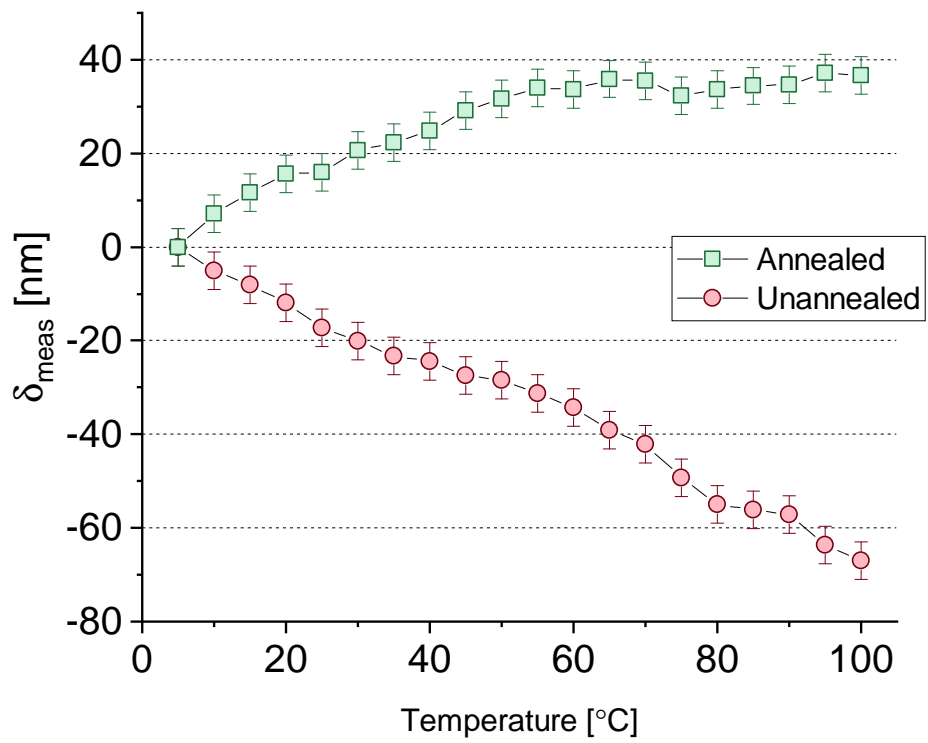
Figure 7.1 – *The measured thermal deflection (δ_{meas}) for annealed and un-annealed specimens in the case of Regime II exposure. Exposure conditions: E_p=250 nJ, E_d=10 J/mm^2, pol=90° and l_s=4µm.*

CTE characterization. The error-bar on the measured displacement rate ($\partial\delta_{meas}/\partial T$) is based on the 95% confidence interval obtained form the linear regression estimation method and found typically smaller than 0.2nm/°C. Where for $\partial\delta_\alpha/\partial T$ uncertainties on the dimensions are included.

When subtracting the term related to the pre-stress effect (δ_β) (see Chapter 3.1) from the measurement, we observe that the thermal bending rate only caused by the thermal expansion difference (δ_α) is negative for both cases (Figure 7.2b). From the latter, it becomes apparent that the magnitude of the thermal strain rate decreases when an annealing step is applied, hence α_l converges to α_s, which may indicate that some fine reorganizations of the material matrix might be taking place. From the bottom graph that excludes the initial strain, we conclude that in Regime II, the modified volume expands more than the unmodified region, hence $\alpha_l > \alpha_s$. Indeed the magnitude of δ_α decreases as function of the line spacing, as the exposed volume decreases, and due to the annealing step. In Chapter 8, a dedicated study about the annealing induced changes of thermal expansion behavior is discussed in greater details.
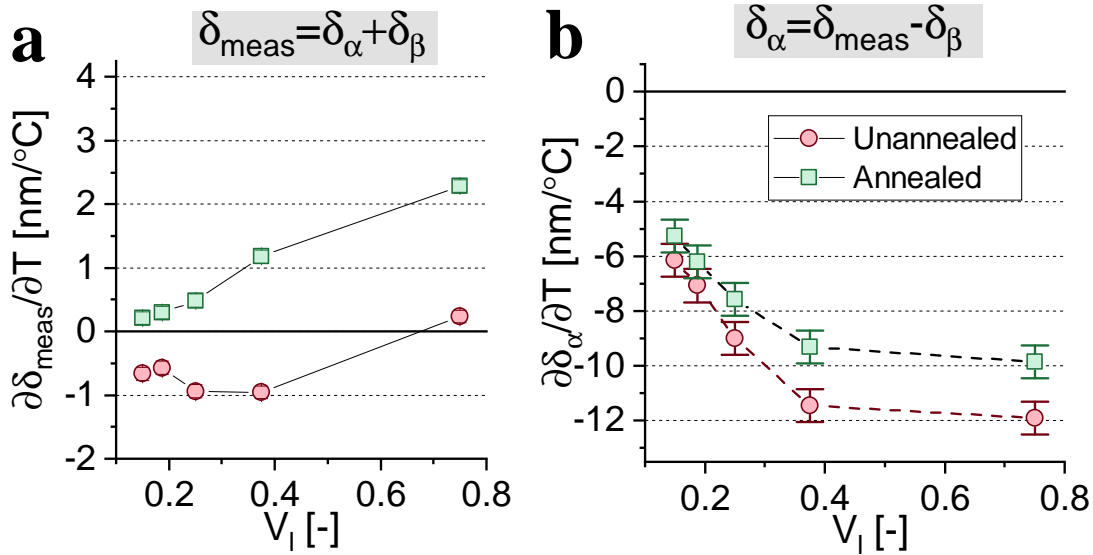
Figure 7.2 – *The thermal deflection rate ($\partial\delta/\partial T$) for the annealed and unannealed case as function of the volume fraction of exposed material (V_l) in the case of Regime II exposure. **a**) Measured thermal displacement rate, **b**) estimated thermal displacement rate only due to the CTE differences ($\partial\delta_\alpha/\partial T$). In the top of each graph, the contribution of the two main thermal expansion effects, δ_α and δ_β, can be conducted from the equation. Exposure conditions; a pulse energy of 250 nJ, a deposited energy of 10 J/mm^2, the repetition rate is 80 kHz, N.A. of 0.4, a wavelength of 1030 nm and a polarization of 90°.*

7.2 Thermal response vs deposited energy in Regime I and Regime II

In this section, we discuss the thermal deflections as function of the exposure conditions and, in particular, the pulse width and the deposited energy. The regime I modifications are

created by irradiating the specimen with 50 fs-pulse length and 250 nJ pulse energy, while regime II is obtained by using 230 nJ pulses using the longer pulse laser. The scanning speed is adjusted to reach a desired deposited energy level. The number of pulses is directly expressed by the ratio between repetition rate and the scanning speed. In regime I, it ranges between 26.5 and 1600 pulses per micron and for regime II, between 18 and 1200 pulses per micron. The line spacing was fixed and set to 4 μm, hence more than two times the width of the laser affected zone. This choice is motivated by observations of cross-talk phenomena [166] when the spacing becomes comparable or smaller than the laser affected width. In addition, for regime II, two polarizations are chosen, 0 ° and 90° (defined as the angle between the electrostatic vector field and the writing direction), to validate the effect of self-organized nanograting orientations. The transverse and axial properties are characterized for a regime II modification, whereas for the Regime I modification, only the transverse properties are studied. The remaining experimental details for each substrate are given in Table 7.2, as well as additional information regarding the substrate thickness (t_c) and laser affected length (L_l). The latter two are important for understanding the differences in measured values. At last, the results obtained in the remaining of this chapter are regarding annealed samples at 300 °C.

Table 7.2 – **The experimental details for each substrate.**

Substrate	τ_p [fs]	E_p [nJ]	Pol [°]	l_s [μm]	L_l [mm]	t_c [μm]	Orientation
Regime I - A	50	250	90°	3	4800	480	$\perp$
Regime I - B	50	250	90°	3	2000	534	$\perp$
Regime II - C	300	230	0°, 90°	4	4800	560	$\perp$
Regime II - D	300	230	90°	4	4800	440	$\perp$
Regime II - E	300	230	90°	4	4800	583	$\perp$
Regime II - F	300	230	0°	4	4800	538	$/\!/$
Regime II - G	300	230	90°	4	4800	497	$/\!/$

The measured athermal and thermal deflections are depicted in Figures 7.3a,b and 7.4a,b, for transverse and longitudinal writing directions, respectively. The corresponding estimated strains, occurring in the laser affected layer, is depicted in the remaining figures (c and d). For the transverse case (Figure 7.3a), the athermal tip deflection (δ_0) of regime I and II displays an upward and downward movement, respectively. Meaning that the net density increases and decreases for a regime I and II modification, respectively. The distinction in volume variation between the two regimes is well established in other works, [90] and [67]. The curves of substrates regime I - A and - B do not overlap, neither do they have equal slopes, which is due to the difference in laser affected length (L_l). Evidently, the corresponding strain shows an overlap and a similar slope, see Figure 7.3c.

The measured thermal deflections also show an opposite behavior for the two regimes, see Figure 7.3b. Note that the thermal movement is in opposite direction with respect to the deflection due the athermal volume variation (δ_0). The reason for this is that the thermal movement due to athermal strain and the positive temperature-elastic coefficient is dominant in this experiment. The stiffening effect of the prestrained substrate for an increasing temperature,

forces the cantilever to bend towards its initial position. As we will see later, there is also a contribution to the thermal deflection due to the CTE difference. The corresponding thermal strains in the laser affected layer are given in Figure 7.3d, where maximum values are in the order of 10 ppb.

The regime II modification and the two orthogonal polarization cases ($0°$ and $90°$), controlling the nanograting orientation, is tested for the axial properties, the results are given in Figure 7.4. Unlike for the transverse case, a low and high deflection magnitude are observed for the $0°$ and $90°$ polarization cases. This effect is not observed for the transverse case in our experiment (Figure 7.3), nor in other works [90]. Nevertheless, based on the conclusions we made about the density of the porous and non-porous planes in Chapter 5, we indeed expect a dependency of the volume expansion on the nanograting orientation. It is therefore puzzling to observe that the transverse direction is insensitive to the nanograting orientation.
It is further interesting to notice that for the volume expansion of substrate G, polarization of $0°$, an inverse trend is obtained, see inset of Figure 7.4a. Instead of a peak, it displays a dip in magnitude of δ_0. This might be due to the volume expansion in transverse direction ($\epsilon_l^\perp$), which imposes a contraction in axial direction due the Poisson's effect, $\hat{\epsilon}^{\varparallel} \sim \hat{\epsilon}^\perp \nu$.

7.3 Estimation of the CTE of laser exposed silica

Let us consider equations 2.5-2.12 and 3.19, and rewrite them as depicted in equations 7.1 and 7.2. Based on the measured values, we derive the thermal deflection due to the CTE differences $\frac{1}{r_\alpha}$. The uncertainty on the estimation of $\alpha_{l,0}$ described in [159] is rather large, due to the lack of knowledge about the elastic properties. In this estimation, we implement the values for $E_{l,0}$, from the previous discussed characterization, presented in Chapter 5.

$$\alpha_{l,0}^\perp = \frac{1}{r_\alpha} \frac{1}{6} \frac{t_s^2}{t_l} \left(\frac{V_s}{V_l} + \frac{E_{s,0}}{E_{l,0}^\perp} \right) \frac{1}{\Delta T} + \alpha_{s,0} \tag{7.1}$$

$$\alpha_{l,0}^{\varparallel} = \frac{1}{r_\alpha} \frac{1}{6} \frac{t_s^2}{t_l} \left(\frac{1}{V_l} \frac{E_{s,0}}{E_{l,0}^{\varparallel}} \right) \frac{1}{\Delta T} + \alpha_{s,0} \tag{7.2}$$

The results are shown in Figure 7.5, which corresponds to the substrates discussed in the previous section. To test the repeatability of the CTE tuning process, three additional substrates were exposed and measured, the corresponding datapoints are illustrated with lighter shade of green. The results are also shown in Figure 7.5. (The labels I and II indicate the modification regime). The graphs represents the mean values, with error bars based on estimates of the geometrical measurement errors for laser affected zones (extracted from paper [166]), on the instruments errors (white light interferometer and digital holographic microscope) as well as error estimates on material parameters based on previous works [42, 164]. The estimated CTE for regime I converges to a value factor two lower, roughly, than the pristine material.

Figure 7.3 *– The room temperature and temperature-dependent measurements for the regime I and II types of modifications, annealed at 300° C and lines written transversely with respect to cantilever.* ***a, b)*** *The measured athermal,* δ_0, *and thermal tip deflection,* $\partial \delta_{meas}/\partial T$. ***c, d)*** *are the estimated average volume expansion,* $\hat{\epsilon}_{l,0}^{\perp}$, *and thermal strain,* $\partial \hat{\epsilon}_l^{\perp}/\partial T$, *in the laser affected layer. For regime I, the pulse energy is 250 nJ, the repetition rate of 120 kHz, the pulse width is 50 fs, a wavelength of 850 nm, N.A. of 0.4 and a line spacing of 3 μm. For regime II the pulse energy is 230 nJ, the repetition rate is 80 kHz, the pulse width is 300 fs, a wavelength of 1030 nm, N.A. of 0.4 and a line spacing of 4 μm, the latter is done for a polarization of 0° and 90°.*

It approaches 0.3 ppm/°C for deposited energies above 100 J/mm². The CTE's mean value for regime II, and polarization of 90°, makes a sharp increase for deposited energies below 20 J/mm² and drops for higher values. We can state that the CTE increases strongly, approximately by a factor two. For regime II and polarization 0°, a similar trend is observed when compared to the perpendicular polarization state. For low deposited energies below 20 J/mm², the values seem to overlap. For higher deposited energy the values are slightly lower than the perpendicular polarization.

The estimation on the axial CTE ($\alpha_{l,0}^{/\!/}$) is given in Figure 7.6. For both polarization cases, lower values are obtained than for the transverse properties. In the case when nanogratings are oriented along the cantilever's long axis and a polarization of 0°, nearly no change is observed.
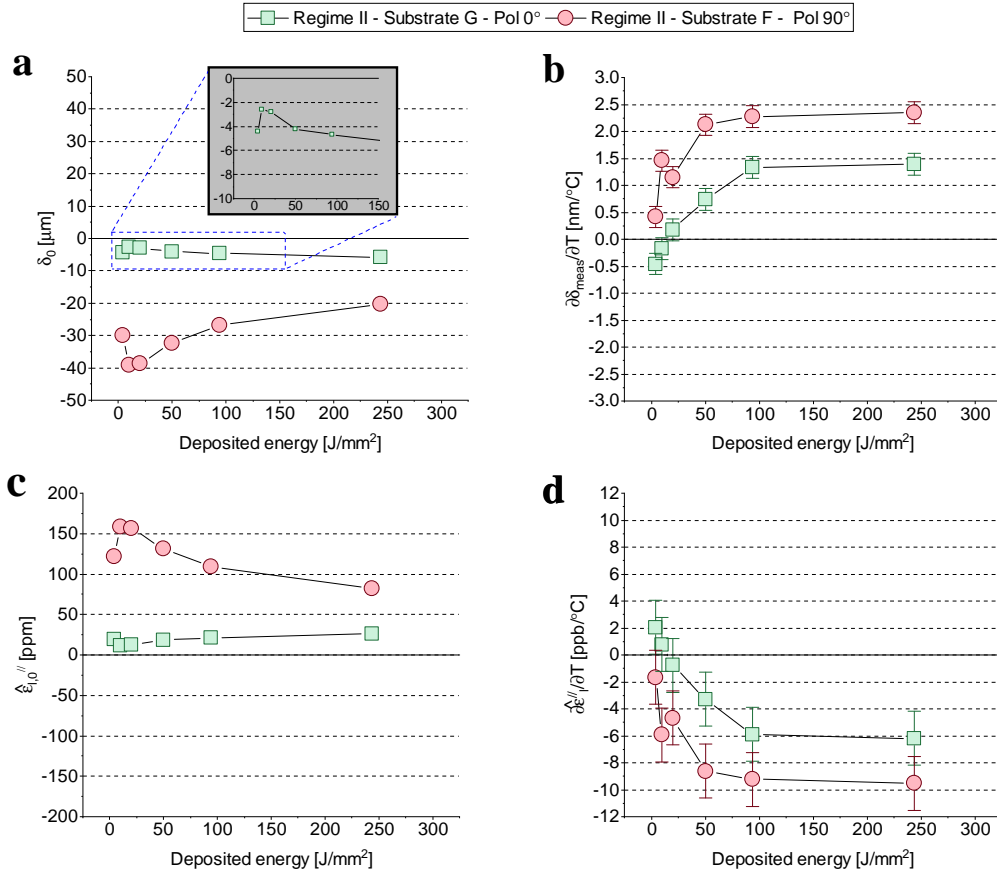
Figure 7.4 – *The room temperature and temperature-dependent measurements for a Regime II type of modification, annealed at 300° C and lines written along the cantilever.* ***a****,* ***b****) The measured athermal, δ_0, and thermal tip deflection, $\partial\delta_{meas}/\partial T$.* ***c****,* ***d****) are the estimated average volume expansion, $\hat{\epsilon}_{l,0}^{\parallel}$, and thermal strain, $\partial\hat{\epsilon}_l^{\parallel}/\partial T$, in the laser affected layer. The pulse energy is 230 nJ, a repetition rate of 100 kHz, a pulse width of 300 fs, a wavelength of 1030 nm, N.A. of 0.4 and a line spacing of 4μm.*

The Regime II modification shows a slight increase in CTE for low deposited energies, while for fluences above 20 J/mm^2, a decrease is observed. A similar trend (peak, followed by a decrease) has been noticed for etching rates versus deposited energy experiments [246] as well as for volume variation vs deposited energy range, and finally, the stress vs deposited energy; suggesting a correlation between the two [90]. In [90], we suggested that the abrupt decreasing volume variation was due to crack formation in the modified volume. However, in the next chapter, we would like to put forward that the decrease in volume expansion and CTE, at higher deposited energies, could be due to the densification of the non-porous layers.
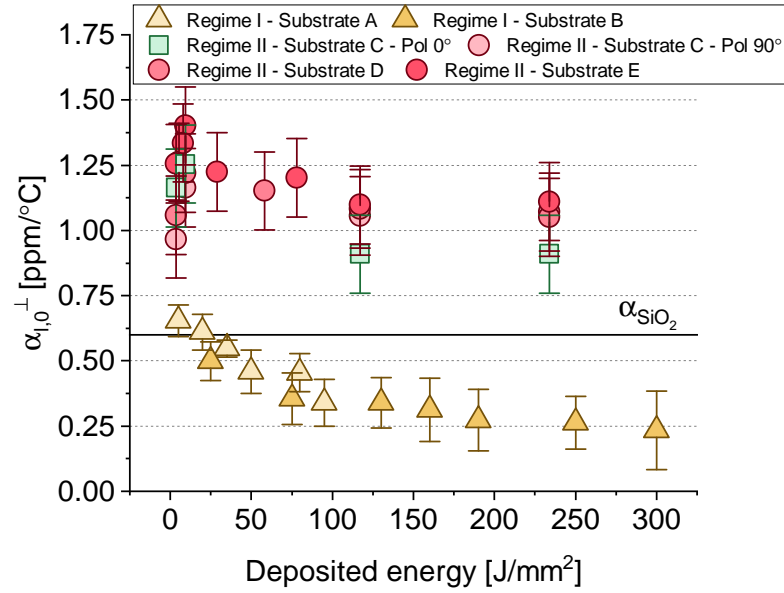
Figure 7.5 – *The estimated transverse CTE for Regime I and II as function of deposited energy, with both at a polarization of 90°, and additionally at a polarization of 0° for Regime II. The value for pristine silica is shown as reference.*
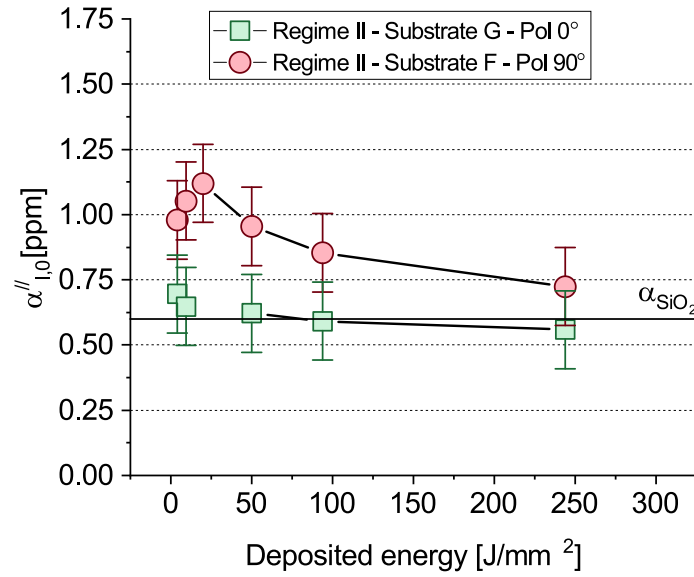
Figure 7.6 – *The estimated longitudinal CTE for Regime II as function of a deposited energy, with both at a polarization of 90° and 0° for Regime II. The value for pristine fused silica is shown as reference.*

7.3.1 Discussion on the estimation

The CTE changes due to laser-exposed fused silica is non-trivial. In general, for the vast-majority of materials, a trend is recognized between density and thermal expansion, where the

density and the CTE are inversely-proportionally related [247]. For both modifications, this interrelation also seems to exist: regime I with a higher density and a lower CTE, and regime II with net lower density and a higher CTE. Nonetheless, we elucidated in Chapter 6 that fused silica's CTE is abnormally low and even negative at temperatures below 200 K. Recently, in-situ neutron scattering has been conducted to retrieve the short-range thermal expansion [248]. They found that the SiO_2 molecule expands to ~9 ppm/$^\circ$C, which is considered as a "normal" thermal expansion coefficient. Furthermore, they found that at medium ranges -bridging-oxygen angle and the ring size- the CTE is even larger, ~21 ppm/$^\circ$C. This further suggests that this material behaves like a rigid-unit mode, where the open structure allows for large thermal movements, and consequently, the "normal" thermal expansion of the SiO_2 molecule does not affect the macroscopic thermal expansion. One could argue that densifying fused silica would hamper these internal motions, in effect the "normal" SiO_2 thermal expansion becomes more prominent. Nevertheless, according to experimental work, this line of thought seems to be untrue. Densification due to fast neutron irradiation leads to a CTE decrease, reported in [249, 250]. In the latter case and our femtosecond laser exposed case, the generation of smaller membered rings (three and four) might disrupt the network, in a way that more open space is created where the large members can fold into and move freely.

The nanograting orientation dependency with the volume variation and CTE is expected to occur, as it does for the longitudinal case, where the volume variation and CTE is higher for nanogratings perpendicularly organized to cantilever long-axis, compared with nanogratings orientated along the cantilever long-axis. It is surprising that this is not obtained for the transverse properties in our results and the ones reported in [90]. An explanation based on shear-lag seems not to hold in this case, as it might be the case for bias between the transverse and longitudinal Young's moduli. This effect is not entirely understood with our current knowledge about this modification.

7.4   Summary

Let us summarize the findings discussed in this chapter:

- It is demonstrated that laser-exposed fused silica induces thermal deformation.

- Evidences are given that the laser-induced athermal strain and CTE difference contribute significantly to the thermal deformation of the bimorph.

- Based on an analytical model and measurements, it has been established that the CTE of fused silica is modified by femtosecond laser irradiation in a notable manner, i.e., typically in the order of factor of 2 for the laser exposure conditions investigated. While densified zones (Regime I) display a decrease of CTE, nanogratings (Regime II) show the opposite trend, with respect to the pristine material.

- The properties in transverse- and axial direction of the athermal volume expansion and

CTE, show distinct behaviors depending on the nanograting orientation.

8 The effect of annealing

Studying the effect of annealing of an unknown material can be a tool to reveal the different structural rearrangements affecting material properties, as they may have distinct quenching thresholds. Apart from understanding the origin of the thermomechanical properties in greater detail, another motivation is more application-oriented. Laser exposure induces both a volume expansion and a CTE change and it seems that they both behave similarly. Meaning, that for an end-user willing to tune the thermal expansion behavior i.e. in a precision device using laser exposure, the athermal position will also be affected. Thermally annealing the material may give an opportunity to circumvent this coupled problem.

In the previous chapter, it became apparent that the thermal deflection of the bimorph structure changes sign by virtue of quenching point defects. In this chapter, we extend the annealing temperature ranging from room-temperature to 900°C. Preliminary results are shown in Figure 8.1; the raw data of the bimorph tip deflections versus the temperature, which corresponds to different annealing conditions. Remarkably, the thermal deflections increase continuously for higher annealing temperatures; for a non-annealed case a slight negative tip deflection rate and for annealing temperatures of 900°C, larger positive tip deflections, reaching 120 nm, are obtained. In Chapter 3 and 7 it is explained that the thermal deflection is a function of the CTE, E, β and ϵ. Most probably, the CTE is affected by the low-temperature annealing step, although in this stage it is not excluded that the other thermomechanical properties are too affected. Furthermore, assumably, for higher annealing temperatures all properties undergo a change. Therefore, we perform a dedicated study to all the material properties discussed so-far in this thesis work, the CTE, ϵ, E and β. The results are discussed first and followed with a discussion, in specifically about the CTE and the volume expansion, ϵ. The latter reveals also some intriguing results.

8.1   Results

The specimens are annealed sequentially at four annealing temperatures, 300, 500, 700 and 900 Celsius degrees, in a nitrogen environment. The duration for each annealing step at the
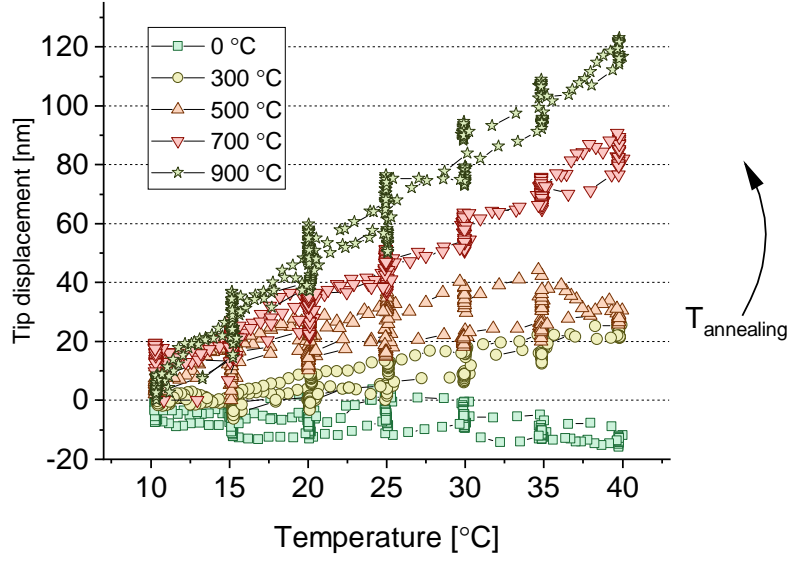
Figure 8.1 – The bimorph's tip-displacement as function of the temperature, for five annealing cases. The exposure conditions are; a pulse energy of 230 nJ, repetition rate of 80 kHz, pulse width of 300 fs, wavelength of 1030 nm, polarizations of 90°, scanning speed 4.2 mm/s (deposited energy of 3.7 J/mm², a N.A. of 0.4 and a line spacing (l_s) of 4 µm.

set-point was 10 hours and the heating-up and cooling-down rate was below 1 °C/min. These conditions are chosen to avoid any transient effects during heating and cooling. The material properties are measured after each annealing step, conducted from the bimorph structure and resonator. First, the elastic properties, athermal and temperature dependent, and second, the CTE and volume expansion, versus the annealing conditions are discussed.

8.1.1 Elastic properties

To study the athermal Young's modulus, the specimens discussed in Chapter 5 are reused. Specifically, the ones regarding a Regime II modification, a polarization 90° and the transverse Young's modulus ($E_{l,0}^{\perp}$), see Figure 5.2. The reference resonators were also measured for each annealing step. No dependency with the annealing steps was observed, for both thermal and athermal properties. The latter measurements gave a standard deviation on f_0 and TCF of <5.02 Hz and <4.18 ppm/°C, respectively.

Figure 8.3 depicts the change of the Young's modulus as a function of the annealing temperature (T_{ann}). The change is with respect to the pristine material for the non-annealed case, meaning that 100% corresponds to the non-annealed case and 0% to the unexposed case. Overall, the laser-induced changes tend to recover for an increasing T_{ann}. For $T_{ann} < 700°C$ the changes are below 2%. At $T_{ann} = 900°C$ the values decayed significantly, towards values of 80%. Remarkably, the low deposited energies exposure, 16 J/mm², decays more sharply. As we see later, a similar effect is observed for the athermal expansion. It seems that the low

deposited energy modifications are less stable.
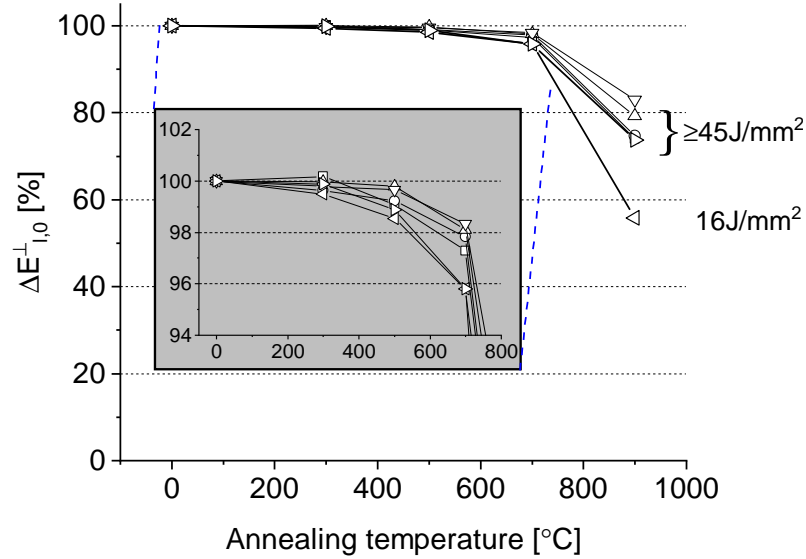
Figure 8.2 – *The change in the LAZ's Young's modulus ($E_{l,0}^{\perp}$) versus the annealing temperature. The change is with respect to the pristine material for the non-annealed case. The inset is the magnified view for the annealing temperature range 0 - 800 °C. The error bar on $\Delta E_{l,0}^{\perp}$ is ±0.128%. The exposure conditions are; pulse energy of 240 nJ, repetition rate of 750 kHz, pulse width of 300 fs, wavelength of 1030 nm, polarization of 90°, a N.A. of 0.4 and a line spacing (l_s) of 4 μm.*

The initial changes in the TCF of the specimens discussed in Figure 8.3 are marginal. Therefore, to study the fine changes due to annealing conditions, we choose a specimen, exposed with a higher exposed volume fraction (V_l). Figure 8.3 depicts the changes versus T_{ann}. The absolute values on measured TCF can be found in Figure 6.7b. The exposure conditions are mentioned in both figure's captions. The error bar is only given for the line spacings (l_s), 1 and 2 μm, for linespacing 3 and 4 μm it exceeds ±20%.

For T_{ann} ≤500 °C, nearly no change is found, although all the values of $\Delta\beta_{l,0}^{\perp}$ are lower compared to the unannealed case. The change corresponds in absolute values typically to 1-2 ppm/°C, which is in the range of the error bar. These minor changes are likely due to the reduction in the CTE, which occurs for these annealing temperatures, as we shall see in the next section in greater detail. At T_{ann} =700°C, β_l starts to return more clearly to the pristine values, except for the one with l_s=4μm. At T_{ann} =900°C, all values are measured above the values corresponding to the pristine case. They all are exceeding the reference value of 109 ppm. Note that the athermal Young's modulus in Figure 8.3 at 900°C did not approach the pristine value. An interpretation of these findings will be given in the discussion.
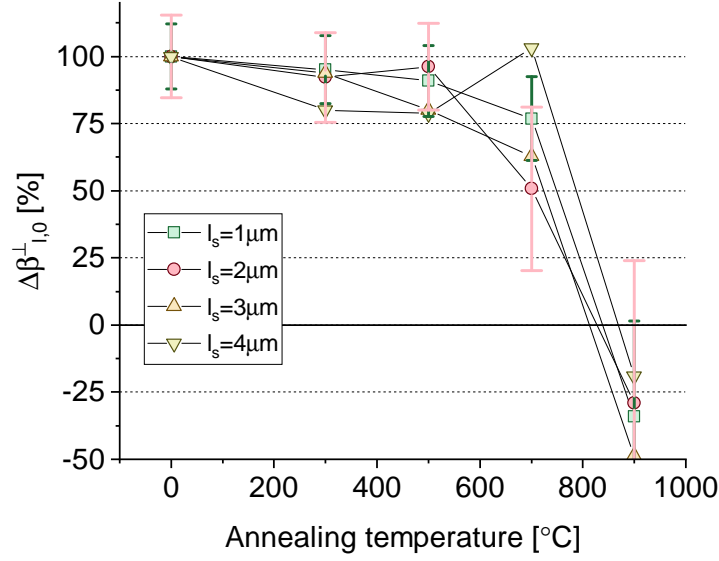
Figure 8.3 – *The change in LAZ's temperature-elastic coefficient ($\beta^\perp_{l,0}$) versus annealing temperatures. The change is with respect to the pristine material for the non-annealed case. The exposure conditions are; pulse energy of 300 nJ, repetition rate of 750 kHz, pulse width of 300 fs, wavelength of 1030 nm, polarization of $0°$, a N.A. of 0.4 and a scanning velocity of 5 mm/s (deposited energy of ~ 40 J/mm^2).*

8.1.2 CTE and athermal volume expansion

For these experiments, we reuse two specimens discussed in Chapter 7. Specifically, the ones with a Regime II modification and polarization of $90°$, depicted in Figure 7.5. The specimens are labeled A and B, and will be mentioned in the figure caption accordingly. The athermal volume expansion changes versus the annealing temperature are shown in Figures 8.4a and b. Figure 8.4a depicts the absolute value of $\epsilon^\perp_0$ versus the deposited energy and figure b depicts the change, with respect to the unannealed case, versus the annealing temperature. For an annealing temperature of $500°$C, there is no significant change observed for ϵ_0. Increasing this annealing temperature to $T_{ann} = 700°$C, two opposite behaviors are observed, a decrease and an increase of 40%, with respect to the initial volume expansion. The decrease is corresponding to deposited energies below 30 J/mm^2, and the increase to deposited energies above 80 J/mm^2. Indeed, higher rate of decay is likewise observed for the Young's modulus at low deposited energies.

Now that the elastic and volume variation values are known, the estimation on the CTE can be made for all the annealing temperatures, shown in Figures 8.4c and d. From room temperature to an annealing temperature T_{ann}=300 °C, a significant decrease is observed. For the low deposited energy cases, ≤30 J/mm^2, the CTE roughly decays by 20%, where a decay of nearly 40% is obtained for the highest deposited energy exposure in this data-set (234 J/mm^2). As no change of this magnitude is obtained for the elastic properties and athermal volume variation, it is therefore evident that the change in sign of the thermal deflection rate, as depicted i.e. in

Figure 8.1, must be accounted to a change in the CTE. From 300°C to 700 °C, a small decay is observed, except at higher deposited energy. Those follow a similar trend as the athermal volume variation - i.e. an increase at 700 °C. At 900 °C, the CTE decays largely towards pristine material properties values.

To confirm these observations, we study another sample with similar exposure conditions, whose results are depicted Figure 8.5. We added additional annealing steps to study the volume expansion increase at 700 °C in finer detail. The exact values are not reconstructed. Nevertheless, the global trend is reproduced, a monotonic decrease for the low deposited energies and an increase of volume expansion at 700 °C for higher deposited energies.
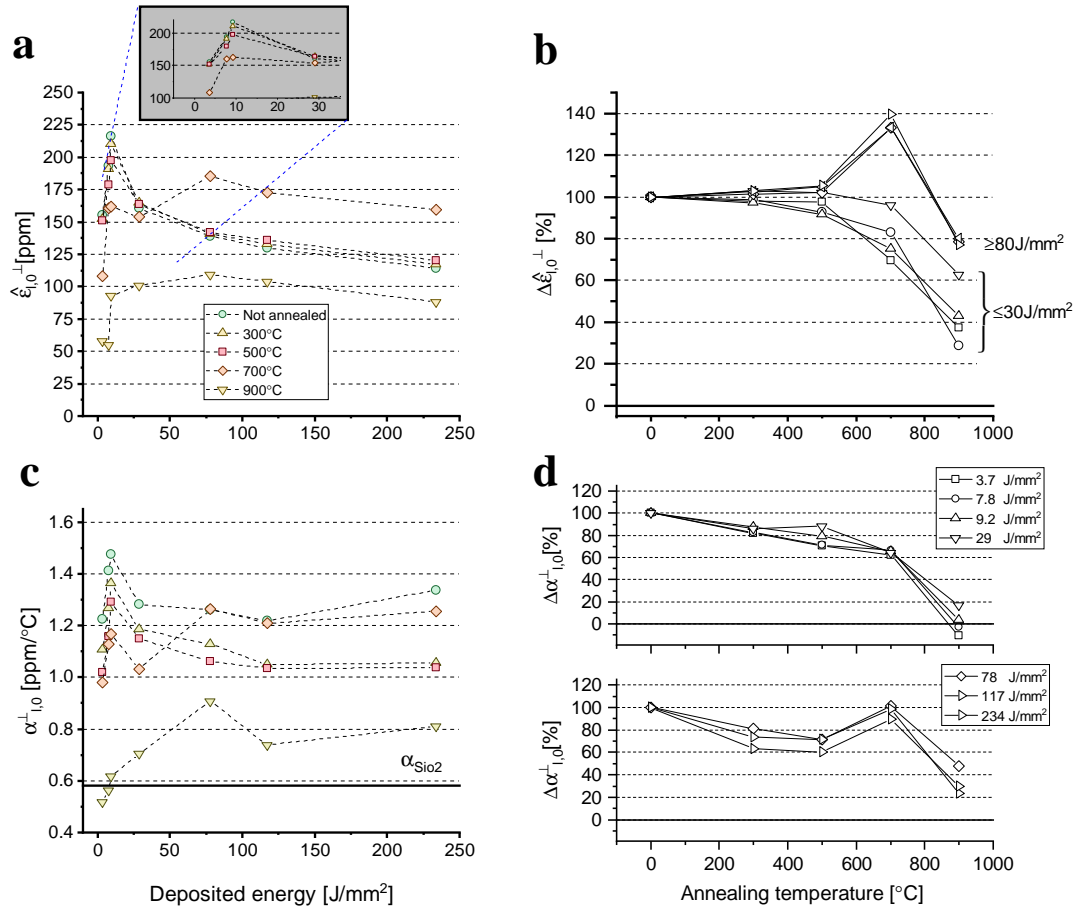
Figure 8.4 – *Sample A: volume expansion ($\hat{\epsilon}_{l,0}^{\perp}$) and CTE ($\alpha_{l,0}^{\perp}$) as function of deposited energy and annealing temperature, up to 900° C. **a**,**c**) depicts the absolute values versus the deposited energy. The inset shows a close-up view of the deposited energy in the range from 0 to 35 J/mm^2 **b**,**d**) shows the changes versus the annealing temperature. Top and bottom figure **d**) illustrates the low- and high-deposited energy ones, respectively. The exposure conditions are; pulse energy of 230 nJ, repetition rate of 80 kHz, pulse width of 300 fs, wavelength of 1030 nm, polarization of 90°, a N.A. of 0.4 and a line spacing (l_s) of 4μm.*
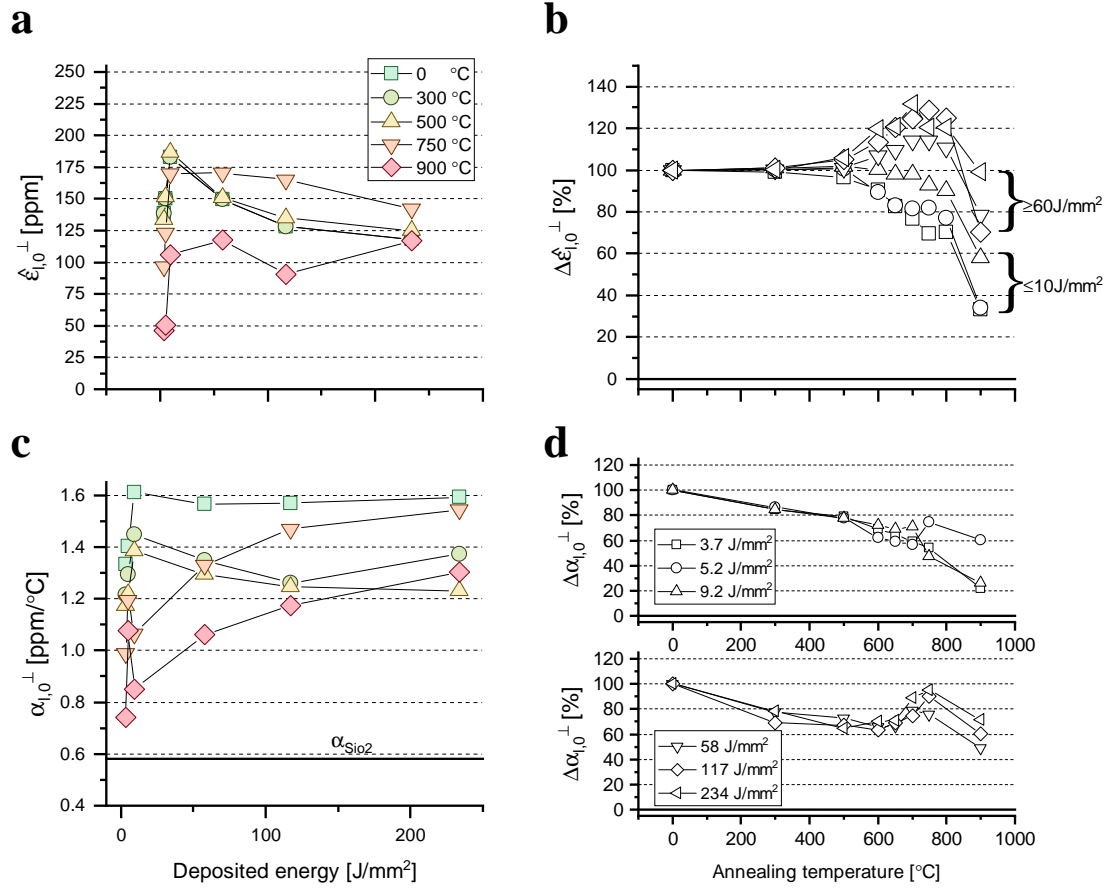
Figure 8.5 – *Sample A: volume expansion ($\hat{\epsilon}_{l,0}^{\perp}$) and CTE ($\alpha_{l,0}^{\perp}$) as function of deposited energy and annealing temperature, up to 900° C. **a,c**) depicts the absolute values versus the deposited energy and **b,d**) depicts the changes versus the annealing temperature. Top and bottom figure **d**) illustrates the low- and high-deposited energies ones, respectively. The exposure conditions are; pulse energy of 230 nJ, repetition rate of 80 kHz, pulse width of 300 fs, wavelength of 1030 nm, polarization of 90°, a N.A. of 0.4 and a line spacing (l_s) of 4 μm.*

8.2 Discussion

The high thermal stability of the nanograting modification was first reported in [88], done by analyzing the birefringence behavior versus annealing treatments. Specifically, the athermal Young's modulus seems to be invariant ($\leq 2\%$) for a broad annealing temperature range, up-to 700°C. Overall, the four other discussed properties respond distinctively upon annealing. The trends regarding high deposited energies ($\geq 30 J/mm^2$) are summarized in Figure 8.6a. To guide the coming discussion, we summarize in Figure 8.6b the laser-induced-defect recovery for different annealing temperatures. We further note that the recovery is not only dependent on the annealing temperature but also on the duration, meaning that certain defects are recovered only after sufficient amount of time. Those events are not necessarily characterized in our work, but it is based on what is found in the literature and in our observations. The references are made in the next discussion.
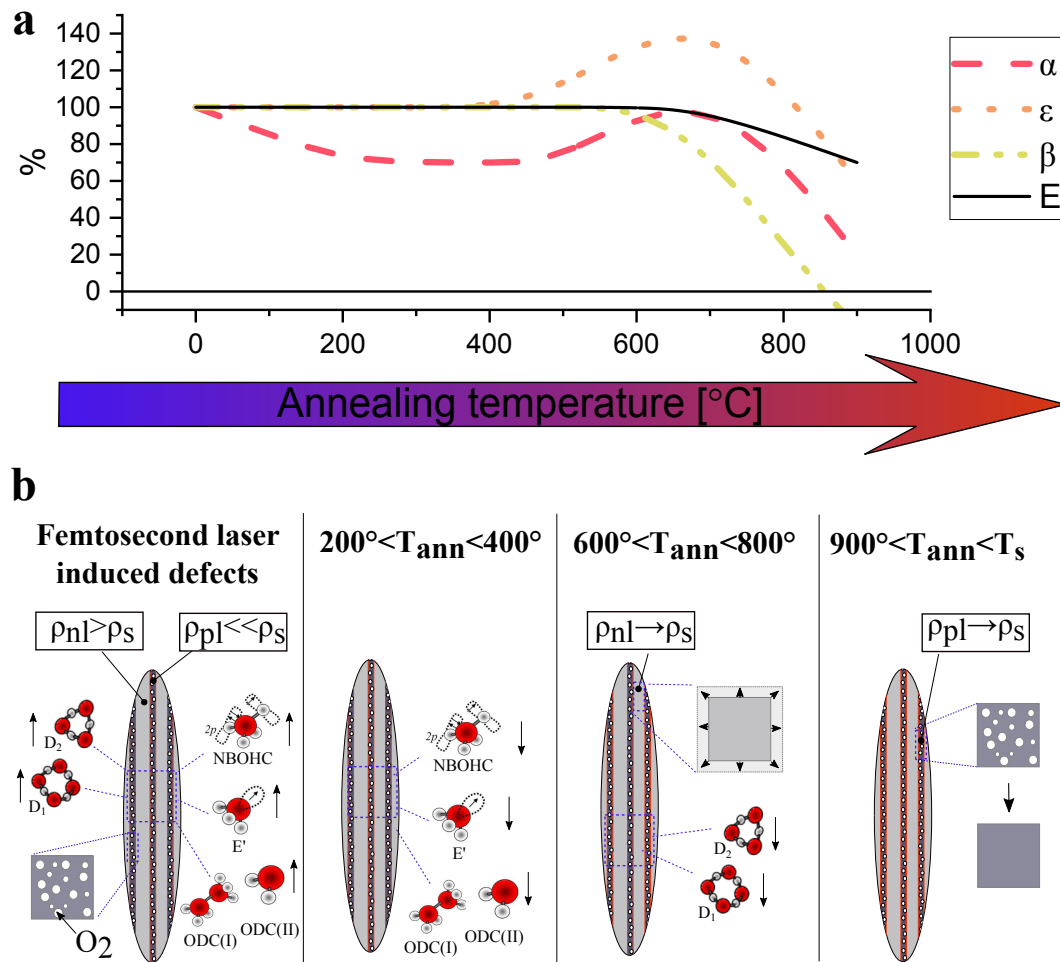
Figure 8.6 – a) *The general trends of the three material properties and volume variation versus the annealing temperature, observed in our experiments.* **b)** *An illustrative summary of laser induced defects and changes for the nanograting modification.* ρ_{nl}, ρ_{pl} *and* ρ_s *are the densities of the non-porous layer, porous layer and pristine substrate, respectively.* T_s *is the softening temperature of the substrate.*

8.2.1   CTE, T_{ann}<300 °C.

For lower annealing temperatures, i.e. T_{ann}<300°C, the change in CTE reduces by nearly 40%. It is known that point-defects are quenched in this temperature range. Irradiation - by neutron, electron, ion, γ-ray, X-ray and laser irradiation- of fused silica leads to the increase of various point-defects and interstitial oxygen [251, 252], in here we review the most common defects induced by laser irradiation.

These point defects can be roughly classified into two categories; oxygen-deficient defects and oxygen-excess defects. The oxygen-deficient defects are E', E'$_\delta$ centers, ODC(I) and ODC(II), where E' and E'$_\delta$ centers are trapped electrons in an oxygen vacancy and the ODC(I) represents a bond between two silicons without a bridging oxygen. One of the possible mechanisms of the aforementioned defects can be due to self-trapped-electrons, created during laser exposure and surviving shortly after. Furthermore, E'center and NBOHC are created by breakage of strained Si-O bonds. The ODC(II) seems to dominate the E'center generation when exceeding a certain energy intensity threshold of the incident laser, as reported by Zoubir *et al.* [253]. We conclude from their description that the energy intensity is related to the one of the Regime I-II transition. This means that the nanograting modification studied in this chapter should contain a considerable amount ODC(II) concentration - which is also observed in [49]. The two common laser induced oxygen-excess defects are non-bridging-oxygen-hole-center (NBOHC) and interstitial oxygen (O_2) or ozone (O_3). The generation of these defects depends on the type of irradiation and the composition of the glass. For instance, hydroxyl groups (OH-content) are the precursors for the generation of NBOHC [254, 253] and of interstitial oxygen [255]. Other mechanisms of the creation of NBOHC are related to pre-strained bonds [256] or plastic deformation [257]. Finally, peroxy-type of bonds, i.e. a peroxy radical (POR) Si-O-O$^\bullet$ are formed by reaction between a E' center and an interstitial oxygen, which is usually stimulated at elevated temperatures.

The quenching behavior of femtosecond laser exposed fused silica and the induced point defects is studied using photoluminescent (PL), absorbtion spectroscopy, electron spin resonance (ESR) and Raman spectroscopy. The production of O_2 and its diluted form is detected, after femtosecond laser exposure, in the Raman spectra [84, 67]. In earlier work, Sun *et al.* studied the magnetic centers with the ESR technique, where the laser induced E'-center and ODC(I) population decayed for annealing temperatures in the range of 25 °C<T_{ann}<400 °C, accompanied with an increase of POR - the latter trend is likewise reported for γ radiation in [258]. They argue that the latter increase is due the recombination of the E' centers and oxygen-excess defects, such as atomic (O) or molecular oxygen (O_2). Therefore, they conclude that interstitial oxygen is quenched in this annealing range [259]. The NBOHC, an oxygen excess defect, is quenched for these annealing temperatures [82], which could mean that the NBOHC and atomic oxygen form POR. Skuja *et al.* argue that the atomic oxygen is generated by destruction of the O_2 (forming $2O^0$), which is the case after neutron bombardment [255]. The atomic oxygen has far higher mobility at these low annealing temperatures than molecular oxygen, therefore it would be a more plausible reaction.

Apart from the works reporting a decrease in the NBOHC population upon annealing [82, 87], other works reported an increase [49, 245]. This could be due the recombination of the E'center and atomic oxygen or due to the rapid cooling these works apply to achieve isothermal annealing conditions, (i.e. 100 °C/min is applied in [245]). It is suggested in these studies that the generation of the NBOHC during the post-annealing step is due the thermal stress. Note, that for these conditions, rapid cooling down, the mismatch in thermal conductivity plays an important role in the generation of thermal stresses [79].

In the experiments discussed in this chapter, it is likely that NBOHC monotonically decrease for T_{ann}<300°C as they react with oxygen-deficient defects recovering the material. We do not expect an increase of NBOHC for higher annealing temperatures, as the cooling down rates are low.

It is suggested that the pores in the porous layers are filled with O_2 [84]. One could imagine that the gaseous oxygen existing in the pores adds a part to the CTE change. To our knowledge there does not exist data on the ultrafast laser generated molecular oxygen evolution versus the annealing temperature, and therefore, we can not infer that the CTE reduction of 40% is due the removal of the gaseous oxygen. Only starting at annealing temperatures of 900°C, and for the applied annealing time, the diffusion length becomes long enough to reach the top surface of the cantilever - for this calculation we choose an activation energy of 29 kCal [260]. Nevertheless, it is possible that the trapped oxygen penetrates the lattice over short distances and forms POR with the E', which would typically occur at 400-500 °C according to [261]. It is hard to assess that this is too the case in our experiment, as the densified material further hinders the mobility of O_2 [262]. To further assimilate the role of trapped gaseous oxygen, an estimate of the thermal pressure change ($\partial P/\partial T$) of the trapped oxygen, see equation 8.1 - derived from the ideal gas law - is compared with the thermal stresses found in the experiments. With n and R as the number of moles and universal gas constant, respectively. V_{pl} is the volume fraction of the porous layer, V_{fp} is the volume fraction of porous in the porous layer and V_{por} is the absolute pore volume.

$$\frac{\partial P}{\partial T} = \frac{nR}{V_{por}} V_{pl} V_{fp} \tag{8.1}$$

The filling factor of the pores, V_{fp}, in the porous layers is roughly 30% [263] and the pore diameters appear in two distinct dimensions, 6 nm or 28 nm [89]. Assuming that these pores are completely filled with oxygen at a pressure of 1bar, the number of moles would be 4.7 x 10^{-22} mol - conducted from the ideal gas law. The trapped oxygen adds roughly 10 Pa/°C to the pressure change inside the laser affected volume. This is roughly four orders lower than the stress changes due CTE difference ($\Delta\alpha E_l$ ~30 kPa/°C). Therefore, it is more likely that the point-defects removal throughout the whole modified volume is responsible for the 40% CTE reduction.

The increase of CTE due to point defects is observed for crystalline materials, such as for silver chloride [264], gold [265] or aluminum [266]. They relate the CTE of a perfect crystal to

the summation of the Grüneisen parameter and Debye temperature of each lattice vibration mode, and add to this the contribution of the point defects. It would be ambiguous to derive for our amorphous material the CTE based on lattice vibrations. Nevertheless in general terms, the vacancies and interstitial would induce phonon scattering, shortening the free mean path of the lattice vibrations [267]. This would not directly mean that the CTE increases, as it does for the decrease of the heat transport due to point defects [268]. Furthermore and intuitively, the scattered waves would not necessarily contribute to the vibration modes. An increase in the CTE is more likely to appear due to the addition of non-linear forces contributing to the increase of anharmonicity.

8.2.2 Athermal volume expansion, 500 $^\circ$C<T_{ann}<700 $^\circ$C.

The increase of the volume expansion, for 500 $^\circ$C< T_{ann} <700 $^\circ$C, is in the first place unexpected as one might expect a recovery of the exposed material at these annealing temperatures. Nevertheless, a similar behavior is obtained for the birefringence in this temperature range, reported in [88, 269]. In [269], the samples are heated-up and cooled-down rapidly to mimic isothermal annealing conditions. They argue that thermal expansion difference, between modified and pristine material, induces additional stress, which remains at room temperature due to the rapid cooling strategy they apply. Bricchi *et al.*, apply similar cooling-down rates as done in this study, 1°C/min. They argue that the porous and non-porous layers exhibit two distinct annealing temperatures, at which the material recovers towards a similar structural arrangement as the pristine material. The latter speculation is in line with our observations we made for the elastic properties. The increase in Young's modulus and decrease in positive temperature-elastic coefficient of the non-porous layer indicate an increase in density (hence a decrease in volume expansion). The increase in volume expansion at 700°C may indicate that the densified layers relax to densities similar to fused silica. The nature of the porous structure indicates that higher activation energies are needed to recover the disrupted structure, whereas for the non-porous layers, a lower energy activation energy is sufficient to reobtain the pristine configuration. Witcher *et al.* and Zhang *et al.* monitored the D_1 and D_2 of thermal annealed femtosecond laser exposed fused silica [82, 270], where typically the population of both defect lines converge to the pristine values for T_{ann}>600°C. Furthermore, the recovery of densified fused silica is likewise observed in this temperature range of 600-800 $^\circ$C [135, 171, 271], using different densification methods. It should be further noted that the recovery in this annealing temperature window is specifically obtained for hot-compressed methods [135], compaction due to thermal quenching [171] or irradiation [271]. Where cold-compressed specimens would show a monotonic recovery, starting from annealing temperatures near room temperature towards the glass transition temperature [272].
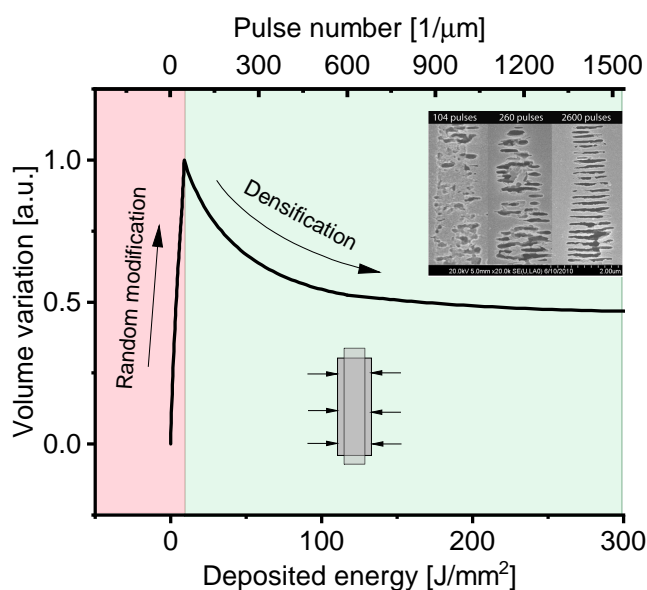
Figure 8.7 *– The volume expansion evolution of the nanogratings versus the deposited energy, adapted from [90]. In the red area, for low deposited energies, the volume expansion is mainly due the porous layers. In the green area, the densification of the non-porous layers reduces the volume expansion. The inset illustrates the evolution of the nanograting modification, adapted from [87].*

The relaxation of the densified zone appears specifically at higher deposited energies. This suggests that the density of non-porous layers evolves as a function of deposited energy and is higher for a higher dose of energy. The evolution of the nanogratings versus the pulse-number (number of pulses per μm) is introduced in Chapter 2. For low pulse-numbers (<100 -/μm) the modification is characterized by a randomly organized porous structure, and the modification organizes gradually for an increasing pulse-number towards a modification with two type of layers, the non- and porous layer [87]. This evolution is depicted in the inset of Figure 8.7. We speculate that the rapid increase of volume expansion for low deposited energies, or pulse-numbers, is due to a porous-dominant character, see Figure 8.7. For deposited energies above ~10-20 J/mm^2, the volume expansion decreases gradually, eventually, resulting in a 50% lower volume-expansion, with respect to the maximum. We further speculate that the latter decrease can be accounted for the density increase of the non-porous layer. Hence, the trend of the volume variation, as depicted Figure 8.7, is a result of two distinct density changes of the non- and porous layer. Ideally, one would like to deduce the densification magnitude of the non-porous layer, however we do not have information about the volume expansion evolution of the porous layer. The pore volume versus the pulse number is investigated using a small angle X-ray scattering method in [89]. For pulse energies of 200 nJ, the pore volume increases steadily when approaching a pulse number of ~1000 -/μm the pore volume is increased by a factor two.

Additionally, this study could tell us more about the compression nature, when indeed assuming that high densities are achieved by hot-compression. Even though the compression imposed by the porous planes from room temperature to the annealing set point is mostly

maintained, the non-porous planes still recover. This suggests that the stationary pressure of the porous planes is not the main driving force for the compaction. Instead; could this mean that the high pressures at the porous plane locations due to the a higher ionization density (see plasma density profile drawn in Figure 5.4 (adapted from [84]), is the driving force for compaction?

8.2.3 Elastic properties, 600 °C<T_{ann}<T_s

The onset for the recovery mechanism of β is closely related to the one of the athermal volume expansion at 700°C, discussed in the previous section. Nevertheless, it is noteworthy to further emphasize the mechanism behind the reduction of the positive temperature-elastic coefficient. In Chapter 6, we deduced from the experiments that the non-porous layer of the nanograting modification is mainly responsible for the decrease of positive temperature-elastic coefficient. We further learned, in the literature review, that densifying fused silica generally leads to a reduction of the positive temperature-elastic coefficient. These findings correlated well with the findings related to the athermal Young's modulus, summarized in Figure 5.4, where we concluded that the non-porous layers are densified, we further speculated that thermal quenching with the assistance of compressive pressures leads to the results we obtained. Once more, the athermal volume expansion at 700°C, discussed in the previous section, may reveal that the nanograting modification contains densified material. The annealing studies of β_l further establish that the reduction may be due to the densified zones and cannot be attributed to the CTE change or to the porous layer. The porous layers are not erased at T_{ann}=900°C and for the applied annealing duration, as athermal Young's modulus is not recovered at this annealing temperature (only by 20%). Therefore, we conclude that the reduction of β_l is due to the densified zones, as no reduction is found at this annealing temperature. Instead, a slight increase of β_l is measured.

8.3 Summary

Studying the effect of thermal annealing on the thermomechanical properties gave us further insights on how certain laser-induced structural rearrangements are related to thermomechanical properties. The key findings presented in this chapter are summarized below. Note that in this study, only nanograting modifications are investigated.

- The athermal Young's modulus remains stable up to annealing temperatures of 700°C, beyond which the measured values are converging back towards the pristine material one.

- The laser-induced CTE reduces by ~40%, when applying annealing temperatures at 300°C. We speculate that the removal of point-defects is responsible for this effect.

- The athermal volume expansion increases by ~40%, at an annealing temperature of

700°C. This could indicate that densified zones, embedded in the nanograting modification, recover at these temperatures. The density of these zones converges to pristine material density values, and therefore, a volume expansion increase is obtained.

- The laser-induced temperature-dependent Young's modulus reduction remains stable up to annealing temperatures of 700°C. At annealing temperatures of 900°C, no reduction is measured. This may point-out that the densified zones is responsible for the temperature-dependent Young's modulus reduction, since for these annealing conditions (annealing temperature and duration), the porous-layers are still present in the material.

- The thermal response of the bimorph is affected by the annealing process, shown in Figure 8.1. This further demonstrates that the thermal response of laser-exposed micromechanical devices can be fine-tuned by a post-annealing step.

A 'visual' summary is proposed in Figure 8.6.

9 Conclusion

In this thesis work, we have experimentally demonstrated that the thermomechanical properties of fused silica are altered upon the action of femtosecond laser irradiation. We believe that this ability of transforming the material in any location of the volume gives nearly unlimited design freedom for defining a landscape with arbitrarily tuned thermomechanical properties with microscale resolution. This result is particularly useful for improving the performance of micrometer-scale precision positioning devices, time references, such as resonators, and optomechanical devices.

The investigation of thermomechanical properties of ultrafast laser-exposed glass is a challenging problem. To capture the main complexity of this problem, it can be best posed as a "coupled multiscale problem". The ultrafast laser exposure of a transparent medium, causes various material property changes at different scales, from the nanoscale up to the macroscopic scale. Consequently, the macroscopic thermomechanical response of the material is dependent on various material properties and structural changes, and differs at different length-scales.

For investigating thermomechanical properties of ultrafast laser-exposed glass, we specifically designed an experimental framework based on micromechanical test devices. Specifically, the thermal expansion behavior was characterized using a bimorph-type of structure, while elastic properties were explored using resonating cantilevers. The temperature of the micromechanical test specimens was controlled by a dedicated environmental chamber, specifically designed for that purpose. In addition, specific mathematical models were implemented, to decipher the thermomechanical response from the micromechanical test specimens as function of material properties.

9.1 Main results

Let us summarize the main results obtained during this thesis work:

1. Thermal expansion coefficient reduction or increase
It has been established that the CTE of fused silica is modified by femtosecond laser irradiation in a notable manner, i.e., typically in the order of factor of 2 for the laser exposure conditions investigated. More interestingly, we have shown that the sign of CTE change depends on the type of laser-induced modifications that is governed by pulse duration and/or the pulse energy. While densified zones (so-called Regime I modification) display a decrease of CTE, nanogratings (Regime II modification) show the opposite trend, with respect to the pristine material. A parametric study to determine the most relevant exposure conditions has been conducted, and shows clearly an evolution of the thermal expansion behavior.

2. Tuning of the Young's modulus
For the homogeneous modification (regime I), a slight increase of the Young's modulus is estimated, approximately 2 GPa. Nanograting modifications are considered to be anisotropic, where the orientation of the anisotropy depends on the orientation of the nanogratings. The Young's modulus is estimated to be slightly stiffer (1 to 2 GPa) along the nanogratings, and more compliant along the orthogonal direction. In the latter direction, the Young's modulus decays exponentially towards values of 35 GPa. Based on the local properties estimation, a mathematical description of the in-plane elastic properties was derived and was experimentally validated for axial and transverse properties. This study effectively demonstrates "laser direct-write nanocomposites" obtained without adding another material, but rather by reorganizing the distribution of matter from the inside, in a controllable way, and according to an arbitrary pattern. These "direct-write" nanocomposites are particularly attractive for novel types of precision resonators and mechanical micro devices with anisotropic and tuned elastic properties.

3. Temperature dependence of laser-tuned Young's modulus
The temperature dependent Young's modulus, known as one of the anomalous material properties of fused silica, shows in both regimes a reduction of the positive temperature-elastic coefficient. As for the athermal Young's modulus in Regime I, reduction of 7% is observed. In regime II, for both nanograting orientations, this modification shows a large decay of the positive temperature-elastic coefficient, approximately within 50%. This result is a preliminary result towards eventually suppressing the thermal dependency of resonators using ultrafast laser irradiation. This thermal stability is for instance desired in seismic sensors or watchmaking.

4. The effect of annealing on thermomechanical properties of laser modified material
A dedicated study was conducted to investigate the effect of annealing on thermomechanical properties in a temperature range from 25 to 900 °C, for the nanograting modification. The Young's modulus displayed a high stability - a change $\leq$ 2% is observed for annealing temperatures 700 °C.

It was revealed that the laser generated point-defects and possibly molecular oxygen contribute to the total CTE change. These contributions account for 20-40%, while we believe that the remaining change is related to structural changes.

At annealing temperatures around 700 °C, the densified zones relaxed towards the pristine configuration, whereas the porous layers remained - this conclusion is made based on the athermal volume expansion.

The laser-induced temperature-dependent Young's modulus reduction remains stable up to annealing temperatures of 700°C. At annealing temperatures of 900°C, no reduction is measured anymore. This may point-out that the densified zones is responsible for the temperature-dependent Young's modulus reduction, since for these annealing conditions, the porous-layers are still present in the material.

These results gave us more insight into the contributions of the different laser-induced material reorganizations. It further demonstrates that the thermomechanical response can be fine-tuned after laser exposure. More interestingly, the thermal deflections of bimorphs were affected without affecting the athermal deflection. This result is potentially useful for applications, which require specific athermal position and fine adjustments in the thermal domain. Most important, this experiment suggests that property changes have a long term stability.

5. New insights related to the nanograting modification

We reported the characterization of local and in-plane elastic properties of femtosecond laser-induced nanogratings in bulk fused silica. The estimation of the values for individual layers is in good agreement with earlier observations of the local refractive index changes. This further confirms that the regions between porous layers, found in the nanograting modification, has similar characteristics as a regime I modification, i.e. a denser structure, with a higher Young's modulus with respect to the pristine material. Interestingly, the estimated elastic properties of this region are significantly higher compared to a regime-I modification. This observation suggests that the densification mechanism of this layer is more complex than the one for regime-I modification. A similar conclusion was made for the thermal dependent Young's modulus. The estimated reduction is remarkably high with respect with other ionizing compaction methods, only hot-compression and fast neutron irradiation have until now shown higher reduction. We make the hypothesis that the compaction of the non-porous layers is similar to the hot-compression method, i.e. the non-porous layers are compressed at elevated temperatures (1000-1500 °C), due to the high pressures generated at the porous layer locations during exposure. Finally, we found evidences of densified zones in the annealing experiments, which is revealed at annealing temperatures of 700 °C. Unfortunately, from this experiment, we could not deduce the high densification we would have expected for a hot-compressed situation.

9.2 Discussion and outlook

A multiscale problem
The local laser affected volume, that itself contains a complex composite structure, is a perfect example of a multiscale problem. In composite type of materials, the macroscopic material properties may be affected by the heterogeneous micro-structure and the morphology of it. For example, the strain-response at the micro-scale upon loading at the macroscopic scale might not be trivial due to subtle differences of material properties at the microscopic scale. Stress is not efficiently transmitted from one constituent to another. Meaning, for instance that the thermal expansion of a particular constituent at the microscopic scale is merely a fraction at the macroscale, and therefore, one should rather speak of "effective" material properties. Complexity rises with the increase in different constituents and the packing ratio [273]. Advanced homogenization and/or multiscale models address these problems [189]. In these modeling schemes, the material properties, which are implemented for each constituent are values, which occur for homogeneous materials at a macroscopic scale. Note that, for our problem the laser affected zone cannot be treated separately from the pristine material, only by approximation, and consequently only the effective properties can be measured. One could retrieve the "real" properties by discriminating it from a volume fraction study, however, with the side note that the laser induced structural changes might be affected for closely exposed volumes (<4 μm). Finally, we like to address that the Poisson's ratio is an important material property for further optimization of the characterization, as the microscopic scale problem cannot be treated as an one dimensional problem.

The transverse expansion behavior and nanograting behavior
For nanograting modifications, we observed a dependence of the nanograting orientations on the thermomechanical properties. However, this dependence is not observed for the transverse athermal volume expansion ($\epsilon_{l,0}^{\perp}$) and the CTE ($\alpha_{l,0}^{\perp}$). The mechanism causing these results is not understood and remains an open-question in this thesis work.

Further study on the anomalous behaviors
Although the question remains whether the origin of the five anomalies of fused silica relate to the same mechanism, it is interesting to study those for ultrafast laser-irradiated specimens. According to our results, we would expect a suppression of the Boson peak in the Raman spectra and the main band would show a smaller blueshift upon a temperature increase. It is hard to predict the effect of the abnormally high internal friction at low-temperatures for the nanograting modifications as the porous layer might induce a higher degree of internal friction. Nevertheless, the excess of vibration modes might be suppressed in the densified locations. These predictions are solely based on the assumption that the anomalies are interrelated and the modification contains densified volumes.

Exploring other glass systems
Studying the thermomechanical properties of other laser-exposed glass formers might give more desired effects for certain applications. For instance, a glass former with a negative

temperature-elastic coefficient might be interesting for thermal actuators, for which typically large motions are desired. We observed in our experiments that the thermal motion due to the positive temperature-elastic coefficient compensates the thermal motion due to the CTE difference. The question remains what the laser affected CTE would be after laser exposure. Another example, vitreous germania has a positive temperature-elastic coefficient [20], although the magnitude is a few factors smaller than fused silica. With the action of laser irradiation, an invariant temperature-elastic coefficient might be more likely achieved. In [274], it is shown that ultrafast laser induced nanogratings are formed in this material.

Towards applications

This work gives an overview on how the thermomechanical properties are tuned versus various exposure conditions. We envision different approaches of tuning the thermomechanical response of microdevices made in glass using laser exposure. For example, for improving the dimensional stability, regime I modifications seems a suitable candidate. However, the improvement would be incremental, as the CTE is reduced by a factor 2. We believe that a system approach is more promising to achieve higher dimensional stability. As an example, a structure with internal degrees-of-freedoms and CTE differences, can be specifically designed to minimize temperature induced length changes, for instance between two points in the material. Another approach could be based on thermally-induced motion caused by initial induced strain and temperature-dependent Young's modulus for compensating the thermally-induced motions due to the CTE of the material. The above mentioned compensation schemes are interesting to implement in applications such as Fabry-Perot cavities and/or on-chip laser cavity, and can be likewise implemented in other precision devices.

A Bimorph stress differentiations

In this annex, we derive a mathematical expression for the stress in the modified layer of the bimorph structure introduced in Chapter 3. To test our model, we designed experiments for which laser-exposure conditions are kept constant, but the filling factor of the exposed volume is varied. The filling factor was tested by changing the line spacing between the individual lines (l_s in Figure 3.1). Additionally, we have preformed these experiments on two wafers, with different wafer thicknesses, 235 μm and 570 μm. The modifications were written using the fiber-laser emitting 250 nJ-pulses and a 300 fs pulse width, at a translation speed of 1.7 mm/s, and a repetition rate of 80 kHz. These exposure conditions correspond to a deposited energy of approximately 10 J/mm^2. It should be noticed that the LAZ length (L_l in Figure 3.1) is 2.4 mm and 4.8 mm for the wafers with a thickness of 235 μm and 570 μm, respectively. Finally, the differentiations are assessed with FEM simulations.
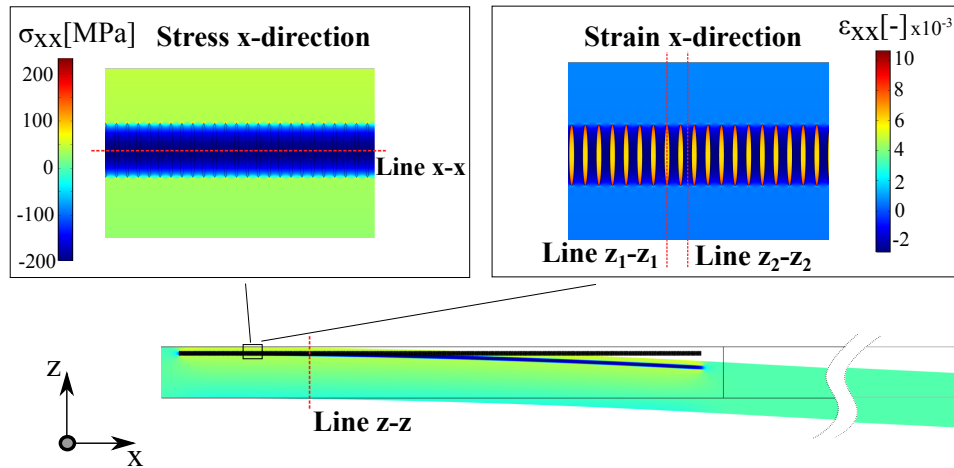
Figure A.1 – *An example of the FEM simulation, with a 4 μm separation between neighboring LAZs and a wafer thickness of 235 μm. The figure at the bottom depicts a stress map of a deflected bimorph's broken-view, with a tip-displacement δ_0. At the top, magnified images of the stress and strain maps of the LAZ region. The red dashed lines represents the Line x-x, z_1-z_1 and z_2-z_2*

Appendix A. Bimorph stress differentiations

For the FEM simulations, the complete bimorph is modeled, as depicted at the bottom of Figure A.1, with a fixed constraint at the anchor, and where the elliptic shapes represents the modified volume. The LAZ's initial volume expansion is applied and iteratively changed, such as the tip-displacement of the cantilever corresponds with the measured tip-displacement. At the top of Figure A.1 magnified images of the stress and strain map, around the LAZ, are given. The stress-map indicates a constant compressive stress throughout the LAZ, and the strain-map indicates a positive strain at the LAZ's location and a negative strain -a compression- in between the LAZ.
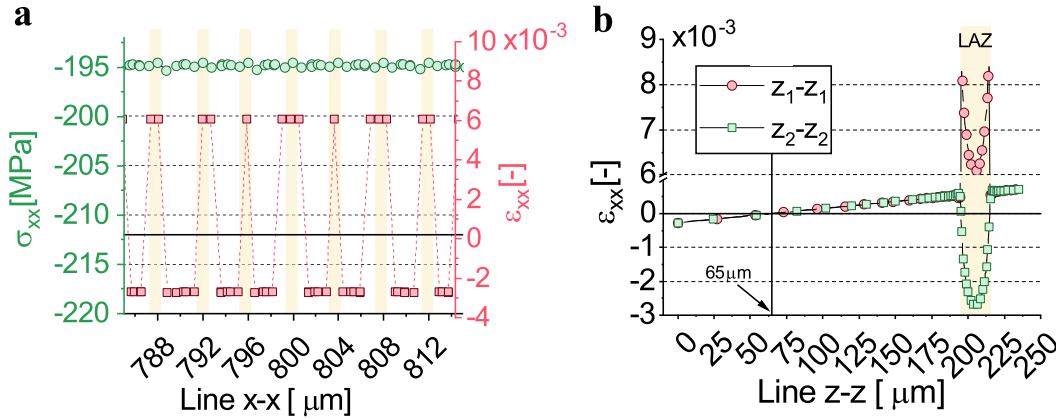
Figure A.2 – a) The simulated strain and stress extracted along the line x-x. The position of the LAZs is indicated by the yellow shaded area. **b)** The linegraphs along the z-axis are located on (z_1-z_1) and in-between the LAZs (z_2-z_2). The neutral-axis is indicated at $t_s/3$, which is in this case at 65 µm.

Figure A.2 depicts the stress and strain along x-direction (σ_{xx} and ϵ_{xx}) from the Line x-x and z-z, which are defined in Figure A.1. Considering Figure A.2a, the compressive stress is also here indicated constant ($\sigma_{xx} \sim$ -195 MPa), and takes into account that the compressive strain in between the LAZs is equal to $\sigma_{xx}/E_{s,0}$. Figure A.2b depicts the lines graphs of ϵ_{xx} from the lines $z_1 - z_1$ and $z_2 - z_2$, which corresponds to a line on and in-between the LAZs, respectively. The neutral axis - i.e. the axis with no stress and strain - is at $t_s/3$ with respect to the bottom of the cantilever, which is expected according to [165] to be the volume expansion of the LAZ and does not represent a pure bending moment, but rather an off-center force - which causes, apart of the bending strain, a spaciously constant strain in x-direction.

The estimated LAZ's average strain ($\hat{\epsilon}_{l,0}$) due to volume expansion by the FEM model and equation 3.1 are depicted in Figure A.3, where we found a satisfying match between the two. For volume fractions ≤0.4, the average strain is proportional to V_l. For higher volume fractions, the volume fraction seems to saturate. The deviation from this proportional relationship at high volume fractions -tight line-spacing- is at this stage interpreted as cross-talk among the lines during the exposure. Finally, it is apparent that $\hat{\epsilon}_{l,0}$ of the thin wafer is roughly twice larger than the thicker (hence stiffer) wafer. Considering the average stress ($\hat{\sigma}_{l,0}$), a large deviation is found for the thin substrate with the Stoney's equation, mentioned in [67, 165], and the FEM simulation, see Figure A.3b. In Stoney's estimation, only a substrate and one

layer is considered, which is not similar to our situation. A layer of non-exposed material is above the LAZ, with a similar thickness, which can be conducted from the graph in Figure A.2. Newton's third law is used to analytical determine LAZ's stress, see equation A.1

$$0 = \frac{\partial \epsilon_{xx}(z)}{\partial z} E_s \left(\int_{-t_s/3}^{0} z \cdot \mathrm{d}z + \int_{0}^{t_s 2/3} z \cdot \mathrm{d}z + \int_{t_s 2/3 + t_l}^{t_s 2/3 + t_l + t_{s,t}} z \cdot \mathrm{d}z \right) + \hat{\sigma}_{l,0} t_l \tag{A.1}$$

The geometrical constant are defined in Figure 3.1. We assume that $\hat{\sigma}_{l,0}$ is spatially constant and we can write for $\epsilon_{xx}(z) = \frac{z}{r_0}$. The LAZ's stress becomes;

$$\hat{\sigma}_{l,0} = -\frac{E_s t_s^2}{6 t_l r_0} - \frac{E_s}{t_l r_0} \left[\frac{1}{2} \left(t_s \frac{2}{3} + t_l + t_{s,t} \right)^2 - \frac{1}{2} \left(\frac{t_s}{3} + t_l \right)^2 \right] \tag{A.2}$$

Note, that the first term is the Stoney's equation. Equation A.2 matches well with the FEM simulation, see Figure A.3.
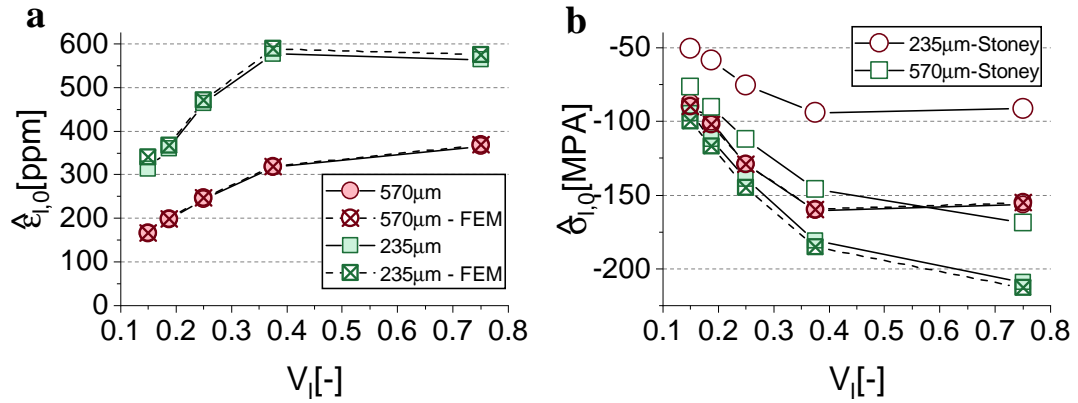
Figure A.3 – *A comparison between the FEM simulation and analytical estimation (equation A.2) on the averaged strain (Figure **a**) and stress (Figure **b**). Additionally in Figure **b** a comparison is made with Stoney's equation.*

Bibliography

[1] *Electronic Materials Handbook: Packaging.* ASM International, Nov. 1989.

[2] A. D. Romig, P. V. Dressendorfer, and D. W. Palmer, "High performance microsystem packaging: A perspective," *Microelectron. Reliab.*, vol. 37, pp. 1771–1781, Oct. 1997.

[3] G. Li and A. A. Tseng, "Low stress packaging of a micromachined accelerometer," *IEEE Trans. Electron. Packag. Manuf.*, vol. 24, pp. 18–25, Jan. 2001.

[4] R. H. Krondorfer and Y. K. Kim, "Packaging effect on MEMS pressure sensor performance," *IEEE Trans. Compon. Packag. Technol.*, vol. 30, pp. 285–293, June 2007.

[5] C. Patel, P. McCluskey, and D. Lemus, "Performance and reliability of mems gyroscopes at high temperatures," in *2010 12th IEEE Intersociety Conference on Thermal and Thermomechanical Phenomena in Electronic Systems*, pp. 1–5, June 2010.

[6] G. Dai, M. Li, X. He, L. Du, B. Shao, and W. Su, "Thermal drift analysis using a multiphysics model of bulk silicon MEMS capacitive accelerometer," *Sens. Actuators A Phys.*, vol. 172, pp. 369–378, Dec. 2011.

[7] B. Xing, B. Zhou, X. Zhang, W. Zhang, B. Hou, Q. Wei, T. Zhang, and R. Zhang, "Thermal deformation suppression chip based on material symmetry design for single center supported MEMS devices," *IEEE Access*, vol. 8, pp. 43314–43324, 2020.

[8] M. Sallusti, P. Gath, D. Weise, M. Berger, and H. R. Schulte, "LISA system design highlights," *Classical Quantum Gravity*, vol. 26, p. 094015, Apr. 2009.

[9] S. G. Turyshev, "The science, technology and mission design for the laser astrometric test of relativity," in *2006 IEEE Aerospace Conference*, p. 16 p., Mar. 2006.

[10] M. Pitkin, S. Reid, S. Rowan, and J. Hough, "Gravitational wave detection by interferometry (ground and space)," *Living Rev. Relativ.*, vol. 14, p. 5, July 2011.

[11] W.-T. Hsu and C. T. C. Nguyen, "Stiffness-compensated temperature-insensitive micromechanical resonators," in *Micro Electro Mechanical Systems, 2002. The Fifteenth IEEE International Conference on*, pp. 731–734, Jan. 2002.

Bibliography

[12] B. Kim, M. A. Hopcroft, R. N. Candler, C. M. Jha, M. Agarwal, R. Melamud, S. A. Chandorkar, G. Yama, and T. W. Kenny, "Temperature dependence of quality factor in MEMS resonators," *J. Microelectromech. Syst.*, vol. 17, pp. 755–766, June 2008.

[13] R. J. Matthys, *Accurate Clock Pendulums*. Great Clarendon Street, Oxford OX2 6DP: Oxford University Press, 2004.

[14] L. R. S. Manuel Blanco, *Advances in Concentrating Solar Thermal Research and Technology*. The Officers'Mess Business Centre, Royston Road, Duxford, CB22 4QH, United Kingdom: Elsevier, 2017.

[15] A. Q. Liu, W. M. Zhu, D. P. Tsai, and N. I. Zheludev, "Micromachined tunable metamaterials: a review," *J. Opt.*, vol. 14, p. 114009, Sept. 2012.

[16] J. Christensen, M. Kadic, O. Kraft, and M. Wegener, "Vibrant times for mechanical metamaterials," *MRS Communications*, vol. 5, pp. 453–462, Sept. 2015.

[17] P. Hofmann, *Solid State Physics An Introduction*. Second edition, Boschstr. 12, 69469 Weinheim,Germany: Wiley-VCH, 2015.

[18] D. A. Padmavathi, "Potential energy curves & material properties," *MSA*, vol. 02, no. 02, pp. 97–104, 2011.

[19] M. R. Vukcevich, "A new interpretation of the anomalous properites of vitreous silica," *Journal of Non-Crystalline Solids*, vol. 11, pp. 25–63, Sept. 1971.

[20] S. Spinner and G. W. Cleek, "Temperature dependence of young's modulus of vitreous germania and silica," *J. Appl. Phys.*, vol. 31, pp. 1407–1410, Aug. 1960.

[21] G. K. White, "Thermal expansion of silica at low temperatures," *Cryogenics*, vol. 4, pp. 2–7, Feb. 1964.

[22] R. B. Roberts, R. J. Tainsh, and G. K. White, "Thermal properties of zerodur at low temperatures," *Cryogenics*, vol. 22, pp. 566–568, Nov. 1982.

[23] K. Takenaka, "Negative thermal expansion materials: technological key for control of thermal expansion," *Sci. Technol. Adv. Mater.*, vol. 13, p. 013001, Feb. 2012.

[24] H. Yamamoto, T. Imai, Y. Sakai, and M. Azuma, "Colossal negative thermal expansion in Electron-Doped PbVO 3 perovskites," *Angew. Chem. Int. Ed.*, vol. 57, pp. 8170–8173, July 2018.

[25] H. Ching and P. H. Ko, "Silicon hairspring," Aug. 2016.

[26] S. M. Aston, M. A. Barton, A. S. Bell, N. Beveridge, B. Bland, A. J. Brummitt, G. Cagnoli, C. A. Cantley, L. Carbone, A. V. Cumming, L. Cunningham, R. M. Cutler, R. J. S. Greenhalgh, G. D. Hammond, K. Haughian, T. M. Hayler, A. Heptonstall, J. Heefner, D. Hoyland, J. Hough, R. Jones, J. S. Kissel, R. Kumar, N. A. Lockerbie, D. Lodhia, I. W. Martin, P. G.

Murray, J. O'Dell, M. V. Plissi, S. Reid, J. Romie, N. A. Robertson, S. Rowan, B. Shapiro, C. C. Speake, K. A. Strain, K. V. Tokmakov, C. Torrie, A. A. van Veggel, A. Vecchio, and I. Wilmut, "Update on quadruple suspension design for advanced LIGO," *Classical Quantum Gravity*, vol. 29, p. 235004, Oct. 2012.

[27] C. J. Bell, S. Reid, J. Faller, G. D. Hammond, J. Hough, I. W. Martin, S. Rowan, and K. V. Tokmakov, "Experimental results for nulling the effective thermal expansion coefficient of fused silica fibres under a static stress," *Classical Quantum Gravity*, vol. 31, p. 065010, Feb. 2014.

[28] G. Cagnoli and P. A. Willems, "Effects of nonlinear thermoelastic damping in highly stressed fibers," *Phys. Rev. B Condens. Matter*, vol. 65, p. 174111, Apr. 2002.

[29] O. Sigmund and S. Torquato, "Design of materials with extreme thermal expansion using a three-phase topology optimization method," *J. Mech. Phys. Solids*, vol. 45, pp. 1037–1067, June 1997.

[30] R. Lakes, "Cellular solids with tunable positive or negative thermal expansion of unbounded magnitude," *Appl. Phys. Lett.*, vol. 90, p. 221905, May 2007.

[31] H. Xu and D. Pasini, "Structurally efficient three-dimensional metamaterials with controllable thermal expansion," *Sci. Rep.*, vol. 6, p. 34924, Oct. 2016.

[32] Q. Wang, J. A. Jackson, Q. Ge, J. B. Hopkins, C. M. Spadaccini, and N. X. Fang, "Lightweight mechanical metamaterials with tunable negative thermal expansion," *Phys. Rev. Lett.*, vol. 117, p. 175901, Oct. 2016.

[33] J. Qu, M. Kadic, A. Naber, and M. Wegener, "Micro-Structured Two-Component 3D metamaterials with negative Thermal-Expansion coefficient from positive constituents," *Sci. Rep.*, vol. 7, p. 40643, Jan. 2017.

[34] B. C. Stuart, M. D. Feit, A. M. Rubenchik, B. W. Shore, and M. D. Perry, "Laser-induced damage in dielectrics with nanosecond to subpicosecond pulses," *Phys. Rev. Lett.*, vol. 74, pp. 2248–2251, Mar. 1995.

[35] E. N. Glezer, M. Milosavljevic, L. Huang, R. J. Finlay, T. H. Her, J. P. Callan, and E. Mazur, "Three-dimensional optical storage inside transparent materials: errata," *Opt. Lett.*, vol. 22, p. 422, Mar. 1997.

[36] K. M. Davis, K. Miura, N. Sugimoto, and K. Hirao, "Writing waveguides in glass with a femtosecond laser," *Opt. Lett.*, vol. 21, pp. 1729–1731, Nov. 1996.

[37] J. D. Mills, P. G. Kazansky, E. Bricchi, and J. J. Baumberg, "Embedded anisotropic microreflectors by femtosecond-laser nanomachining," *Appl. Phys. Lett.*, vol. 81, pp. 196–198, July 2002.

[38] A. Marcinkevičius, S. Juodkazis, M. Watanabe, M. Miwa, S. Matsuo, H. Misawa, and J. Nishii, "Femtosecond laser-assisted three-dimensional microfabrication in silica," *Opt. Lett.*, vol. 26, pp. 277–279, Mar. 2001.

[39] S. Kiyama, S. Matsuo, S. Hashimoto, and Y. Morihira, "Examination of etching agent and etching mechanism on femotosecond laser microfabrication of channels inside vitreous silica substrates," *J. Phys. Chem. C*, vol. 113, pp. 11560–11566, July 2009.

[40] Y. Bellouard, A. Said, M. Dugan, and P. Bado, "Fabrication of high-aspect ratio, micro-fluidic channels and tunnels using femtosecond laser pulses and chemical etching," *Opt. Express*, vol. 12, pp. 2120–2129, May 2004.

[41] C.-E. Athanasiou, M.-O. Hongler, and Y. Bellouard, "Unraveling Brittle-Fracture statistics from intermittent patterns formed during femtosecond laser exposure," *Phys. Rev. Applied*, vol. 8, p. 054013, Nov. 2017.

[42] C.-E. Athanasiou and Y. Bellouard, "A monolithic Micro-Tensile tester for investigating silicon dioxide polymorph micromechanics, fabricated and operated using a femtosecond laser," *Micromachines*, vol. 6, pp. 1365–1386, Sept. 2015.

[43] V. Tielen and Y. Bellouard, "Three-Dimensional glass monolithic Micro-Flexure fabricated by femtosecond laser exposure and chemical etching," *Micromachines*, vol. 5, pp. 697–710, Sept. 2014.

[44] Y. Bellouard, A. Said, M. Dugan, and P. Bado, "Monolithic three-dimensional integration of micro-fluidic channels and optical waveguides in fused silica," *Materials Research Society Symposium*, vol. 782, p. 63–68, 2003.

[45] Felix Sima, Koji Sugioka, Rebeca Martínez Vázquez, Roberto Osellame, Lóránd Kelemen, Pal Ormos, "Three-dimensional femtosecond laser processing for lab-on-a-chip applications," *Nanophotonics*, vol. 7, pp. 613–634, Jan. 2018.

[46] F. Kotz, P. Risch, K. Arnold, S. Sevim, J. Puigmartí-Luis, A. Quick, M. Thiel, A. Hrynevich, P. D. Dalton, D. Helmer, and B. E. Rapp, "Fabrication of arbitrary three-dimensional suspended hollow microstructures in transparent fused silica glass," *Nat. Commun.*, vol. 10, p. 1439, Mar. 2019.

[47] S. I. Nazir and Y. Bellouard, "A monolithic gimbal Micro-Mirror fabricated and remotely tuned with a femtosecond laser," *Micromachines (Basel)*, vol. 10, Sept. 2019.

[48] D. J. Little, M. Ams, P. Dekker, G. D. Marshall, J. M. Dawes, and M. J. Withford, "Femtosecond laser modification of fused silica: the effect of writing polarization on Si-O ring structure," *Opt. Express*, vol. 16, pp. 20029–20037, Nov. 2008.

[49] K. Mishchik, C. D'Amico, P. K. Velpula, C. Mauclair, A. Boukenter, Y. Ouerdane, and R. Stoian, "Ultrafast laser induced electronic and structural modifications in bulk fused silica," *J. Appl. Phys.*, vol. 114, p. 133502, Oct. 2013.

[50] K. Minoshima, A. M. Kowalevicz, I. Hartl, E. P. Ippen, and J. G. Fujimoto, "Photonic device fabrication in glass by use of nonlinear materials processing with a femtosecond laser oscillator," *Opt. Lett., OL*, vol. 26, pp. 1516–1518, Oct. 2001.

[51] A. M. Kowalevicz, V. Sharma, E. P. Ippen, J. G. Fujimoto, and K. Minoshima, "Three-dimensional photonic devices fabricated in glass by use of a femtosecond laser oscillator," *Opt. Lett.*, vol. 30, pp. 1060–1062, May 2005.

[52] J. Liu, Z. Zhang, S. Chang, C. Flueraru, and C. P. Grover, "Directly writing of 1-to-n optical waveguide power splitters in fused silica glass using a femtosecond laser," *Opt. Commun.*, vol. 253, pp. 315–319, Sept. 2005.

[53] R. R. Thomson, T. A. Birks, S. G. Leon-Saval, A. K. Kar, and J. Bland-Hawthorn, "Ultrafast laser inscription of an integrated photonic lantern," *Opt. Express*, vol. 19, pp. 5698–5705, Mar. 2011.

[54] G. D. Marshall, M. Ams, and M. J. Withford, "Direct laser written waveguide-bragg gratings in bulk fused silica," *Opt. Lett.*, vol. 31, pp. 2690–2691, Sep 2006.

[55] K. K. C. Lee, A. Mariampillai, M. Haque, B. A. Standish, V. X. D. Yang, and P. R. Herman, "Temperature-compensated fiber-optic 3D shape sensor based on femtosecond laser direct-written bragg grating waveguides," *Opt. Express*, vol. 21, pp. 24076–24086, Oct. 2013.

[56] G. Bharathan, R. I. Woodward, M. Ams, D. D. Hudson, S. D. Jackson, and A. Fuerbach, "Direct inscription of bragg gratings into coated fluoride fibers for widely tunable and robust mid-infrared lasers," *Opt. Express*, vol. 25, pp. 30013–30019, Nov. 2017.

[57] G. D. Marshall, P. Dekker, M. Ams, J. A. Piper, and M. J. Withford, "Directly written monolithic waveguide laser incorporating a distributed feedback waveguide-bragg grating," *Opt. Lett.*, vol. 33, pp. 956–958, May 2008.

[58] R. G. Krämer, F. Möller, C. Matzdorf, T. A. Goebel, M. Strecker, M. Heck, D. Richter, M. Plötner, T. Schreiber, A. Tünnermann, and S. Nolte, "Extremely robust femtosecond written fiber bragg gratings for an ytterbium-doped fiber oscillator with 5 kw output power," *Opt. Lett.*, vol. 45, pp. 1447–1450, Mar. 2020.

[59] Y. Sikorski, A. A. Said, P. Bado, R. Maynard, C. Florea, and K. A. Winick, "Optical waveguide amplifier in nd-doped glass written with near-IR femtosecond laser pulses," *Electron. Lett.*, vol. 36, pp. 226–227, Feb. 2000.

[60] E. Bricchi, B. G. Klappauf, and P. G. Kazansky, "Form birefringence and negative index change created by femtosecond direct writing in transparent materials," *Opt. Lett.*, vol. 29, pp. 119–121, Jan. 2004.

[61] M. Gecevičius, M. Beresna, J. Zhang, W. Yang, H. Takebe, and P. G. Kazansky, "Extraordinary anisotropy of ultrafast laser writing in glass," *Opt. Express*, vol. 21, pp. 3959–3968, Feb. 2013.

Bibliography

[62] M. Beresna, M. Gecevičius, P. G. Kazansky, and T. Gertus, "Radially polarized optical vortex converter created by femtosecond laser nanostructuring of glass," *Appl. Phys. Lett.*, vol. 98, p. 201101, May 2011.

[63] J. Zhang, M. Gecevičius, M. Beresna, and P. G. Kazansky, "Seemingly unlimited lifetime data storage in nanostructured glass," *Phys. Rev. Lett.*, vol. 112, p. 033901, Jan. 2014.

[64] B. McMillen, C. Athanasiou, and Y. Bellouard, "Femtosecond laser direct-write wave-plates based on stress-induced birefringence," *Opt. Express*, vol. 24, pp. 27239–27252, Nov. 2016.

[65] Y. Bellouard, A. Said, and P. Bado, "Integrating optics and micro-mechanics in a single substrate: a step toward monolithic integration in fused silica," *Opt. Express*, vol. 13, pp. 6635–6644, Aug. 2005.

[66] A. Schaap, Y. Bellouard, and T. Rohrlack, "Optofluidic lab-on-a-chip for rapid algae population screening," *Biomed. Opt. Express*, vol. 2, pp. 658–664, Feb. 2011.

[67] Y. Bellouard, A. Champion, B. McMillen, S. Mukherjee, R. R. Thomson, C. Pépin, P. Gillet, and Y. Cheng, "Stress-state manipulation in fused silica via femtosecond laser irradiation," *Optica*, vol. 3, pp. 1285–1293, Dec. 2016.

[68] F. Chen and J. R. V. de Aldana, "Optical waveguides in crystalline dielectric materials produced by femtosecond-laser micromachining," *Laser Photonics Rev.*, vol. 8, pp. 251–275, May 2014.

[69] J. Tian, H. Yao, M. Cavillon, E. Garcia-Caurel, R. Ossikovski, M. Stchakovsky, C. Eypert, B. Poumellec, and M. Lancry, "A comparison between Nanogratings-Based and Stress-Engineered waveplates written by femtosecond laser in silica," *Micromachines (Basel)*, vol. 11, Jan. 2020.

[70] B. McMillen and Y. Bellouard, "On the anisotropy of stress-distribution induced in glasses and crystals by non-ablative femtosecond laser exposure," *Opt. Express*, vol. 23, pp. 86–100, Jan. 2015.

[71] Y. Bellouard, A. Champion, B. Lenssen, M. Matteucci, A. Schaap, M. Beresna, C. Corbari, M. Gecevicius, P. Kazansky, O. Chappuis, and Others, "The femtoprint project," *J. Laser Micro/Nanoeng.*, vol. 7, no. 1, pp. 1–10, 2012.

[72] R. M. Vazquez, R. Osellame, D. Nolli, C. Dongre, H. van den Vlekkert, R. Ramponi, M. Pollnau, and G. Cerullo, "Integration of femtosecond laser written optical waveguides in a lab-on-chip," *Lab Chip*, vol. 9, pp. 91–96, Jan. 2009.

[73] M. Haque, K. K. C. Lee, S. Ho, L. A. Fernandes, and P. R. Herman, "Chemical-assisted femtosecond laser writing of lab-in-fibers," *Lab Chip*, vol. 14, pp. 3817–3829, Oct. 2014.

[74] C. B. Schaffer, A. Brodeur, J. F. García, and E. Mazur, "Micromachining bulk glass by use of femtosecond laser pulses with nanojoule energy," *Opt. Lett.*, vol. 26, pp. 93–95, Jan. 2001.

[75] A. B. Chris B Schaffer and E. Mazur, "Laser-induced breakdown and damage in bulk transparent materials induced by tightly focused femtosecond laser pulses," *Measurement Science and Technology*, vol. 12, pp. 1784–1794, Oct. 2001.

[76] A. Kaiser, B. Rethfeld, M. Vicanek, and G. Simon, "Microscopic processes in dielectrics under irradiation by subpicosecond laser pulses," *Phys. Rev. B Condens. Matter*, vol. 61, pp. 11437–11450, May 2000.

[77] E. Gamaly, S. Juodkazis, K. Nishimura, H. Misawa, B. Luther-Davies, L. Hallo, P. Nicolai, and V. Tikhonchuk, "Laser-matter interaction in the bulk of a transparent solid: Confined microexplosion and void formation," *Phys. Rev. B Condens. Matter*, vol. 73, p. 214101, June 2006.

[78] N. M. Bulgakova, V. P. Zhukov, S. V. Sonina, and Y. P. Meshcheryakov, "Modification of transparent materials with ultrashort laser pulses: What is energetically and mechanically meaningful?," *J. Appl. Phys.*, vol. 118, p. 233108, Dec. 2015.

[79] Y. Bellouard, E. Barthel, A. A. Said, M. Dugan, and P. Bado, "Scanning thermal microscopy and raman analysis of bulk fused silica exposed to low-energy femtosecond laser pulses," *Opt. Express*, vol. 16, pp. 19520–19534, Nov. 2008.

[80] K. Bergner, B. Seyfarth, K. A. Lammers, T. Ullsperger, S. Döring, M. Heinrich, M. Kumkar, D. Flamm, A. Tünnermann, and S. Nolte, "Spatio-temporal analysis of glass volume processing using ultrashort laser pulses," *Appl. Opt.*, vol. 57, pp. 4618–4632, June 2018.

[81] R. Stoian, K. Mishchik, G. Cheng, C. Mauclair, C. D'Amico, J. P. Colombier, and M. Zamfirescu, "Investigation and control of ultrafast laser-induced isotropic and anisotropic nanoscale-modulated index patterns in bulk fused silica," *Opt. Mater. Express*, vol. 3, p. 1755, Oct. 2013.

[82] J. J. Witcher, W. J. Reichman, L. B. Fletcher, N. W. Troy, and D. M. Krol, "Thermal annealing of femtosecond laser written structures in silica glass," *Opt. Mater. Express.*, vol. 3, pp. 502–510, Mar. 2013.

[83] C. Hnatovsky, R. S. Taylor, P. P. Rajeev, E. Simova, V. R. Bhardwaj, D. M. Rayner, and P. B. Corkum, "Pulse duration dependence of femtosecond-laser-fabricated nanogratings in fused silica," *Appl. Phys. Lett.*, vol. 87, p. 014104, July 2005.

[84] M. Lancry, B. Poumellec, J. Canning, K. Cook, J.-C. Poulin, and F. Brisset, "Ultrafast nanoporous silica formation driven by femtosecond laser irradiation: In the heart of nanogratings," *Laser Photonics Rev.*, vol. 7, pp. 953–962, Nov. 2013.

[85] J. W. Chan, T. Huser, S. Risbud, and D. M. Krol, "Structural changes in fused silica after exposure to focused femtosecond laser pulses," *Opt. Lett.*, vol. 26, pp. 1726–1728, Nov. 2001.

[86] Y. Shimotsuma, P. G. Kazansky, J. Qiu, and K. Hirao, "Self-organized nanogratings in glass irradiated by ultrashort light pulses," *Phys. Rev. Lett.*, vol. 91, p. 247405, Dec. 2003.

[87] S. Richter, M. Heinrich, S. Döring, A. Tünnermann, S. Nolte, and U. Peschel, "Nanogratings in fused silica: Formation, control, and applications," *J. Laser Appl.*, vol. 24, p. 042008, Sept. 2012.

[88] E. Bricchi and P. G. Kazansky, "Extraordinary stability of anisotropic femtosecond direct-written structures embedded in silica glass," *Appl. Phys. Lett.*, vol. 88, p. 111119, Mar. 2006.

[89] S. Richter, A. Plech, M. Steinert, M. Heinrich, S. Döring, F. Zimmermann, U. Peschel, E. B. Kley, A. Tünnermann, and S. Nolte, "On the fundamental structure of femtosecond laser-induced nanogratings," *Laser Photon. Rev.*, vol. 6, pp. 787–792, Nov. 2012.

[90] A. Champion and Y. Bellouard, "Direct volume variation measurements in fused silica specimens exposed to femtosecond laser," *Opt. Mater. Express*, vol. 2, no. 6, p. 789, 2012.

[91] S. Richter, M. Heinrich, S. Döring, A. Tünnermann, and S. Nolte, "Formation of femtosecond laser-induced nanogratings at high repetition rates," *Applied Physics A: Materials Science and Processing*, vol. 104, no. 2, pp. 503–507, 2011.

[92] F. Zimmermann, A. Plech, S. Richter, A. Tünnermann, and S. Nolte, "The onset of ultrashort pulse-induced nanogratings," *Laser Photonics Rev.*, vol. 10, pp. 327–334, Mar. 2016.

[93] S. Richter, F. Jia, M. Heinrich, S. Döring, U. Peschel, A. Tünnermann, and S. Nolte, "The role of self-trapped excitons and defects in the formation of nanogratings in fused silica," *Opt. Lett.*, vol. 37, pp. 482–484, Feb. 2012.

[94] C. Hnatovsky, R. S. Taylor, E. Simova, V. R. Bhardwaj, D. M. Rayner, and P. B. Corkum, "Polarization-selective etching in femtosecond laser-assisted microfluidic channel fabrication in fused silica," *Opt. Lett.*, vol. 30, pp. 1867–1869, July 2005.

[95] M. Beresna, M. Gecevičius, P. G. Kazansky, T. Taylor, and A. V. Kavokin, "Exciton mediated self-organization in glass driven by ultrashort light pulses," *Appl. Phys. Lett.*, vol. 101, p. 053120, July 2012.

[96] Y. Liao, W. Pan, Y. Cui, L. Qiao, Y. Bellouard, K. Sugioka, and Y. Cheng, "Formation of in-volume nanogratings with sub-100-nm periods in glass by femtosecond laser irradiation," *Opt. Lett.*, vol. 40, pp. 3623–3626, Aug. 2015.

[97] R. Buividas, L. Rosa, R. Sliupas, T. Kudrius, G. Slekys, V. Datsyuk, and S. Juodkazis, "Mechanism of fine ripple formation on surfaces of (semi)transparent materials via a half-wavelength cavity feedback," *Nanotechnology*, vol. 22, p. 055304, Feb. 2011.

[98] R. Le Harzic, D. Dörr, D. Sauer, M. Neumeier, M. Epple, H. Zimmermann, and F. Stracke, "Large-area, uniform, high-spatial-frequency ripples generated on silicon using a nanojoule-femtosecond laser at high repetition rate," *Opt. Lett.*, vol. 36, pp. 229–231, Jan. 2011.

[99] Y. Shimotsuma, P. G. Kazansky, J. Qiu, and K. Hirao, "Self-organized nanogratings in glass irradiated by ultrashort light pulses," *Phys. Rev. Lett.*, vol. 91, p. 247405, Dec. 2003.

[100] V. R. Bhardwaj, E. Simova, P. P. Rajeev, C. Hnatovsky, R. S. Taylor, D. M. Rayner, and P. B. Corkum, "Optically produced arrays of planar nanostructures inside fused silica," *Phys. Rev. Lett.*, vol. 96, p. 057404, Feb. 2006.

[101] Y. Liao, Y. Shen, L. Qiao, D. Chen, Y. Cheng, K. Sugioka, and K. Midorikawa, "Femtosecond laser nanostructuring in porous glass with sub-50 nm feature sizes," *Opt. Lett.*, vol. 38, pp. 187–189, Jan. 2013.

[102] A. Rudenko, J.-P. Colombier, and T. E. Itina, "From random inhomogeneities to periodic nanostructures induced in bulk silica by ultrashort laser," *Phys. Rev. B Condens. Matter*, vol. 93, p. 075427, Feb. 2016.

[103] A. Rudenko, J.-P. Colombier, S. Höhm, A. Rosenfeld, J. Krüger, J. Bonse, and T. E. Itina, "Spontaneous periodic ordering on the surface and in the bulk of dielectrics irradiated by ultrafast laser: a shared electromagnetic origin," *Sci. Rep.*, vol. 7, p. 12306, Sept. 2017.

[104] B. Poumellec, M. Lancry, A. Chahid-Erraji, and P. G. Kazansky, "Modification thresholds in femtosecond laser processing of pure silica: review of dependencies on laser parameters [invited]," *Optical materials express*, vol. 1, pp. 766–782, Aug. 2011.

[105] Y. Bellouard and M.-O. Hongler, "Femtosecond-laser generation of self-organized bubble patterns in fused silica," *Opt. Express*, vol. 19, pp. 6807–6821, Mar. 2011.

[106] A. Rudenko, J.-P. Colombier, and T. E. Itina, "Nanopore-mediated ultrashort laser-induced formation and erasure of volume nanogratings in glass," *Phys. Chem. Chem. Phys.*, vol. 20, pp. 5887–5899, Feb. 2018.

[107] E. O. Kissi and Y. Bellouard, "Self-organized nanostructures forming under high-repetition rate femtosecond laser bulk-heating of fused silica," *Opt. Express*, vol. 26, pp. 14024–14037, May 2018.

[108] M. F. Pantano, H. D. Espinosa, and L. Pagnotta, "Mechanical characterization of materials at small length scales," *J. Mech. Sci. Technol.*, vol. 26, pp. 545–561, Feb. 2012.

[109] G. J. McShane, M. Boutchich, A. Srikantha Phani, D. F. Moore, and T. J. Lu, "Young's modulus measurement of thin-film materials using micro-cantilevers," *J. Micromech. Microeng.*, vol. 16, p. 1926, Aug. 2006.

[110] H.-K. Liu, C. H. Pan, and P.-P. Liu, "Dimension effect on mechanical behavior of silicon micro-cantilever beams," *Measurement*, vol. 41, pp. 885–895, Oct. 2008.

[111] J. J. Vlassak and W. D. Nix, "A new bulge test technique for the determination of young's modulus and poisson's ratio of thin films," *J. Mater. Res.*, vol. 7, pp. 3242–3249, Dec. 1992.

[112] M. A. Haque and M. T. A. Saif, "A review of MEMS-based microscale and nanoscale tensile and bending testing," *Exp. Mech.*, vol. 43, pp. 248–255, Sept. 2003.

[113] M. Alfano, L. Pagnotta, and M. F. Pantano, "A review of patented works on the mechanical characterization of materials at micro- and nano-scale," *Recent Pat. Nanotechnol.*, vol. 5, pp. 37–45, Jan. 2011.

[114] M. T. A. Saif and N. C. MacDonald, "Microelectromechanical integrated microloading device," July 1998.

[115] M. Kiuchi, S. Matsui, and Y. Isono, "Mechanical characteristics of FIB deposited carbon nanowires using an electrostatic actuated nano tensile testing device," *J. Microelectromech. Syst.*, vol. 16, pp. 191–201, Apr. 2007.

[116] R. Liu, H. Wang, X. Li, G. Ding, and C. Yang, "A micro-tensile method for measuring mechanical properties of MEMS materials," *J. Micromech. Microeng.*, vol. 18, p. 065002, Apr. 2008.

[117] B. A. Samuel, A. V. Desai, and M. A. Haque, "Design and modeling of a MEMS pico-newton loading/sensing device," *Sens. Actuators A Phys.*, vol. 127, pp. 155–162, Feb. 2006.

[118] T. Tsuchiya, O. Tabata, J. Sakata, and Y. Taga, "Specimen size effect on tensile strength of surface-micromachined polycrystalline silicon thin films," *J. Microelectromech. Syst.*, vol. 7, pp. 106–113, Mar. 1998.

[119] M. A. Haque and M. T. A. Saif, "In-situ tensile testing of nano-scale specimens in SEM and TEM," *Exp. Mech.*, vol. 42, pp. 123–128, Mar. 2002.

[120] I. Chasiotis and W. G. Knauss, "A new microtensile tester for the study of MEMS materials with the aid of atomic force microscopy," *Exp. Mech.*, vol. 42, pp. 51–57, Mar. 2002.

[121] Y. Zhu, N. Moldovan, and D. Horacio, "A microelectromechanical load sensor for in situ electron and x-ray microscopy tensile testing of nanostructures," *Appl. Phys. Lett.*, vol. 86, pp. 013506–013506–3, Dec. 2004.

[122] M. Hardiman, T. J. Vaughan, and C. T. McCarthy, "A review of key developments and pertinent issues in nanoindentation testing of fibre reinforced plastic microstructures," *Compos. Struct.*, vol. 180, pp. 782–798, Nov. 2017.

[123] S.-H. Lee, S. Wang, G. M. Pharr, and H. Xu, "Evaluation of interphase properties in a cellulose fiber-reinforced polypropylene composite by nanoindentation and finite element analysis," *Compos. Part A Appl. Sci. Manuf.*, vol. 38, pp. 1517–1524, June 2007.

[124] A. K. Bhattacharya and W. D. Nix, "Finite element simulation of indentation experiments," *Int. J. Solids Struct.*, vol. 24, pp. 881–891, Jan. 1988.

[125] J. A. M. Mata, "The role of friction on sharp indentation," *Elsevier Journal of the Mechanics and Physics of Solids*, vol. 52, pp. 145–165, May 2003.

[126] C. G. N. Pelletier, J. M. J. Den Toonder, L. E. Govaert, N. Hakiri, and M. Sakai, "Quantitative assessment and prediction of contact area development during spherical tip indentation of glassy polymers," *Philos. Mag.*, vol. 88, pp. 1291–1306, Mar. 2008.

[127] M. A. Mahmoud, "Validity and accuracy of resonance shift prediction formulas for microcantilevers: A review and comparative study," *Crit. Rev. Solid State Mater. Sci.*, vol. 41, pp. 386–429, Sept. 2016.

[128] D. R. França and A. Blouin, "All-optical measurement of in-plane and out-of-plane young's modulus and poisson's ratio in silicon wafers by means of vibration modes," *Meas. Sci. Technol.*, vol. 15, p. 859, Mar. 2004.

[129] M. Alfano and L. Pagnotta, "A non-destructive technique for the elastic characterization of thin isotropic plates," *NDT E Int.*, vol. 40, pp. 112–120, Mar. 2007.

[130] H. Ogi, N. Nakamura, and M. Hirao, "Advanced resonant ultrasound spectroscopy for measuring anisotropic elastic constants of thin films," *Fatigue Fract. Eng. Mater. Struct.*, vol. 28, pp. 657–663, Aug. 2005.

[131] S. Spinner, "Elastic moduli of glasses at elevated temperatures by a dynamic method," *J. Am. Ceram. Soc.*, vol. 39, pp. 113–118, Mar. 1956.

[132] J. W. Marx and J. M. Sivertsen, "Temperature dependence of the elastic moduli and internal friction of silica and glass," *J. Appl. Phys.*, vol. 24, pp. 81–87, Jan. 1953.

[133] T. Deschamps, J. Margueritat, C. Martinet, A. Mermet, and B. Champagnon, "Elastic moduli of permanently densified silica glasses," *Sci. Rep.*, vol. 4, p. 7193, Nov. 2014.

[134] M. Guerette, C. R. Kurkjian, S. Semjonov, and L. Huang, "Nonlinear elasticity of silica glass," *J. Am. Ceram. Soc.*, vol. 99, pp. 841–848, Mar. 2016.

[135] M. Guerette, M. R. Ackerson, J. Thomas, E. B. Watson, and L. Huang, "Thermally induced amorphous to amorphous transition in hot-compressed silica glass," *J. Chem. Phys.*, vol. 148, p. 194501, May 2018.

[136] R. E. Taylor, *Cindas Data series on material properties, Volume I-4 – Thermal expansion of solids*, vol. I-4. ASM International, 1998.

[137] J. D. James, J. A. Spittle, S. G. R. Brown, and R. W. Evans, "A review of measurement techniques for the thermal expansion coefficient of metals andalloys at elevated temperatures," *Iopscience*, pp. R1–R15, 2001.

[138] E37 Committee, "Test method for linear thermal expansion of solid materials with a Push-Rod dilatometer," tech. rep., ASTM International, West Conshohocken, PA, Apr. 2017.

[139] R. Jedamzik, A. Engel, C. Kunisch, G. Westenberger, P. Fischer, and T. Westerhoff, "Next generation dilatometer for highest accuracy thermal expansion measurement of ZERO-DUR®," in *Material Technologies and Applications to Optics, Structures, Components, and Sub-Systems II*, vol. 9574, p. 95740O, International Society for Optics and Photonics, Sept. 2015.

[140] E37 Committee, "Test method for linear thermal expansion of rigid solids with interferometry," tech. rep., ASTM International, West Conshohocken, PA, Apr. 2017.

[141] T. Rubin, H. W. Altman, and H. L. Johnston, "Coefficients of thermal expansion of solids at low temperatures. i. the thermal expansion of copper from 15 to 300°k," *J. Am. Chem. Soc.*, vol. 76, pp. 5289–5293, Nov. 1954.

[142] R. Schödel, "Ultra-high accuracy thermal expansion measurements with PTB's precision interferometer," *Meas. Sci. Technol.*, vol. 19, p. 084003, July 2008.

[143] J. Suska and J. Tschirnich, "An interferometric device for precise thermal expansion measurements on bar-shaped materials," *Meas. Sci. Technol.*, vol. 10, p. N55, Jan. 1999.

[144] M. Okaji, N. Yamada, and H. Moriyama, "Ultra-precise thermal expansion measurements of ceramic and steel gauge blocks with an interferometric dilatometer," *Metrologia*, vol. 37, p. 165, Mar. 2003.

[145] A. Lewis, "Measurement of length, surface form and thermal expansion coefficient of length bars up to 1.5 m using multiple-wavelength phase-stepping interferometry," *Meas. Sci. Technol.*, vol. 5, p. 694, Jan. 1999.

[146] S. J. Bennett, "An absolute interferometric dilatometer," *J. Phys. E*, vol. 10, p. 525, Feb. 2001.

[147] W. A. Plummer and H. E. Hagy, "Precision thermal expansion measurements on low expansion optical materials," *Appl. Opt.*, vol. 7, pp. 825–831, May 1968.

[148] I. Hamann, J. Sanjuan, R. Spannagel, M. Gohlke, G. Wanner, S. Schuster, F. Guzman, and C. Braxmaier, "Laser-dilatometer calibration using a single-crystal silicon sample," *Int. J. Optomechatronics*, vol. 13, pp. 18–29, Jan. 2019.

[149] R. Schödel, A. Walkov, M. Zenker, G. Bartl, R. Meeß, D. Hagedorn, C. Gaiser, G. Thummes, and S. Heltzel, "A new ultra precision interferometer for absolute length measurements down to cryogenic temperatures," *Meas. Sci. Technol.*, vol. 23, p. 094004, July 2012.

[150] T. Middelmann, A. Walkov, G. Bartl, and R. Schödel, "Thermal expansion coefficient of single-crystal silicon from 7 K to 293 K," *Phys. Rev. B Condens. Matter*, vol. 92, p. 174113, Nov. 2015.

[151] J. Varesi and A. Majumdar, "Scanning joule expansion microscopy at nanometer scales," *Appl. Phys. Lett.*, vol. 72, pp. 37–39, Jan. 1998.

[152] Y. Zhang, W. Zhu, F. Hui, M. Lanza, T. Borca-Tasciuc, and M. Muñoz Rojo, "A review on principles and applications of scanning thermal microscopy (SThM)," *Adv. Funct. Mater.*, vol. 30, p. 1900892, May 2020.

[153] Q. Ren, L. Wang, and Q. Huang, "A Micro-Test structure for the thermal expansion coefficient of metal materials," *Micromachines*, vol. 8, p. 70, Feb. 2017.

[154] S. Timoshenko, "Analysis of Bi-Metal thermostats," *J. Opt. Soc. Am.*, vol. 11, no. 3, p. 233, 1925.

[155] C.-L. Cheng, M.-H. Tsai, and W. Fang, "Determining the thermal expansion coefficient of thin films for a CMOS MEMS process using test cantilevers," *J. Micromech. Microeng.*, vol. 25, p. 025014, Jan. 2015.

[156] Y. Y. Hu and W. M. Huang, "Thermal stress analysis and characterization of thermomechanical properties of thin films on an elastic substrate," in *Handbook of Manufacturing Engineering and Technology* (A. Nee, ed.), pp. 1–71, London: Springer London, 2013.

[157] W. C. Young and R. G. Budynas, *Roark's formulas for stress and strain.* 7th ed., McGraw-Hill, 2002.

[158] K. K. Chawla, *Composite Materials.* 3rd Edition, Springer, 2012.

[159] P. Vlugter, E. Block, and Y. Bellouard, "Local tuning of fused silica thermal expansion coefficient using femtosecond laser," *Phys. Rev. Materials*, vol. 3, p. 053802, May 2019.

[160] P. Vlugter and Y. Bellouard, "Elastic properties of self-organized nanogratings produced by femtosecond laser exposure of fused silica," *Phys. Rev. Materials*, vol. 4, p. 023607, Feb. 2020.

[161] M. Benabdi and A. A. Roche, "Mechanical properties of thin and thick coatings applied to various substrates. part i. an elastic analysis of residual stresses within coating materials," *J. Adhes. Sci. Technol.*, vol. 11, pp. 281–299, Jan. 1997.

[162] W. C. Young and R. G. Budynas, *Roark's formulas for stress and strain.* 7th ed., McGraw-Hill, 2002.

[163] M. Christophersen, B. Shapiro, and E. Smela, "Characterization and modeling of PPy bilayer microactuators: Part 1. curvature," *Sens. Actuators B Chem.*, vol. 115, pp. 596–609, June 2006.

[164] Y. Bao and G. Chen, "Temperature-dependent strain and temperature sensitivities of fused silica single mode fiber sensors with pulse pre-pump brillouin optical time domain analysis," *Meas. Sci. Technol.*, vol. 27, p. 065101, Apr. 2016.

[165] C.-H. Hsueh, "Modeling of elastic deformation of multilayers due to residual stresses and external bending," *Appl. Phy.*, vol. 91, pp. 9652–9656, Mar. 2002.

[166] Y. Bellouard, T. Colomb, C. Depeursinge, M. Dugan, A. A. Said, and P. Bado, "Nanoindentation and birefringence measurements on fused silica specimen exposed to low-energy femtosecond pulses," *Opt. Express*, vol. 14, pp. 8360–8366, Sept. 2006.

[167] J. M. Rimsza and J. Du, "Structural and mechanical properties of nanoporous silica," *J. Am. Ceram. Soc.*, vol. 97, pp. 772–781, Mar. 2014.

[168] T. Adachi and S. Sakka, "Dependence of the elastic moduli of porous silica gel prepared by the sol-gel method on heat-treatment," *J. Mater. Sci.*, vol. 25, pp. 4732–4737, Nov. 1990.

[169] K. Mishchik, G. Cheng, G. Huo, I. M. Burakov, C. Mauclair, A. Mermillod-Blondin, A. Rosenfeld, Y. Ouerdane, A. Boukenter, O. Parriaux, and R. Stoian, "Nanosize structural modifications with polarization functions in ultrafast laser irradiated bulk fused silica," *Opt. Express*, vol. 14, pp. 3785–3791, Nov. 2006.

[170] J. Hernandez-Rueda, J. Clarijs, D. van Oosten, and D. M. Krol, "The influence of femtosecond laser wavelength on waveguide fabrication inside fused silica," *Appl. Phys. Lett.*, vol. 110, p. 161109, Apr. 2017.

[171] R. Bruckner, "Properties and structure of vitreous silica. i," *J. Non-Cryst. Solids*, vol. 5, pp. 123–175, 1970.

[172] W. Primak, "Mechanism for the radiation compaction of vitreous silica," *J. Appl. Phys.*, vol. 43, pp. 2745–2754, June 1972.

[173] A. Saliminia, N. T. Nguyen, S. L. Chin, and R. Vallée, "Densification of silica glass induced by 0.8 and 1.5μm intense femtosecond laser pulses," *J. Appl. Phys.*, vol. 99, p. 093104, May 2006.

[174] M. Guerette, M. R. Ackerson, J. Thomas, F. Yuan, E. Bruce Watson, D. Walker, and L. Huang, "Structure and properties of silica glass densified in cold compression and hot compression," *Sci. Rep.*, vol. 5, p. 15343, Oct. 2015.

[175] R. Le Parc, C. Levelut, J. Pelous, V. Martinez, and B. Champagnon, "Influence of fictive temperature and composition of silica glass on anomalous elasticbehaviour," *J. Phys. Condens. Matter*, vol. 18, p. 7507, July 2006.

[176] H. Kakiuchida, K. Saito, and A. J. Ikushima, "Refractive index, density and polarizability of silica glass with various fictive temperatures," *Jpn. J. Appl. Phys.*, vol. 43, p. L743, May 2004.

[177] U. Haken, O. Humbach, S. Ortner, and H. Fabian, "Refractive index of silica glass: influence of fictive temperature," *J. Non-Cryst. Solids*, vol. 265, pp. 9–18, Mar. 2000.

[178] C. Z. Tan, J. Arndt, and H. S. Xie, "Optical properties of densifed silica glasses," *Phys. B*, vol. 252, pp. 28–33, 1998.

[179] A. Champion, M. Beresna, P. Kazansky, and Y. Bellouard, "Stress distribution around femtosecond laser affected zones: effect of nanogratings orientation," *Opt. Express*, vol. 21, pp. 24942–24951, Oct. 2013.

[180] P. F. McMillan, M. Wilson, M. C. Wilding, D. Daisenberger, M. Mezouar, and G. Neville Greaves, "Polyamorphism and liquid–liquid phase transitions: challenges for experiment and theory*," *J. Phys. Condens. Matter*, vol. 19, p. 415101, Sept. 2007.

[181] M. Grimsditch, "Polymorphism in amorphous SiO_2," *Phys. Rev. Lett.*, vol. 52, pp. 2379–2381, June 1984.

[182] J. C. Mauro, R. J. Loucks, and P. K. Gupta, "Fictive temperature and the glassy state," *J. Am. Ceram. Soc.*, vol. 92, pp. 75–86, Jan. 2009.

[183] P. K. Gupta, "Fictive pressure effects in structural relaxation," *J. Non-Cryst. Solids*, vol. 102, pp. 231–239, June 1988.

[184] A. K. Varshneya, E. D. Zanotto, and J. C. Mauro, "Perspectives on the scientific career and impact of prabhat k. gupta," *Journal of Non-Crystalline Solids: X*, vol. 1, p. 100011, Mar. 2019.

[185] G.-Z. Kang and Q. Gao, "Tensile properties of randomly oriented shortd-Al2O3®ber re-inforcedaluminum alloy composites: II. finite element analysis for stress transfer,elastic modulus and stress±strain curve," *Elsevier composites: Part A*, vol. 33, pp. 657–667, Jan. 2002.

[186] S. Ahmed and F. R. Jones, "A review of particulate reinforcement theories for polymer composites," *J. Mater. Sci.*, vol. 25, pp. 4933–4942, Dec. 1990.

[187] H. L. Cox, "The elasticity and strength of paper and other fibrous materials," *Br. J. Appl. Phys.*, vol. 3, p. 72, Mar. 1952.

[188] J. D. Eshelby and R. E. Peierls, "The determination of the elastic field of an ellipsoidal inclusion, and related problems," *Proc. R. Soc. Lond. A Math. Phys. Sci.*, vol. 241, pp. 376–396, Aug. 1957.

[189] P. Kanouté, D. P. Boso, J. L. Chaboche, and B. A. Schrefler, "Multiscale methods for composites: A review," vol. 16, pp. 31–75, Mar. 2009.

Bibliography

[190] C. L. Babcock, S. W. Barber, and K. Fajans, "Coexisting structures in vitreous silica," *Ind. Eng. Chem.*, vol. 46, pp. 161–166, Jan. 1954.

[191] L. Huang, L. Duffrène, and J. Kieffer, "Structural transitions in silica glass: Thermo-mechanical anomalies and polyamorphism," *Glass Science for High Technology. 16th University Conference*, vol. 349, no. 1-3, pp. 1–9, 2004.

[192] T. Nakayama, "Boson peak and terahertz frequency dynamics of vitreous silica," *Rep. Prog. Phys.*, vol. 65, p. 1195, July 2002.

[193] P. W. Bridgman, "Compressibility of glasses," . *Am.J.Sci.*, vol. 10, 1925.

[194] R. C. Zeller and R. O. Pohl, "Thermal conductivity and specific heat of noncrystalline solids," *Phys. Rev. B Condens. Matter*, vol. 4, pp. 2029–2041, Sept. 1971.

[195] D. F. Gibbons, "On the thermal expansion and grüneisen factor of vitreous silica," *J. Phys. Chem. Solids*, vol. 11, pp. 246–248, Oct. 1959.

[196] G. K. White, "Thermal expansion at low temperatures of glass-ceramics and glasses," *Cryogenics*, vol. 16, pp. 487–490, Aug. 1976.

[197] B. Rufflé, S. Ayrinhac, E. Courtens, R. Vacher, M. Foret, A. Wischnewski, and U. Buchenau, "Scaling the temperature-dependent boson peak of vitreous silica with the high-frequency bulk modulus derived from brillouin scattering data," *Phys. Rev. Lett.*, vol. 104, p. 067402, Feb. 2010.

[198] W. H. Zachariasen, "The atomic arrangement in glass," *J. Am. Chem. Soc.*, vol. 54, pp. 3841–3851, Oct. 1932.

[199] Mozzi R. L. and Warren B. E., "Structure of vitreous silica," *J. Appl. Crystallogr.*, vol. 2, no. pt 4, pp. 164–172, 1969.

[200] J. P. Rino, I. Ebbsjö, I, R. K. Kalia, A. Nakano, and P. Vashishta, "Structure of rings in vitreous SiO$_2$," *Phys. Rev. B Condens. Matter*, vol. 47, pp. 3053–3062, Feb. 1993.

[201] A. C. Wright, "Neutron scattering from vitreous silica. v. the structure of vitreous silica: What have we learned from 60 years of diffraction studies?," *J. Non-Cryst. Solids*, vol. 179, pp. 84–115, Nov. 1994.

[202] D. Uhlmann, *Elasticity and Strength in Glasses: Glass: Science and Technology.* Elsevier, Dec. 2012.

[203] J. T. Krause and C. R. Kurkjian, "Vibrational anomalies in inorganic glass formers," *J. Am. Ceram. Soc.*, vol. 51, pp. 226–227, Apr. 1968.

[204] Harold T. Smyth, Haven S. Skogen, and William B. Harsell, "Thermal capacity of vitreous silica," *Journal of The American Ceramic Society*, vol. 36, no. 10, pp. 327–328, 1953.

[205] O. L. Anderson and H. E. Bommel, "Ultrasonic absorption in fused silica at low temperatures and high frequencies," *J. Am. Ceram. Soc.*, vol. 38, pp. 125–131, Apr. 1955.

[206] B. E. Warren and J. Biscce, "The structure of silica glass by x-ray differaction studies," *J. Am. Ceram. Soc.*, vol. 21, pp. 49–54, Feb. 1938.

[207] A. Pasquarello and R. Car, "Identification of raman defect lines as signatures of ring structures in vitreous silica," *Phys. Rev. Lett.*, vol. 80, pp. 5145–5147, June 1998.

[208] O. L. Anderson, "The debye temperature of vitreous silica," *J. Phys. Chem. Solids*, vol. 12, pp. 41–52, Dec. 1959.

[209] L. Huang and J. Kieffer, "Amorphous-amorphous transitions in silica glass. II. irreversible transitions and densification limit," *Phys. Rev. B Condens. Matter*, vol. 69, p. 224204, June 2004.

[210] Y. Shi, J. Neuefeind, D. Ma, K. Page, L. A. Lamberson, N. J. Smith, A. Tandia, and A. P. Song, "Ring size distribution in silicate glasses revealed by neutron scattering first sharp diffraction peak analysis," *J. Non-Cryst. Solids*, vol. 516, pp. 71–81, July 2019.

[211] V. N. Sigaev, E. N. Smelyanskaya, V. G. Plotnichenko, V. V. Koltashev, A. A. Volkov, and P. Pernice, "Low-frequency band at 50 cm^{-}1 in the raman spectrum of cristobalite: identification of similar structural motifs in glasses and crystals of similar composition," *J. Non-Cryst. Solids*, vol. 248, pp. 141–146, June 1999.

[212] M. Handke and W. Mozgawa, "Vibrational spectroscopy of the amorphous silicates," *Vib. Spectrosc.*, vol. 5, pp. 75–84, Apr. 1993.

[213] S. V. King, "Ring configurations in a random network model of vitreous silica," *Nature*, vol. 213, pp. 1112–1113, Mar. 1967.

[214] R. J. Bell and P. Dean, "Properties of vitreous silica: Analysis of random network models," *Nature*, vol. 212, pp. 1354–1356, Dec. 1966.

[215] F. L. Galeener, "Planar rings in glasses," *Solid State Commun.*, vol. 44, pp. 1037–1040, Nov. 1982.

[216] L. Huang and J. Kieffer, "Amorphous-amorphous transitions in silica glass. i. reversible transitions and thermomechanical anomalies," *Phys. Rev. B Condens. Matter*, vol. 69, p. 224203, June 2004.

[217] L. Huang, F. Yuan, M. Guerette, Q. Zhao, and S. Sundararaman, "Tailoring structure and properties of silica glass aided by computer simulation," *J. Mater. Res.*, vol. 32, pp. 174–182, Jan. 2017.

[218] L. Huang and J. Kieffer, "Structural origin of negative thermal expansion in high-temperature silica polymorphs," *Phys. Rev. Lett.*, vol. 95, p. 215901, Nov. 2005.

Bibliography

[219] R. J. Hemley, H. K. Mao, P. M. Bell, and B. O. Mysen, "Raman spectroscopy of SiO2 glass at high pressure," *Phys. Rev. Lett.*, vol. 57, pp. 747–750, Aug. 1986.

[220] T. Deschamps, C. Martinet, D. R. Neuville, D. de Ligny, C. Coussa-Simon, and B. Champagnon, "Silica under hydrostatic pressure: A non continuous medium behavior," *J. Non-Cryst. Solids*, vol. 355, pp. 2422–2424, Nov. 2009.

[221] B. Champagnon, L. Wondraczek, and T. Deschamps, "Boson peak, structural inhomogeneity, light scattering and transparency of silicate glasses," *J. Non-Cryst. Solids*, vol. 355, pp. 712–714, May 2009.

[222] T. Sato and N. Funamori, "Sixfold-coordinated amorphous polymorph of SiO2 under high pressure," *Phys. Rev. Lett.*, vol. 101, p. 255502, Dec. 2008.

[223] Y. Inamura, M. Arai, M. Nakamura, T. Otomo, N. Kitamura, S. M. Bennington, A. C. Hannon, and U. Buchenau, "Intermediate range structure and low-energy dynamics of densified vitreous silica," *J. Non-Cryst. Solids*, vol. 293-295, pp. 389–393, Nov. 2001.

[224] C. Weigel, M. Mebarki, S. Clément, R. Vacher, M. Foret, and B. Rufflé, "Pressure-induced densification of vitreous silica: Insight from elastic properties," *Phys. Rev. B Condens. Matter*, vol. 100, p. 094102, Sept. 2019.

[225] C. Martinet, A. Kassir-Bodon, T. Deschamps, A. Cornet, S. Le Floch, V. Martinez, and B. Champagnon, "Permanently densified SiO2 glasses: a structural approach," *J. Phys. Condens. Matter*, vol. 27, p. 325401, Aug. 2015.

[226] F. S. El'kin, V. V. Brazhkin, L. G. Khvostantsev, O. B. Tsiok, and A. G. Lyapin, "In situ study of the mechanism of formation of pressure-densified sio2 glasses," *Journal of Experimental and Theoretical Physics Letters*, vol. 75, pp. 342–347, Apr. 2002.

[227] C. Martinet, M. Heili, V. Martinez, G. Kermouche, G. Molnar, N. Shcheblanov, E. Barthel, and A. Tanguy, "Highlighting the impact of shear strain on the SiO2 glass structure: From experiments to atomistic simulations," *J. Non-Cryst. Solids*, vol. 533, p. 119898, Apr. 2020.

[228] M. Heili, B. Poumellec, E. Burov, C. Gonnet, C. Le Losq, D. R. Neuville, and M. Lancry, "The dependence of raman defect bands in silica glasses on densification revisited," *J. Mater. Sci.*, vol. 51, pp. 1659–1666, Feb. 2016.

[229] A. Cornet, V. Martinez, D. de Ligny, B. Champagnon, and C. Martinet, "Relaxation processes of densified silica glass," *J. Chem. Phys.*, vol. 146, p. 094504, Mar. 2017.

[230] I. Reghioua, M. Lancry, O. Cavani, S. L. Floch, D. R. Neuville, and N. Ollier, "Unique silica polymorph obtained under electron irradiation," *Appl. Phys. Lett.*, vol. 115, p. 251101, Dec. 2019.

[231] S. Kapoor, L. Wondraczek, and M. M. Smedskjaer, "Pressure-induced densification of oxide glasses at the glass transition," *Frontiers in Materials*, vol. 4, p. 1, Feb. 2017.

[232] M. Tomozawa, J.-W. Hong, and S.-R. Ryu, "Infrared (IR) investigation of the structural changes of silica glasses with fictive temperature," *J. Non-Cryst. Solids*, vol. 351, pp. 1054–1060, May 2005.

[233] D. B. Fraser, "Factors influencing the acoustic properties of vitreous silica," *J. Appl. Phys.*, vol. 39, pp. 5868–5878, Dec. 1968.

[234] R. E. Strakna, "Investigation of Low-Temperature ultrasonic absorption in Fast-Neutron irradiated SiO_2 glass," *Phys. Rev.*, vol. 123, pp. 2020–2026, Sept. 1961.

[235] R. E. Strakna, A. E. Clark, D.L. Bradley, and W. M. Slie, "Effect of Fast-Neutron irradiation on the pressure and temperature dependence of the elastic moduli of SiO2 glass," *J. Appl. Phys.*, vol. 34, May 1963.

[236] R. H. Stolen, J. T. Krause, and C. R. Kurkjian, "Raman scattering and far infra-red absorption in neutron compacted silica," *Discuss. Faraday Soc.*, vol. 50, pp. 103–107, Jan. 1970.

[237] R. A. B. Devine, "Macroscopic and microscopic effects of radiation in amorphous SiO2," *Nucl. Instrum. Methods Phys. Res. B*, vol. 91, pp. 378–390, June 1994.

[238] J. C. King, "The anelasticity of natural and synthetic quartz at low temperatures," *The bell system technical journal*, 1959.

[239] M. K. Rabia, S. Degioanni, C. Martinet, J. Le Brusq, B. Champagnon, and D. Vouagner, "A-thermal elastic behavior of silicate glasses," *J. Phys. Condens. Matter*, vol. 28, p. 075402, Feb. 2016.

[240] S. P. Jaccani, S. Sundararaman, and L. Huang, "Understanding the structural origin of intermediate glasses," *J. Am. Ceram. Soc.*, vol. 102, pp. 1137–1149, Mar. 2019.

[241] V. G. Karpov and M. Grimsditch, "Pressure-induced transformations in glasses," *Phys. Rev. B Condens. Matter*, vol. 48, pp. 6941–6948, Sept. 1993.

[242] N. S. Shcheblanov, M. E. Povarnitsyn, K. N. Mishchik, and A. Tanguy, "Raman spectroscopy of femtosecond multipulse irradiation of vitreous silica: Experiment and simulation," *Phys. Rev. B Condens. Matter*, vol. 97, p. 054106, Feb. 2018.

[243] S. Vukelić, P. Kongsuwan, S. Ryu, and Y. L. Yao, "Ultrafast laser induced structural modification of fused Silica—Part II: Spatially resolved and decomposed raman spectral analysis," *J. Manuf. Sci. Eng.*, vol. 132, Dec. 2010.

[244] J. W. Chan, T. R. Huser, S. H. Risbud, and D. M. Krol, "Modification of the fused silica glass network associated with waveguide fabrication using femtosecond laser pulses," *Appl. Phys. A: Mater. Sci. Process.*, vol. 76, pp. 367–372, Mar. 2003.

[245] H.-B. Sun, S. Juodkazis, M. Watanabe, S. Matsuo, H. Misawa, and J. Nishii, "Generation and recombination of defects in vitreous silica induced by irradiation with a Near-Infrared femtosecond laser," *J. Phys. Chem. B*, vol. 104, pp. 3450–3455, Apr. 2000.

[246] S. Rajesh and Y. Bellouard, "Towards fast femtosecond laser micromachining of fused silica: The effect of deposited energy," *Opt. Express*, vol. 18, pp. 21490–21497, Sept. 2010.

[247] M. F. Ashby, *Materials Selection in Mechanical Design, 4th ed.* 30 Corporate Drive, Suite 400 Burlington, MA 01803, USA: Butterworth-Heinemann, 2011.

[248] Y. Shi, D. Ma, A. P. Song, B. Wheaton, M. Bauchy, and S. R. Elliott, "Structural evolution of fused silica below the glass-transition temperature revealed by in-situ neutron total scattering," *J. Non-Cryst. Solids*, vol. 528, p. 119760, Jan. 2020.

[249] J. G. Guy Mayer, "Effets des neutrons rapides sur quelques constantes physiques du quartz cristallin et de la silice vitreuse," *J. Phys. Radium*, vol. 18, pp. 109–114, 1957.

[250] P. L. Higby, E. J. Friebele, C. M. Shaw, M. Rajaram, E. K. Graham, D. L. Kinser, and E. G. Wolff, "Radiation effects on the physical properties of Low-Expansion-Coefficient glasses and ceramics," *J. Am. Ceram. Soc.*, vol. 71, pp. 796–802, Sept. 1988.

[251] D. L. Griscom, "A minireview of the natures of Radiation-Induced point defects in pure and doped silica glasses and their Visible/Near-IR absorption bands, with emphasis on Self-Trapped holes and how they can be controlled," *Physics Research International*, vol. 2013, Feb. 2013.

[252] L. Skuja, H. Hosono, and M. Hirano, "Laser-induced color centers in silica," in *Laser-Induced Damage in Optical Materials: 2000*, vol. 4347, pp. 155–168, International Society for Optics and Photonics, Apr. 2001.

[253] A. Zoubir, C. Rivero, R. Grodsky, K. Richardson, M. Couzi, and others, "Laser-induced defects in fused silica by femtosecond IR irradiation," *Phys. Rev. B*, vol. 73, June 2006.

[254] H. Nishikawa, R. Nakamura, Y. Ohki, and Y. Hama, "Correlation of preexisting diamagnetic defect centers with induced paramagnetic defect centers by ultraviolet or vacuum-ultraviolet photons in high-purity silica glasses," *Phys. Rev. B Condens. Matter*, vol. 48, pp. 15584–15594, Dec. 1993.

[255] L. Skuja and B. Güttler, "Detection of interstitial oxygen molecules in SiO_2 glass by a direct photoexcitation of the infrared luminescence of singlet O_2," *Phys. Rev. Lett.*, vol. 77, pp. 2093–2096, Sept. 1996.

[256] H. Hosono, Y. Ikuta, T. Kinoshita, K. Kajihara, and M. Hirano, "Physical disorder and optical properties in the vacuum ultraviolet region of amorphous SiO(2)," *Phys. Rev. Lett.*, vol. 87, p. 175501, Oct. 2001.

[257] S. O. Kucheyev and S. G. Demos, "Optical defects produced in fused silica during laser-induced breakdown," *Appl. Phys. Lett.*, vol. 82, pp. 3230–3232, May 2003.

[258] D. L. Griscom and M. Mizuguchi, "Determination of the visible range optical absorption spectrum of peroxy radicals in gamma-irradiated fused silica," *J. Non-Cryst. Solids*, vol. 239, pp. 66–77, Oct. 1998.

[259] A. H. Edwards and W. B. Fowler, "Theory of the peroxy-radical defect in a-SiO$_2$," *Phys. Rev. B Condens. Matter*, vol. 26, pp. 6649–6660, Dec. 1982.

[260] E. L. Williams, "Diffusion of oxygen in fused silica," *J. Am. Ceram. Soc.*, vol. 48, pp. 190–194, Apr. 1965.

[261] K. Kajihara, T. Miura, H. Kamioka, A. Aiba, M. Uramoto, Y. Morimoto, M. Hirano, L. Skuja, and H. Hosono, "Diffusion and reactions of interstitial oxygen species in amorphous SiO2: A review," *J. Non-Cryst. Solids*, vol. 354, pp. 224–232, Jan. 2008.

[262] R. A. Devine, J. J. Capponi, and J. Arndt, "Oxygen-diffusion kinetics in densified, amorphous SiO$_2$," *Phys. Rev. B Condens. Matter*, vol. 35, pp. 770–773, Jan. 1987.

[263] R. Desmarchelier, B. Poumellec, F. Brisset, S. Mazerat, and M. Lancry, "In the heart of femtosecond laser induced nanogratings: From porous nanoplanes to form birefringence," *WJNSE*, vol. 05, pp. 115–125, Nov. 2015.

[264] Robert D. Fouchaux and R. O. Simmons, "Measurements of thermal expansion and thermal equilibrium defects in silver chloride," *Physical review*, vol. 136, Dec. 1964.

[265] M. G. Pamato, I. G. Wood, D. P. Dobson, S. A. Hunt, and L. Vočadlo, "The thermal expansion of gold: point defect concentrations and pre-melting in a face-centred cubic metal," *J. Appl. Crystallogr.*, vol. 51, pp. 470–480, Apr. 2018.

[266] K. Wang and R. R. Reeber, "The perfect crystal, thermal vacancies and the thermal expansion coefficient of aluminium," *Philos. Mag. A*, vol. 80, pp. 1629–1643, July 2000.

[267] K. Watari, K. Ishizaki, and F. Tsuchiya, "Phonon scattering and thermal conduction mechanisms of sintered aluminium nitride ceramics," *J. Mater. Sci.*, vol. 28, pp. 3709–3714, July 1993.

[268] S. Cao, H. He, and W. Zhu, "Defect induced phonon scattering for tuning the lattice thermal conductivity of SiO2 thin films," *AIP Adv.*, vol. 7, p. 015038, Jan. 2017.

[269] Y. Wang, S. Wei, M. R. Cicconi, Y. Tsuji, M. Shimizu, Y. Shimotsuma, K. Miura, G. Peng, D. R. Neuville, B. Poumellec, and M. Lancry, "Femtosecond laser direct writing in SiO 2 -al 2 O 3 binary glasses and thermal stability of type II permanent modifications," *J. Am. Ceram. Soc.*, vol. 122, p. 66, May 2020.

[270] F. Zhang, Y. Yu, C. Cheng, Y. Dai, H. Zhang, and J. Qiu, "Wavelength response and thermal stability of embedded nanograting structure light attenuator fabricated by direct femtosecond laser writing," *Appl. Phys. B*, vol. 117, pp. 53–58, Oct. 2014.

Bibliography

[271] W. Primak, L. H. Fuchs, and P. Day, "Radiation damage in insulators," *Phys. Rev.*, vol. 92, pp. 1064–1065, Nov. 1953.

[272] M. Grimsditch, "Annealing and relaxation in the high-pressure phase of amorphous SiO2," *Phys. Rev. B Condens. Matter*, vol. 34, pp. 4372–4373, Sept. 1986.

[273] O. Pierard, C. Friebel, and I. Doghri, "Mean-field homogenization of multi-phase thermo-elastic composites: a general framework and its validation," *Compos. Sci. Technol.*, vol. 64, pp. 1587–1603, Aug. 2004.

[274] F. Zhang, A. Cerkauskaite, R. Drevinskas, P. G. Kazansky, and J. Qiu, "Microengineering of optical properties of GeO 2 glass by ultrafast laser nanostructuring," *Advanced Optical Materials*, vol. 5, p. 1700342, Dec. 2017.

Curriculum Vitae

Pieter Vlugter
Born on 1st July 1987
Nationality: Dutch
pieter.vlugter@gmail.com

Education

2016 - 2020	PhD candidate at Galatea Laboratory
	Institute of Microengineering, School of Engineering
	Ecole Polytechnique Fédérale de Lausanne (EPFL), Switzerland
2010 - 2016	Master of Science in Mechanical Engineering
	Department of Mechanical Engineering
	Technische Universiteit Eindhoven (TU/e, Eindhoven University of Technology), the Netherlands
2007 -2010	Bachelor of Applied Science in Mechanical Engineering
	Department of Mechanical Engineering
	University of Applied Sciences Utrecht (HU, Hogeschool Utrecht), the Netherlands

Journal articles

Pieter Vlugter and Yves Bellouard (2020). *Elastic properties of self-organized nanogratings produced by femtosecond laser exposure of fused silica.* Physical Review Materials, 4(2), 023607.

Pieter Vlugter, Erica Block and Yves Bellouard (2019). *Local tuning of fused silica thermal expansion coefficient using femtosecond laser.* Physical Review Materials, 3(5), 053802.

Kana Tomita, Tetsuo Kishi, Tetsuji Yano, Pieter Vlugter and Yves Bellouard. *Monolithic damping of silica cantilever through structural control and material modification by fs laser micromachining.* (Accepted, doi:10.1111/ijag.15857)

Enrico Casamenti, Tao Yang, Pieter Vlugter and Yves Bellouard. *Optomechanical coupling of a double-clamped micro-beam nonlinearity for remote vibrations monitoring.* (Under review)

Conferences

Pieter Vlugter and Yves Bellouard. *Towards the Microfabrication of Thermally Compensated Monolithically Integrated Devices Using Ultrafast Lasers.* ASPE 34th meeting, Pittsburgh (PA), United States, October 28 - November 1 2019. (oral presentation)

Pieter Vlugter and Yves Bellouard. *Understanding Nanogratings Elastic Anisotropy: A Step Towards Femtosecond Laser-Written Elastic Meta-Crystal.* CLEO, Munich, Germany, 23-27 June 2019. (oral presentation)

Pieter Vlugter and Yves Bellouard. *Tuning of the thermal expansion coefficient of fused silica by femtosecond laser.* SPIE LASE, San Francisco (CA), United States, 27 January - 1 February 2018. (oral presentation)